

UC San Diego

UC San Diego Electronic Theses and Dissertations

Title

Development of Catalytic Metal-Organic Frameworks

Permalink

<https://escholarship.org/uc/item/9ht6k022>

Author

Yu, Xiao

Publication Date

2018

Peer reviewed|Thesis/dissertation

UNIVERSITY OF CALIFORNIA SAN DIEGO

Development of Catalytic Metal-Organic Frameworks

A dissertation submitted in partial satisfaction of the requirements
for the degree Doctor of Philosophy

in

Nanoengineering

by

Xiao Yu

Committee in charge:

Professor Seth M. Cohen, Chair
Professor Eric Fullerton
Professor Darren Lipomi
Professor Joseph O'Connor
Professor Joseph Wang

2018

Copyright

Xiao Yu, 2018

All rights reserved.

The Dissertation of Xiao Yu is approved, and it is acceptable in quality and form for publication on microfilm and electronically:

Chair

University of California San Diego

2018

DEDICATION

To my family and my loved ones.

TABLE OF CONTENTS

Signature Page	iii
Dedication.....	iv
Table of Contents	v
List of Abbreviations and Symbols	viii
List of Figures.....	xi
List of Tables	xv
Acknowledgements	xvi
Vita	xix
Abstract of the Dissertation	xx
Chapter 1 : Introduction to Metal-Organic Frameworks	1
1.1 Metal-Organic Frameworks	2
1.2 MOFs as Heterogeneous Catalysts.....	10
1.2.1 SBUs as Catalytic Centers.....	12
1.2.2 Functionalized Linkers as Catalytic Sites.....	12
1.3 Acknowledgments	15
1.4 References	15
Chapter 2 : Photocatalytic Metal-Organic Frameworks for Aerobic Oxidation of Arylboronic Acids.....	21
2.1 Introduction	22
2.2 Synthesis and Characterization of MOFs Incorporated with Polypyridyl Ruthenium Photocatalyst	23
2.3 MOF Catalysis for Aerobic Oxidation of Arylboronic Acids.....	27

2.4 Conclusion.....	31
2.5 Experimental	31
2.6 Appendix	34
2.7 Acknowledgments	46
2.8 References	46
Chapter 3 : Photocatalytic Metal-organic Frameworks for Selective 2,2,2-Trifluoroethylation	
of Styrenes	50
3.1 Introduction	51
3.2 MOF Synthesis and Characterization.....	53
3.3 Catalytic Reactions.....	56
3.4 Conclusion.....	60
3.5 Experimental	61
3.6 Appendix	64
3.7 Acknowledgements	79
3.8 References	79
Chapter 4 : A Metal-Organic Framework with Exceptional Activity for C–H Bond Amination	
.....	83
4.1 Introduction	84
4.2 CPF-5 as Catalyst for Intermolecular C-H Amination.....	85
4.3 Mechanism Study	94
4.4 PSE of CPF-5	96
4.5 Conclusion.....	99
4.6 Appendix	115

4.7 Acknowledgements	126
4.8 References	126
Chapter 5 : Metal-Organic Frameworks as Micromotors with Tunable Engines and Brakes	130
5.1 Introduction	131
5.2 MOF-MNMs Synthesis and Characterization.....	132
5.3 Motion Test	134
5.4 Conclusion.....	139
5.5 Experimental	140
5.6 Appendix	142
5.7 Acknowledgements	144
5.8 References	144

LIST OF ABBREVIATIONS AND SYMBOLS

BET	Brunauer-Emmett-Teller
bpy	Bipyridine
BzTHF	2,3-dihydrobenzofuran
°C	Degrees Celsius
CAT	2,3-dihydroxyterephthalic acid
CDC	Deuterated Chloroform
CHCl ₃	Chloroform
CH ₂ Cl ₂ or DCM	Methylene Chloride
CH ₃ CN	Acetonitrile
d ₆ -DMSO	Deuterated DMSO
DHP	3,4-Dihydro-2H-pyran
DMF	<i>N,N'</i> -dimethylformamide
DMOF	D = 1,4-diazabicyclo[2.2.2]octane (dabco)
DMSO	Dimethylsulfoxide
EtOAc	Ethyl Acetate
h	Hour
H ₂ bdc	Terephthalic Acid
H ₂ bpdc	4,4'-biphenyldicarboxylate Acid
H ₂ bpdc	2,2'-bipyridine-5,5'-dicarboxylic Acid
H ₂ btc	Benzene-1,3,5-tricarboxylic acid
H ₂ O	Water, hydrate

H ₂ tcpp	4-tetracarboxyphenyl porphyrin
HKUST	Hong Kong University of Science and Technology
ICP-MS	Inductively-Coupled Plasma Mass Spectrometry
KIE	Kinetic Isotope Effect
MeOH	Methanol
MIL	Material Institut Lavoisier
MNMs	Micro- and Nanomotors
MOF	Metal-Organic Framework
MS	Mass spectrometry
MgSO ₄	Magnesium Sulfate
N ₂	Dinitrogen
NMR	Nuclear Magnetic Resonance spectroscopy
PCN	Porous Coordination Network
PSE	Postsynthetic Exchange
PSM	Postsynthetic Modification
PXRD	Powder X-ray Diffraction
RT	Room Temperature
SBU	Secondary Building Unit
SEM	Scanning Electron Microscopy
TCAT	2,3-dimercaptoterephthalic acid
TGA	Thermal Gravimetric Analysis
THF	Tetrahydrofuran

THP	Tetrahydropyran
UiO	University of Oslo
UMCM	University of Michigan Crystalline Material
XRD	X-ray diffraction
ZIF	Zeolite Imidazolate Framework

LIST OF FIGURES

Figure 1-1 MOF diversity resulting from various combinations of SBUs and ligands.....	3
Figure 1-2 Schematic depiction of presynthetic method, postsynthetic modification (PSM) and postsynthetic exchange (PSE) of MOFs.....	5
Figure 1-3 PSM on three amine-tagged MOFs. IRMOF-1-NH ₂ , DMOF-1-NH ₂ and UCMCM-1-NH ₂ were transformed to IRMOF-1-AM _n , DMOF-1-AM _n and UCMCM-1-AM _n by reactions between amine groups (blue) and alkyl anhydrides (the length of alkyl chain is denoted by n). The obtained MOFs contained amide bonds (red).	7
Figure 1-4 Schemes of PSE on UiO-66.....	10
Figure 1-5 Schematic depiction of three approaches to design MOF catalyst.	11
Figure 2-1 Synthesis of UiO-67-Ru(bpy) ₃ using three different synthetic strategies.....	24
Figure 2-2 ¹ H NMR (D ₃ PO ₄ /d ⁶ -DMSO digested) of UiO-67-Ru(bpy) ₃ containing different amount of Ru complex	26
Figure 2-3 PXRD of UiO-67-Ru(bpy) ₃ containing different amount of Ru complex.....	27
Figure 2-4 PXRD of UiO-67-bpy _{0.5} , UiO-67-bpy _{1.0} , and their metalated derivatives (PSM for 1 h).....	35
Figure 2-5 TGA of UiO-67-bpy _{0.25} (blue) and UiO-bpy-[Ru(bpy) ₃] _{0.1} (red).	35
Figure 2-6 N ₂ isotherms of UiO-67-bpy _{0.25} and UiO-67-[Ru(bpy) ₃].	36
Figure 2-7 ¹ HNMR of oxidation of phenylboronic acid.....	37
Figure 2-8 ¹ HNMR of 4-methoxyphenylboronic acid (black), 4-methoxyphenol (brown), aerobic oxidation of 4-methoxyphenylboronic acid using UiO-67-[Ru(bpy) ₃] _{0.1} as catalyst under visible-light irradiation	38
Figure 2-9 PXRD of 5 cycles of UiO-67-[Ru(bpy) ₃] _{0.1} catalyst.....	39
Figure 2-10 ¹ HNMR of digested UiO-67-[Ru(bpy) ₃] _{0.1} before (red) and after (blue) catalysis showing minimal or no loss in Ru(bpy) ₃ from the MOF.....	39
Figure 2-11 ¹ H NMR of oxidation of phenylboronic acid using UiO-67-[Ru(bpy) ₃] _{0.1} as catalyst (before reaction, magenta; after reaction, dark red) and UiO-67-bpy _{0.25} as catalyst (after reaction, dark blue).....	40
Figure 2-12 ¹ HNMR of 3-methoxyphenylboronic acid (dark red), 3-methoxyphenol (brown), reaction mixture after photocatalysis under visible-light irradiation (dark green, Yield ~72%) and near UV light irradiation (dark blue, Yield ~79%).....	41

Figure 2-13 ¹ HNMR of 4-(methoxycarbonyl)phenylboronic acid (dark red), methyl 4-hydroxybenzoate (brown) and reaction mixture after photocatalysis under both visible light (dark green, Yield > 95%) and near-UV irradiation (dark blue, Yield > 95%).....	42
Figure 2-14 ¹ HNMR of 4-fluorophenylboronic acid (dark red), 4-fluorophenol (brown), reaction mixture after photocatalysis under both visible-light irradiation (dark green, Yield ~50%) and near-UV irradiation (dark blue, Yield ~55%).....	43
Figure 2-15 ¹ HNMR of 1,4-phenylenediboronic acid (dark red), hydroquinone (brown), mixture after reaction under visible-light irradiation (dark green, Yield 15%) and near-UV irradiation (dark blue, Yield 23%).....	44
Figure 2-16 ¹ HNMR of phenylboronic acid pinacol ester (dark red), phenol (brown) and reaction mixture after photocatalysis under both visible-light (dark green, Yield 91%) and near-UV irradiation (dark blue, Yield > 95%).....	45
Figure 3-1 Synthesis of UiO-67-Ir via PSM and homogeneous Ir catalysts.	55
Figure 3-2 PXRD of UiO-67-bpy _{0.25} (black), UiO-67-Ir(ppy) ₂ (red) and UiO-67-Ir(ppy ^{F'}) ₂ (blue).....	56
Figure 3-3 Proposed mechanism of UiO-67-Ir catalyzed trifluoroethylation reaction.	66
Figure 3-4 ¹ H NMR (D ₃ PO ₄ /d ⁶ -DMSO) of digested UiO-67-bpy _{0.25} (black), UiO-67-Ir(ppy) ₂ (red, with [Ir(ppy) ₂ (dcbpy)] ⁺ denoted by “o”) and UiO-67-Ir(ppy ^{F'}) ₂ (blue, with [Ir(ppy ^{F'}) ₂ (dcbpy)] ⁺ denoted by “*”)......	67
Figure 3-5 Models of UiO-67-Ir MOFs. (a),(b) UiO-67-Ir(ppy) ₂ ; (c),(d) UiO-67-Ir(ppy ^{F'}) ₂ ..	68
Figure 3-6 N ₂ adsorption at 77K for UiO-67-Ir MOFs.	69
Figure 3-7 Time-dependent catalysis by UiO-67-Ir(ppy ^{F'}) ₂ and Ir(ppy) ₃	69
Figure 3-8 Effect of water content on hydroxytrifluoroethylation catalyzed by UiO-67-Ir(ppy ^{F'}) ₂	70
Figure 3-9 ¹ H NMR of digested UiO-67-Ir(ppy ^{F'}) ₂ before (orange) and after (pink) catalytic reaction (with [Ir(ppy ^{F'}) ₂ (dcbpy)] ⁺ denoted by “*”)......	70
Figure 3-10 Photoluminescent spectra (excitation λ = 261 nm) of (1). Ir(ppy ^{F'}) ₂ (Et ₂ dcbpy)Cl; (2). digested As-synthesized UiO-67-Ir(ppy ^{F'}) ₂ ; (3). digested UiO-67-Ir(ppy ^{F'}) ₂ after catalytic reaction; (4). digested UiO-67-bpy _{0.25}	71
Figure 3-11 PXRD of UiO-67-Ir(ppy ^{F'}) ₂ after cycle 1 (black), cycle 2 (blue) and cycle 3 (red).	71
Figure 3-12 GC-MS of 4-methoxystyrene trifluoroethylation reaction catalyzed by UiO-67-Ir(ppy ^{F'}) ₂ for 3 cycles. First two small peaks are solvent and N, N- Diisopropylethylamine (RT < 4 mins).....	72
Figure 3-13 GC-MS of styrene trifluoroethylation reaction catalyzed by UiO-67-Ir(ppy ^{F'}) ₂ . 73	73

Figure 3-14 GC-MS of 4-methylstyrene trifluoroethylation reaction catalyzed by UiO-67-Ir(ppy ^F) ₂ . No dimerization product was found in the reaction mixture.	73
Figure 3-15 GC-MS of 4-bromostyrene trifluoroethylation reaction catalyzed by UiO-67-Ir(ppy ^F) ₂ . No dimerization product was found in the reaction mixture.	74
Figure 3-16 GC-MS of 4-vinylbiphenyl trifluoroethylation reaction catalyzed by UiO-67-Ir(ppy ^F) ₂ . No dimerization product was found in the reaction mixture. Isolated yields were used for this substrate because of high boiling point of the products.	75
Figure 3-17 GC-MS calibration curves of styrenes.	76
Figure 3-18 GC-MS calibration curves of product A (hydroxyethylation products) of different substrates.	77
Figure 3-19 GC-MS calibration curves for product B (ketones) of different substrates.	78
Figure 3-20 GC-MS calibration curves for product C (dimerization products) for two substrates. Other substrates did not show any dimerization product.	78
Figure 4-1 The structures of CPF-5 and composition of its SBUs.	86
Figure 4-2 Reaction scheme and substrate scope for C–H amination by CPF-5. Yield for 3-MeTHF is the combined yield of two isomers. Isolated yields are shown under each amination product with the solvent system indicated.	90
Figure 4-3 Evidence for CPF-5 as an immortal C–H amination catalyst.	93
Figure 4-4 Schematic illustration of C-H amination mechanism.	95
Figure 4-5 Metal exchanged in and out CPF-5 with Co and Fe.	99
Figure 4-6 PXRD of CPF-5 before (red) and after (blue) catalysis.	115
Figure 4-7 N ₂ adsorption at 77 K of CPF-5 before (red) and after (blue) catalysis.	116
Figure 4-8 ¹ H (<i>top</i>) and ¹³ C (<i>bottom</i>) NMR for amination product of THF.	117
Figure 4-9 ¹ H (<i>top</i>) and ¹³ C (<i>bottom</i>) NMR for amination product of BzTHF.	118
Figure 4-10 ¹ H NMR for amination product isomers of 3-Me-THF.	119
Figure 4-11 ¹ H NMR for amination product of DHP.	119
Figure 4-12 ¹ H NMR for amination product of cyclohexene.	120
Figure 4-13 ¹ H NMR for amination product of TBE.	120
Figure 4-14 Conversion of cyclohexene (0.67 mmol) using 1.5 mol% CPF-5 in 5.0 mL of CHCl ₃ , with repeated additions of 50 mg (0.13 mmol) of PhI=NTS.	121
Figure 4-15 Conversion of BzTHF (red) and BzTHP (blue) in the presence of 1.5 mol% CPF-5 and PhI=NTs (1.0 equiv) in dry acetonitrile.	121

Figure 4-16 Kinetic traces for the amination of THF (<i>top</i>) and THF- <i>d</i> ₈ (<i>bottom</i>) by CPF-5 at 30 °C. The Kinetic Isotope Effect (KIE) for the reaction was determined using the average of three runs for each substrate.	122
Figure 4-17 Optimized structures of [Zn(OH ₂) ₃ (MeTet)Mn(NTs)] ⁺ (i1), [Zn(OH ₂) ₃ (MeTet)Mn(NTs)(THF)] ⁺ (m1), [Zn(OH ₂) ₃ (MeTet)Mn(NTs)(THF·)] ⁺ (m2), [Zn(OH ₂) ₃ (MeTet)Mn(κ ² - <i>N,O</i> -N(H)Ts(OC ₄ H ₇))] ⁺ (p).	123
Figure 4-18 Comparative energies along the reaction coordinate for the amination of THF via a proposed hydrogen-atom abstraction/radical recombination pathway.	124
Figure 5-1 Zr-based MOF micromotors.	133
Figure 5-2 SEM and EDX characterization of UiO-67-bpy _{0.25} metalated with different transition metal salts	134
Figure 5-3 Tuning the speed of micromotor engines with different metals.	136
Figure 5-4 Chelators act as molecular brakes for MOF micromotors.	138
Figure 5-5 PXRD of MOF micromotors after treatment with braking chelators for 1 h	143
Figure 5-6 SEM of MOF micromotors after treatment with braking chelators for 1 h	143
Figure 5-7 Mechanism of catalytic decomposition of hydrogen peroxide by Co(II) or Mn(II).	144

LIST OF TABLES

Table 2-1 Summary of results for the aerobic oxidative hydroxylation of arylboronic acids using UiO-67-[Ru(bpy) ₃] _{0.1} as catalyst.....	29
Table 2-2 Scope of substrate conversion using UiO-67-[Ru(bpy) ₃] _{0.1} as catalyst.....	30
Table 3-1 Conversions and yields of photocatalytic trifluoroethylation of styrene.	59
Table 3-2 Substrate scope using UiO-67-Ir(ppy ^{F'}) ₂ as photocatalyst.	60
Table 3-3 BET surface areas of UiO MOFs.	65
Table 3-4 Recyclability test of UiO-67-Ir(ppy ^{F'}) ₂ for trifluoroethylation of 4-methoxystyrene.	65
Table 4-1 Amination of tetrahydrofuran (THF) or 2,3-dihydrobenzofuran (BzTHF) with different catalysts.....	88
Table 4-2 PSE of CPF-5 with Co and Fe under different reaction conditions.	98
Table 4-3 Crystal data and structure refinement for CPF-5 after use in 20 catalytic cycles with BzTHF.	125
Table 5-1 Metal ratio before and after treatment with chemical brakes (IDA or EDTA), as measured by SEM-EDX.	142

ACKNOWLEDGEMENTS

I would like to thank and acknowledge my committee for their support throughout my time at UCSD. Particularly, I would like to thank Professor Seth Cohen for his support as committee chair, my mentor and advisor, and as my friend. Seth has been supportive and encouraging from my first monthly meeting to my last draft throughout these years, and I am not sure if I can achieve many accomplishments without his support and guidance. I learned a lot from him in both research and life.

I would like to thank the past Cohen Lab members, Dr. Honghan Fei, Dr. Zhengjie Zhang, Dr. Le Wang, Dr. Yuyong Ma, Dr. Yao Chen, Dr. TengHao Chen, Dr. Phuong Dau, Dr. Michael Denny, Dr. Cy Credille for helping me to survive grad school and being supportive colleagues. They taught me a lot on both research and life when I first joined the lab. I also thank the present Cohen Lab members for being my friends through my PhD. We spent a lot of time helping each other on experiments and also celebrating every holiday and big dates during our PhD. You guys make me feel at home in the lab. I really appreciate your support.

I would like to acknowledge and thank Dr. Yongxuan Su for helping to teach me the art of mass spectrometry and analytical chemistry, I would also like to thank the rest of the facilities and personnel that work behind the scenes to make the department run every single day.

Lastly, I would like to acknowledge my family and my boyfriend Zhi Deng. Your loving support has made it possible for me to overcome challenges from failed experiments, anxiety and depression. You have kept me sane, you have never lost faith in me, and you have always made sure that I know that I am loved. I would like to thank my roommate Yuan Pu for being my considerate friend especially during my last year. Thank you all.

Chapter 1 is, in part, a reprint of materials published in *CrystEngComm*: Xiao Yu, Le Wang and Seth M. Cohen*, “Photocatalytic Metal-Organic Frameworks for Organic Transformations”. *CrystEngComm*. **2017**, *19*, 4126-4136. The dissertation author was the primary researcher and writer for the paper. The permission to reproduce the paper was granted by the Royal Society of Chemistry, copyright 2017.

Chapter 2 is, in large part, a reprint of paper published in *Chemical Communication*: Xiao Yu and Seth M. Cohen*, “Photocatalytic Metal-organic Frameworks for the Aerobic Oxidation of Arylboronic Acids” *Chem. Commun.* **2015**, *51*, 9880-9883. The dissertation author was the primary researcher for the data presented. The permission to reproduce the paper was granted by the Royal Society of Chemistry, copyright 2015.

Chapter 3 is, in large part, a reprint of paper published in *Journal of the American Chemistry Society*: Xiao Yu and Seth M. Cohen*, “Photocatalytic Metal–Organic Frameworks for Selective 2,2,2-Trifluoroethylation of Styrenes” *J. Am. Chem. Soc.* **2016**, *138*, 12320-12323. The dissertation author was the primary researcher and the primary writer for the reprinted data presented herein, The permission to reproduce the paper was granted by the American Chemical Society, copyright 2016.

Chapter 4 is, in part, a reprint of material published in *Angewandte Chemie International Edition*: Le Wang, Douglas W. Agnew, Xiao Yu, Josh S. Figueroa*, and Seth M. Cohen*, “A Metal-Organic Framework with Exceptional Activity for C–H Bond Amination” *Angew. Chem. Int. Ed.* **2018**, *57*, 511-515. The dissertation author was the primary researcher for the reprinted data presented, and was a co-author on the aforementioned publication. The permission to reproduce this material was granted by the John Wiley and Sons, copyright 2018.

Chapter 5 is, in large part, a reprint of material published in *Journal of the American Chemistry Society*: Jinxing Li, Xiao Yu, Mingli Xu, Wenjuan Liu, Elodie Sandraz, Hsin Lan, Joseph Wang*, and Seth M. Cohen*, “Metal–Organic Frameworks as Micromotors with Tunable Engines” *J. Am. Chem. Soc.* **2017**, *139*, 611-614. The dissertation author was the primary researcher for the data presented and was the primary author of this publication. The permission to reproduce this material was granted by the American Chemical Society, copyright 2017.

VITA

Education

- 2018 Doctor of Philosophy, Nanoengineering, University of California San Diego, La Jolla, California
- 2014 Master of Science, Nanoengineering, University of California San Diego, La Jolla, California
- 2013 Bachelor of Science, Materials Chemistry, Harbin Institute of Technology, China

Publications

1. "Photocatalytic Metal-organic Frameworks for the Aerobic Oxidation of Arylboronic Acids". **Xiao Yu** and Seth M. Cohen*, *Chem. Commun.* **2015**, *51*, 9880-9883.
2. "Photocatalytic Metal–Organic Frameworks for Selective 2,2,2-Trifluoroethylation of Styrenes". **Xiao Yu** and Seth M. Cohen*, *J. Am. Chem. Soc.* **2016**, *138*, 12320-12323.
3. "Metal–Organic Frameworks as Micromotors with Tunable Engines and Brakes". Jinxing Li, **Xiao Yu**, Mingli Xu, Wenjuan Liu, Elodie Sandraz, Hsin Lan, Joseph Wang*, and Seth M. Cohen*, *J. Am. Chem. Soc.* **2017**, *139*, 611-614 (JL and XY contributed equally)
4. "Photocatalytic Metal-Organic Frameworks for Organic Transformations". **Xiao Yu**, Le Wang and Seth M. Cohen*, *CrystEngComm.* **2017**, *19*, 4126-4136 (invited review).
5. "A Metal-Organic Framework with Exceptional Activity for C-H Bond Amination". Le Wang, Douglas W. Agnew. **Xiao Yu**. Joshua S. Figueroa*, and Seth M. Cohen*. *Angew. Chem. Int. Ed.* **2018**, *57*, 511-515.
6. "Flux Melting of Metal-Organic Frameworks". Louis Longley, Sean M. Collins, Shichun Li, Glen J. Smales, Ilknur Eruçar, Ang Qiao, Jingwei Hou, Cara M. Doherty, Aaron W. Thornton, Anita J. Hill, **Xiao Yu**, Nicholas J. Terrill, Andrew J. Smith, Seth M. Cohen, Paul A. Midgley, David A. Keen, Shane G. Telfer and Thomas D. Bennett*. *in submission*.
7. "Pressure Promoted Low-Temperature Melting of Metal-Organic Frameworks". Remo N. Widmer, Giulio Lampronti, Simone Anzellini, Romain Gaillac, Stefan Farsang, Chao Zhou, Ana M. Belenguer, Craig Wilson, Hannah Palmer, Annette K. Kleppe, Michael T. Wharmby, **Xiao Yu**, Seth M. Cohen, Shane G. Telfer, Simon A. T. Redfern, Francois-Xavier Coudert, Simon G. MacLeod and Thomas D. Bennett*. *in submission*.

ABSTRACT OF THE DISSERTATION

Development of Catalytic Metal-Organic Frameworks

by

Xiao Yu

Doctor of Philosophy in Nanoengineering

University of California San Diego, 2018

Professor Seth M. Cohen, Chair

MOFs have become a very active area of inorganic materials research. The high surface areas of MOFs have prompted numerous studies for their use in different applications, including catalysis. MOFs have the potential to display significant advantages as catalysts over conventional heterogeneous catalysts. Features including high surface areas, large pore/cavity sizes, and the ability to modify design molecular-style catalysts within MOFs make these materials uniquely suited to achieve enzyme-like performance. The use of both pre- and post-synthetic methods to modify MOFs adds to the unique tunability of these materials.

This dissertation will discuss the catalytic applications of MOFs for organic transformations and as nanomotors. A series of catalytic MOFs were synthesized via different

methods including prefunctionalization, postsynthetic modification, and postsynthetic exchange. In the first two parts, different photocatalytic polypyridyl complexes have been successfully incorporated into MOF ligands to produce stable and reusable heterogenous catalysts. Organic reactions, including aerobic oxidations of arylboronic acids, and trifluoroethylation of styrenes are described in Chapters 2 and 3, respectively. In Chapter 4, a MOF with catalytic SBUs is investigated for its use in C-H amination chemistry, displaying exceptional activity under mild conditions. Lastly, in Chapter 5, in a relatively new area for catalytic MOFs, MOF micro- and nanomotors, will be described.

Chapter 1 : Introduction to Metal-Organic Frameworks

1.1 Metal-Organic Frameworks

Metal-organic frameworks are a class of porous crystalline materials constructed from metal ions or clusters and organic linkers. The metal ions or clusters are often referred to as secondary building units (SBUs). Metal-containing SBUs vary in nuclearity and geometry depending on the types of metal ions and coordination environments (Figure 1-1 *top*). The SBUs are connected by the organic bridging ligands to form the MOF structure via coordination bonds. Many MOFs possess large pores and display high surface areas, in excess of 2000 m²/g. The versatile coordination chemistry, as well as the variety of metal ions, polytopic linkers and terminating ligands, affords an essentially infinite number of MOF structures (Figure 1-1).¹ Particularly, merging different SBUs with the same organic ligand can afford multiple types of MOFs by changing synthesis conditions. For example, merging terephthalic acid (H₂bdc, deprotonated as bdc²⁻ to bind metal ions) with Zn²⁺ SBUs results in the formation of MOF-5 (a related series of materials described by Yaghi and co-workers can be prepared from other dicarboxylates).² Combining bdc²⁻ with Fe/Cr/Al SBUs under different solvothermal conditions produces MIL-53 and MIL-101 (MIL = Material Institut Lavoisier).³ Use of the same bdc²⁻ ligand can also produce UiO-66 (UiO = UiO = University of Oslo) with Zr⁴⁺ or Hf⁴⁺ SBUs.⁴ Mixing different organic ligands (bdc²⁻, btc²⁻, MIm⁻) with a common metal ion (e.g., Zn²⁺) leads to diverse MOFs (MOF-5, HKUST-1, and ZIF-8, respectively; HKUST = Hong Kong University of Science and Technology, ZIF = zeolite imidazolate framework).⁵⁻⁶ The unparalleled tunability of MOF structures, as well as their diverse physical and chemical properties, has led to proposed uses in a wide applications in gas storage/separation,⁷⁻⁸ chemical sensing,⁹ drug delivery,¹⁰⁻¹¹ and catalysis.¹²⁻¹³

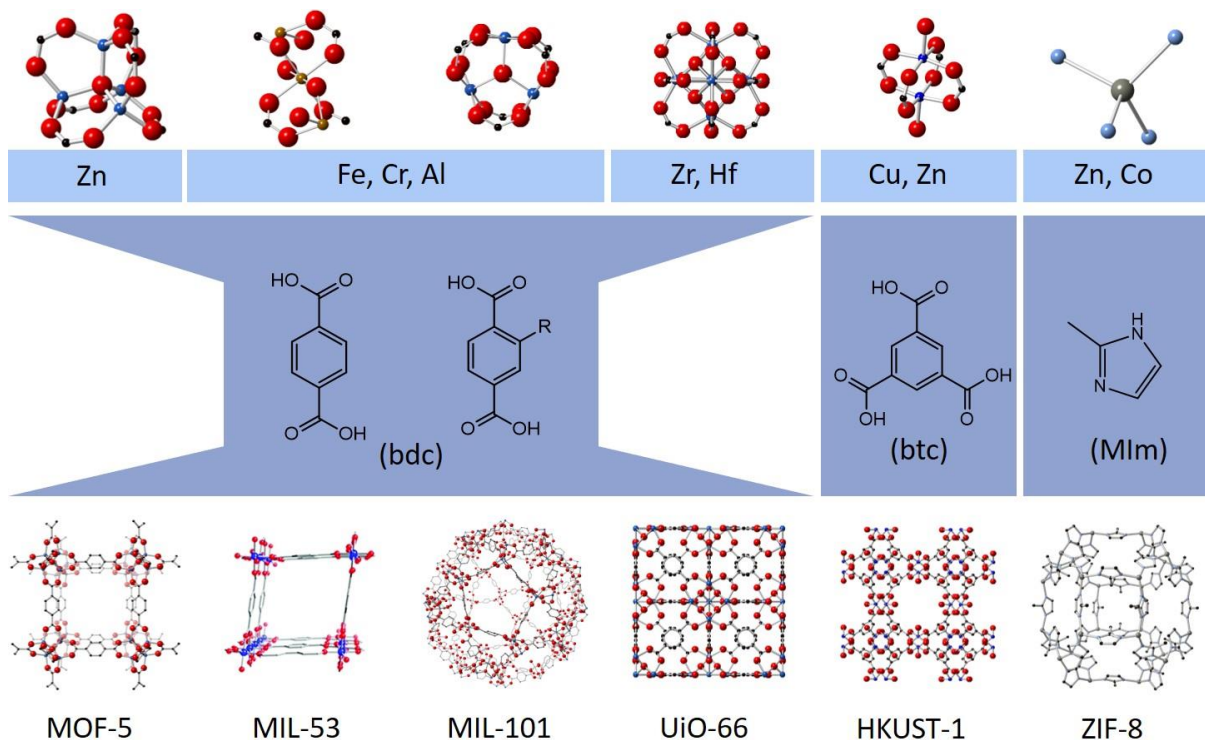


Figure 1-1 MOF diversity resulting from various combinations of SBUs and ligands. *Top:* From left to right, they are examples of 4-Zn tetrahedral cluster, 3-M (M = Fe/ Cr/Al) cluster, 6-M (M = Zr/Hf) octahedral cluster, dinuclear Cu/Zn paddle-wheel cluster and simple one-metal (Zn/Co) cluster. *Middle:* Examples of commonly-used ligands have been listed including terephthalic acid (H₂bdc) and its derivatives, benzene-1,3,5-tricarboxylic acid (H₂btc) and 2-methyl-1H-imidazole (HMIIm). *Bottom:* Combination of various SBUs and ligands leads to almost infinite types of MOFs.

The development of MOF applications relies on the development of MOF synthetic methods to introduce various functionalities. MOFs are conventionally synthesized under solvothermal conditions. Depending on the order of MOF assembly and functionalization, these synthetic methods are further categorized as presynthetic and postsynthetic methods. During last two decades, both presynthetic and postsynthetic methods have been widely employed in MOF preparation and functionalization (Figure 1-2).¹⁴⁻¹⁵

MOFs can be prefunctionalized where a functional organic ligand is directly combined with metal ions under solvothermal conditions. In 2010, Yaghi and coworkers reported the successful synthesis of multivariate MOFs (MTV-MOFs), which is a class of MOFs containing a variety of functionalized ligands within the structure.¹⁶ In their study, they incorporated eight distinctive functionalities: $-\text{NH}_2$, $-\text{NO}_2$, $-\text{Br}$, $-\text{Cl}_2$, $-(\text{CH}_3)_2$, $-(\text{OC}_3\text{H}_5)_2$, $-\text{C}_4\text{H}_4$, and $-(\text{OC}_7\text{H}_7)_2$ on H_2bdc ligands into a singular crystalline network using a facile, one-pot method. The different ligands in the MTV-MOF are randomly distributed throughout the ordered framework. This remarkable example demonstrates the possibility to incorporate a wide variety of different linkers in a single MOF structure via presynthetic methods. However, the requirement of the same geometry and connectivity for these linkers (i.e., isorecticular synthesis) limits the variety of functionality that can be incorporated into MOFs. Recently, the Zhou group incorporated two kinds of ligands with different symmetry and connectivity into a MOF. They employed presynthetic method to synthesize a UiO-66 based mixed-linker MOF, where a H_2bdc ligand and tetratopic 4-tetracarboxyphenyl porphyrin (H_4tcpp) ligands were integrated into the ultra-stable UiO-66 backbone.¹⁷ In addition to mixed-linker MOFs, presynthetic methods can also be utilized to prepare mixed-metal MOFs. In 2014, Yaghi and coworkers reported the one-pot synthesis of mixed-metal MOF-74 containing 10 different divalent metals.¹⁸ Other prefunctionalization strategies have also been employed to produce mixed-metal MOFs.¹⁹⁻²⁰

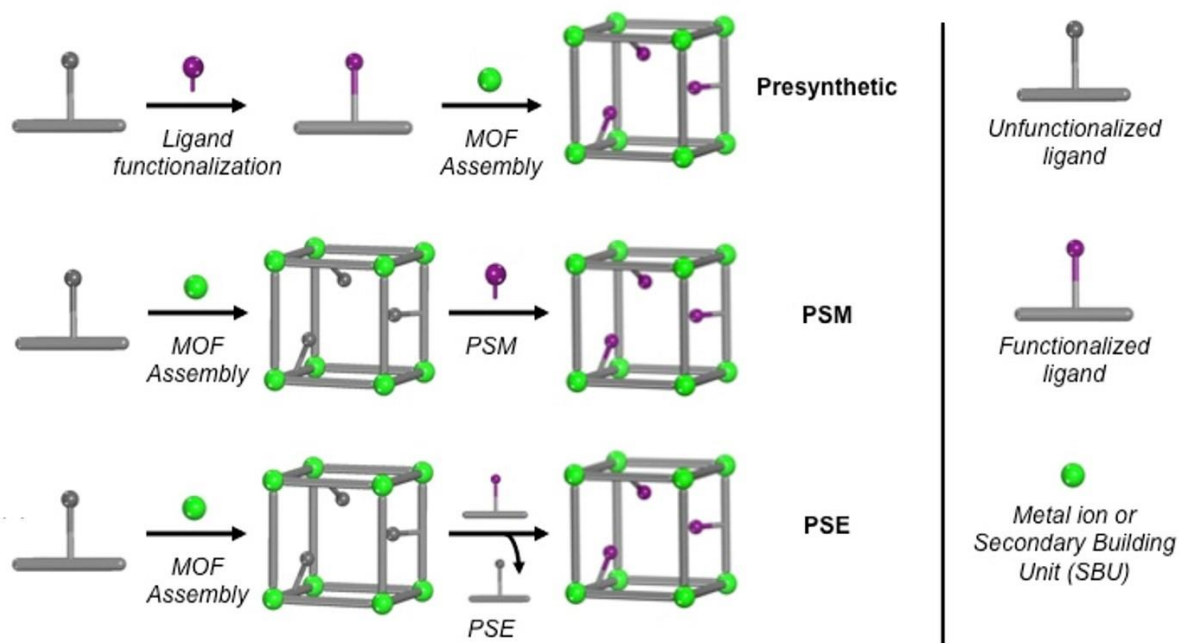


Figure 1-2 Schematic depiction of presynthetic method, postsynthetic modification (PSM) and postsynthetic exchange (PSE) of MOFs. *Top:* Using presynthetic methods, a functionalized ligand (gray bar with magenta ball) can be incorporated into a MOF (metals represented by green spheres). *Middle:* In PSM, the intact MOF lattice can be modified with chemical reagents, to give a functionalized material that remains crystalline and porous. *Bottom:* In PSE, the original MOF ligand can be replaced by a functionalized ligand after MOF assembly, without any loss of crystallinity and porosity.

Although presynthetic methods have been widely used in MOF synthesis, there are many cases that the desired MOFs cannot be easily obtained using these methods. Presynthetic methods have been largely limited to cases where the functional groups are not thermally stable under MOF synthesis conditions. In addition, functional ligands containing strong chelating groups cannot be easily incorporated into MOFs via presynthetic methods, because the chelators will coordinate to metal ions in the SBUs and thus interfere with MOF growth. For mixed-metal MOFs, presynthetic approaches, by directly mixing different metal ions without careful modifications to the solvothermal conditions, often result in either mixed phases or amorphous materials (e.g., metal oxides), rather than a single MOF phase containing a mixture

of metal ions in the SBU.²⁰⁻²² Successful examples of mixed-component MOFs synthesized through presynthetic methods all require precisely controlled solvothermal conditions. However, uncovering these conditions is often a very time-consuming and nontrivial endeavor. From these perspectives, postsynthetic methods provide more opportunities to introduce target functionalities into MOF structures.

“Postsynthetic” refers to the fact that chemical reactions are conducted after the MOF has already formed.²³ Postsynthetic methods for MOF synthesis include, but are not limited to, postsynthetic modification (PSM) and postsynthetic exchange (PSE).²⁴⁻²⁵ PSM most often describes the tailoring of ligand struts after MOF assembly. PSM has become a commonplace tool for the synthesis and derivatization of MOFs. Since 2007, Cohen and co-workers have conducted systematic investigations on PSM of MOFs.²⁶ They investigated the generality of covalent-PSM methods in three different MOFs containing bdc^{2-} ligands as building blocks: IRMOF (MOF-5), UCMC (UMCM = University of Michigan Crystalline Material), and DMOF (D = 1,4-diazabicyclo[2.2.2]octane (dabco)). “Amine tags” were introduced into these MOFs by replacing H_2bdc with $\text{H}_2\text{bdc-NH}_2$ ligands during MOF synthesis (Figure 1-3). The obtained IRMOF-1- NH_2 , UCMC-1- NH_2 and DMOF-1- NH_2 can readily undergo PSM with reagents such as alkyl anhydrides to form the corresponding amide-bearing materials.²⁷⁻²⁸ Due to the variety of bdc -containing MOFs, incorporation of bdc-NH_2 into these MOFs can easily afford numerous amine-tagged MOFs. The obtained MOFs with amine tags readily react with reagents like carboxylic acids, anhydrides and aldehydes to introduce more functionalities that cannot be achieved via conventional MOF synthesis.²⁵ A more recent example of PSM on amine-tagged MOFs was reported by Toste and Yaghi,²⁹ where the authors constructed small peptides on the organic struts of MTV-IRMOF-74-III via seven sequential PSM reactions,

without losing MOF porosity or crystallinity. Taking the advantage of various organic reactions, PSM on MOFs is not limited to amine-tagged MOFs.³⁰ Many reports have also described the use of functional tags like aldehydes, alkynes, azides, thioethers, and aryl halides.³¹⁻³³ For example, the Zhou group reported PSM on highly stable Zr-MOF series: PCN-58 and PCN-59 (PCN = Porous Coordination Network).³⁴ The azide group on PCN-58 and PCN-59 was able to undergo a click reaction with alkynes to postsynthetically form triazole groups.

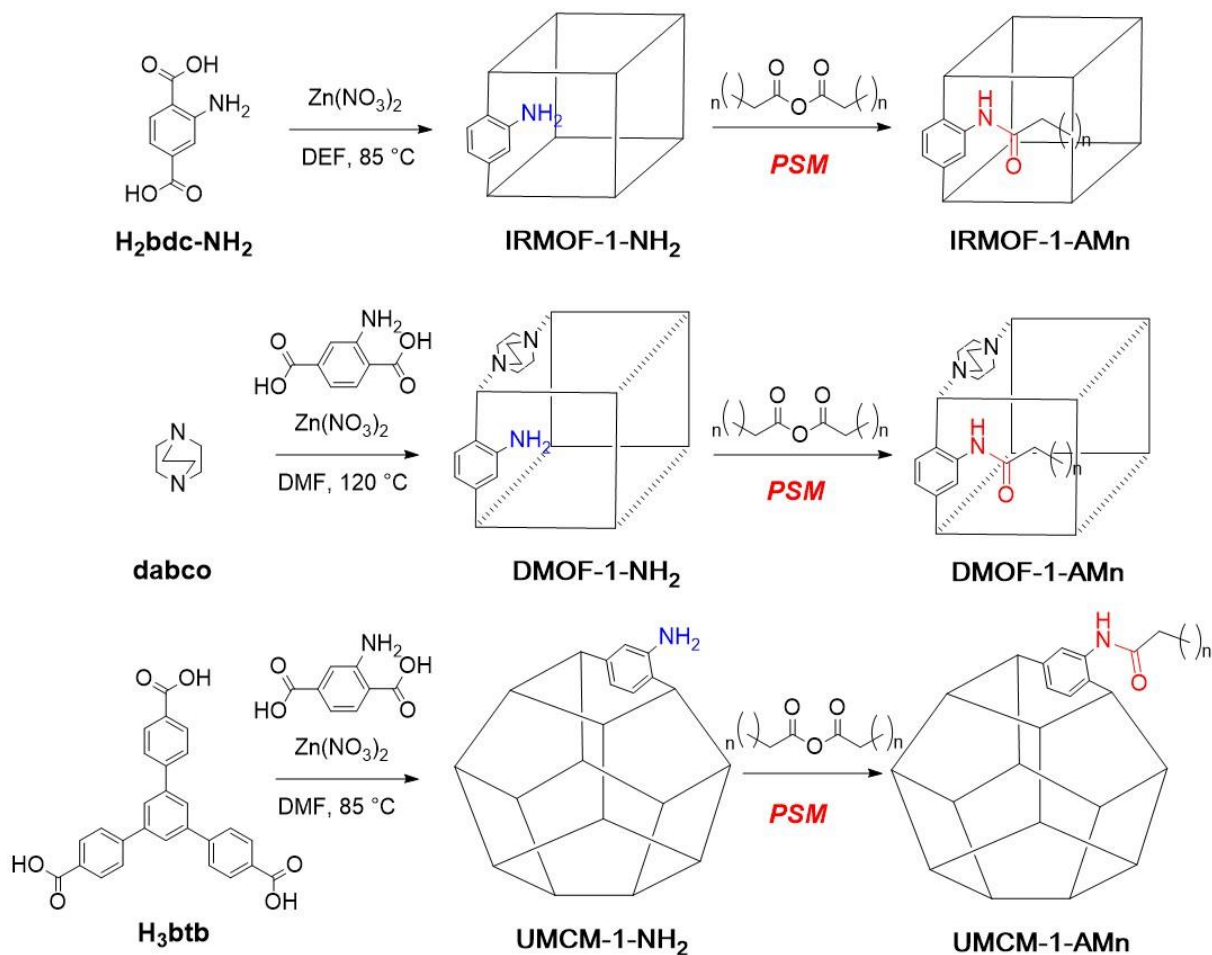


Figure 1-3 PSM on three amine-tagged MOFs. IRMOF-1-NH₂, DMOF-1-NH₂ and UMCM-1-NH₂ were transformed to IRMOF-1-AM_n, DMOF-1-AM_n and UMCM-1-AM_n by reactions between amine groups (blue) and alkyl anhydrides (the length of alkyl chain is denoted by n). The obtained MOFs contained amide bonds (red).

In addition to covalent-PSM (i.e., forming covalent bonds via PSM) on MOF linkers, metalation of functionalized ligands has been used extensively in MOF catalysis.³⁵ This type of PSM is achieved by metal addition to secondary binding sites on organic ligands, when the primary binding sites coordinate to MOF SBUs. For instance, the Lin group reported the synthesis of a homochiral MOF with bridging ligand (*R*)-6,6'-dichloro-2,2'-dihydroxy-1,1'-binaphthyl-4,4'-bipyridine.³⁶ The binaphthol sites of the bridging ligand were metalated with titanium isopropoxide ($\text{Ti}(\text{O}^i\text{Pr})_4$). And the resulting MOF proved to be a highly active asymmetric catalyst for the addition of ZnEt_2 to aromatic aldehydes. Due to the requirement for accessible secondary binding groups on bridging ligand, this metalation approach is always combined with other PSM methods when the secondary functional group is not compatible with MOF synthesis.

As another powerful postsynthetic method, PSE takes the advantage of kinetically dynamic nature of metal-ligand coordination bonds. PSE is employed to swap metal or ligand components in-and-out of MOFs (Figure 1-2 *bottom*). Metal ion exchange reactions have been successfully demonstrated for many different types of SBUs, particularly for polynuclear SBUs which impart high architectural stability to MOFs. For example, Zn^{2+} ions in the tetranuclear SBUs of MOF-5 can be replaced by a range of different metal ions including Ti^{3+} , V^{2+} , V^{3+} , Cr^{2+} , Cr^{3+} , Mn^{2+} , and Fe^{3+} .³⁷ These MOFs are not accessible by typical presynthetic pathways. In 2015, the Zhou group reported the formation of a bimetallic PCN-700 MOF with a decanuclear Zr_6M_4 ($\text{M} = \text{Ni}, \text{Co}$) SBU via PSE.¹⁹ Single crystallinity of the MOF was preserved throughout PSE and the structural transformation was evidenced by successive single-crystal

X-ray diffraction (SCXRD). In this case, the Zr^{4+} -O bond in PCN-700 is much more stable than Zn^{2+} -O bond in MOF-5 in the previous example, but PSE can still be achieved.

With respect to ligand PSE, also referred to as solvent-assisted ligand exchange (SALE), there are many impressive examples reported in recent years. In addition to the early reports of ligand PSE on pillared-paddlewheel MOFs³⁸⁻³⁹, the Cohen group demonstrated successful ligand PSE on UiO-66, with different functionalized linkers (Figure 1-4) to produce recyclable heterogeneous catalysts with enhanced catalytic properties.⁴⁰⁻⁴² For example, a diiron hydrogenase model catalyst is not stable at elevated temperature, and cannot be incorporated into MOFs via direct synthesis. Therefore, PSE method was used to integrate the catalyst into UiO-66 in H₂O at room temperature.⁴⁰ Chelating ligands like 2,3-dihydroxyterephthalic acid (CAT) and 2,3-dimercaptoterephthalic acid (TCAT) were also successfully incorporated into UiO-66 via one-step PSE process, followed by metalation to form catalytically active sites for different organic reactions. Both UiO-66-CAT and UiO-66-TCAT cannot be synthesized by direct solvothermal methods because of the coordination complexity between chelating groups and metal ions.⁴¹⁻⁴² Although bdc^{2-} derivatives were used in these reports, the same length of ligands is not essential for ligand PSE. In some cases, PSE has been used to afford the formation of isorecticular expanded MOFs with longer ligands. Rosi and coworkers reported sequential ligand exchange on bio-MOF-100 ($[Zn_8O_2(ad)_4(bpdc)_6]$, ad^- = adeninate, $bpdc^{2-}$ = 1,1'-biphenyl-4,4'-dicarboxylate]) for the preparation of a family of mesoporous MOFs.⁴³ The $bpdc^{2-}$ linkers in bio-MOF-100 are readily replaced by slightly longer azobenzene-4,4'-dicarboxylate ($abdc^{2-}$) and then the much longer 2'-amino-1,1':4,1''-terphenyl-4,4''-dicarboxylate (NH_2-tpdc^{2-}) to give the isorecticular expanded analog bio-MOF-102 and bio-MOF-103 in single-crystal to single-crystal transformations. It is of great significance that

neither bio-MOF-102 nor bio-MOF-103 can be directly synthesized by standard solvothermal methods.

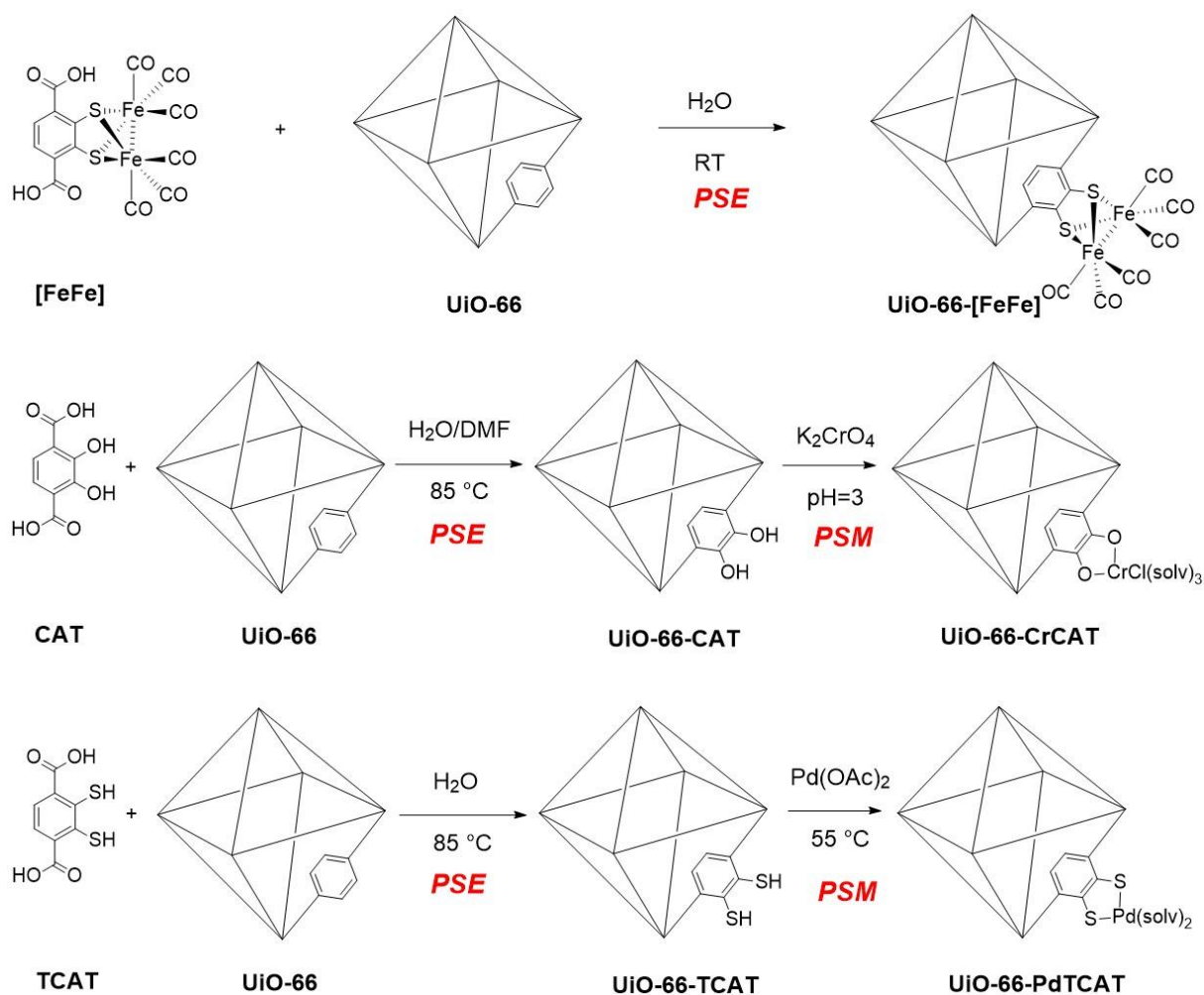


Figure 1-4 Schemes of PSE on UiO-66. *Top*: Incorporation of a hydrogenase model catalyst [FeFe] into UiO-66 via PSE. *Middle*: Incorporation of CAT ligand into UiO-66 via PSE, followed by metalation with Cr(III) to generate a catalytic MOF for oxidation reactions. *Bottom*: Incorporation of TCAT ligand into UiO-66 via PSE, followed by metalation with Pd(II) to generate a catalytic MOF for C-H bond activation.

1.2 MOFs as Heterogeneous Catalysts

The tunability of MOF and the readily accessible internal surface areas make MOFs excellent candidates as heterogeneous catalysts with many advantages.^{13, 44} These advantages

include: 1) a high density of catalytically active centers due to high surface area, 2) size- and shape-selectivity endowed by the well-defined pores and channels, 3) enhanced catalyst stability and reactivity due to spatial separation of catalytic sites, 4) easy tunability and modification of catalytic microenvironment, and 5) the possibility of investigating structure–activity relationship due to their high crystallinity. The first MOF catalysis report was published by Fujita in 1994,⁴⁵ and since then MOFs have gained increasing attention for catalysis applications. Three different approaches have been used to design and produce catalytically active sites in MOFs: 1) using catalytic metal salts to construct SBUs of the framework, 2) incorporating existing homogeneous catalysts, either organocatalysts or transition metal catalysts, into the organic linkers, and 3) loading MOFs with active species into pores (Figure 1-5). Because this thesis will include work related to MOF catalysis with SBUs and connecting ligands, the first two approaches for MOF-catalyst design will be discussed.

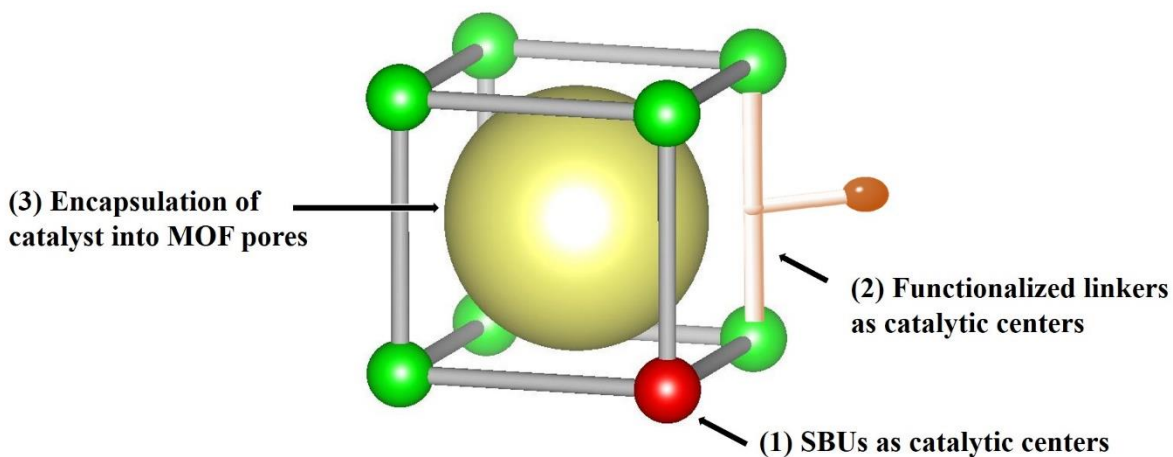


Figure 1-5 Schematic depiction of three approaches to design MOF catalyst. Regular MOF SBUs are denoted as green balls, and catalytic SBUs as red balls. Regular connecting ligands are denoted as grey sticks and catalytic linkers are orange sticks and balls. Yellow ball illustrates the open space in MOF pores.

1.2.1 SBUs as Catalytic Centers

MOFs with SBUs containing coordinatively unsaturated metal sites can strongly interact with organic molecules in catalysis. MIL-101(Cr), for example, was investigated by Kaskel and coworkers as a cyanosilylation catalyst.⁴⁶ The coordinated water molecules in MIL-101(Cr) are easily removed to expose Cr(III) sites, which act as a Lewis-acid catalyst for the addition of trimethylsilylcyanide (TMSCN) to benzaldehyde. Direct use of unsaturated metal sites in original MOFs like MIL-101(Cr) is a facile way for MOF catalysis. However, large amounts of MOFs contain metal SBUs without catalytic activity. In this condition, postsynthetic methods on MOF SBUs need to be employed to introduce catalytic active sites. Recently, the Dinca group demonstrated that SBUs in nickel-substituted MFU-4l (Ni-MFU-4l, MFU = Metal-organic Framework University of Ulm) can catalyze the selective dimerization of ethylene, which outperforms other reported hetero- and homogeneous catalysts.⁴⁷ The SBUs of parent MFU-4l contain a central Zn atom that is octahedrally coordinated by six nitrogen atoms, and four tetrahedral Zn²⁺ ions coordinated by three nitrogen atoms and a chloride. The four tetrahedral Zn atoms with scorpionate coordination were partially exchanged with Ni²⁺ ions via PSE method. The obtained Ni-MFU-4l exhibited high reactivity with a turnover frequency of 41,500 h⁻¹ and excellent selectivity for 1-butene production (>96%). The Zn atoms can also be replaced by other transition metals like Cr, Ti and V, and the resulting metal-exchanged derivatives of MFU-4l have been demonstrated to be catalytically active for several chemical transformations.⁴⁸⁻⁵⁰

1.2.2 Functionalized Linkers as Catalytic Sites

Functionalization of MOF organic linkers with catalytically active sites has been an attractive and straightforward strategy to design MOF-based heterogeneous catalyst. Metallosalen and metalloporphyrin ligands have been employed to prepare MOF catalysts because of their proven efficiency as homogeneous catalysts. For example, Hupp⁵¹, Ma⁵² and Zhou⁵³⁻⁵⁴ groups prepared Mn-/Co-/Fe-porphyrin-based MOFs, and illustrated their catalytic activities for oxidation reactions and CO₂ fixation reactions. In another report, the Zhang group developed a controllable synthesis of an anionic indium porphyrinic MOF, UNLPF-10 (UNLPF = University of Nebraska–Lincoln porous framework), which was metalated via in-situ metalation during MOF synthesis.⁵⁵ Oxygenation of sulfide was explored as a model reaction to investigate the photocatalytic ability of UNLPF-10. The rate of photooxygenation of thioanisole was found to increase as the ratio of MOF metalation increased.

Among functionalized ligands, polypyridyl Ru(II) and Ir(III) ‘metalloligand’ complexes have attracted increasing attention due to their exceptional photocatalytic ability.⁵⁶ In 2011, Lin and coworkers first incorporated polypyridyl Ru(II) and Ir(III) complexes into UiO-67 (Zr₆O₄(OH)₄(bpdc)₆) framework via a direct (mixed-ligand) synthesis method.⁵⁷ The resulting UiO-67 derivatives exhibited high surface areas, with ~2-3% of the ligand sites comprised of the polypyridyl photoactive catalytic sites. Aza-Henry reactions, oxidative coupling of amines, and oxidation of sulfides were reported to be catalyzed by these photocatalytic MOFs. The MOFs showed slightly lower activity compared to homogeneous catalysts, but exhibited good yields and reusability after three catalytic runs. In recent years, various organocatalysts and organometallic catalysts have been incorporated into MOF structures.⁵⁸ These reports demonstrate the possibilities to improve stability, activity and selectivity of catalysts by immobilizing them into MOF frameworks via facile presynthetic or postsynthetic methods.

This thesis will explore the functionalization of MOFs via both presynthetic and postsynthetic methods to produce catalytic MOFs for organic reactions. Catalytic MOFs as Micro- and nanomotors (MNM)s will also be investigated. In Chapter 2, polypyridyl Ru(II) complex was incorporated into a Zr-based MOF as active photocatalyst. The resulting UiO-67-Ru(bpy)₃ shows efficient and recyclable catalytic activity for aerobic oxidation of arylboronic acids under visible-light irradiation. In Chapter 3, Incorporation of polypyridyl Ir(III) complexes into a Zr-based MOF produced efficient photocatalyst for selective 2,2,2-trifluoroethylation of styrenes with the irradiation of visible light. Remarkably, when compared to the homogenous Ir(III) catalyst, the MOF-based photocatalyst showed reversal selectivity towards products. Confined space of MOF pores suppressed the dimerization of intermediate benzyl radicals, thus enhancing the selectivity of the desired hydroxytrifluoroethyl compounds. In Chapter 4, MOF SBUs was employed as catalytic sites for organic reactions. Specifically, Mn-based MOF CPF-5 was used as a highly efficient catalyst for C-H bond amination under mild conditions. Notably, CPF-5 is capable of aminating C-H bonds in an intermolecular fashion with high catalytic stability producing an unrivaled >10⁵ turnover. In addition, PSE of CPF-5 SBUs with transition metals, Fe and Co, which are known as better catalytic metals for C-H activation, will be discussed. Finally, Chapter 5 will discuss the synthesis of UiO-based self-propelled MNMs. Incorporation of a bipyridine ligand into the UiO-67 lattice transforms the crystallites, upon metalation, into single-site, metal-based catalytic ‘engines’ to power the micromotors with chemical fuel. The ‘engine performance’ (i.e. propulsion) of the single-site powered micromotors has been tuned by the choice of the metal ion utilized. In addition, a chemical ‘braking’ system was achieved by adding chelating agents capable of sequestering the metal ion engines and thereby suppressing the catalytic activity, with different chelators dis-

playing different deceleration capacities. These results demonstrate that MOFs can be powered by various engines and halted by different brakes, resulting in a high degree of motion design and control at nanoscale.

1.3 Acknowledgments

I thank Dr. Michael Denny Jr. for the assistance with Figure 1-1. Chapter 1 is, in part, a reprint of materials published in *CrystEngComm*: Xiao Yu, Le Wang and Seth M. Cohen*, “Photocatalytic Metal-Organic Frameworks for Organic Transformations”. *CrystEngComm*. **2017**, *19*, 4126-4136. The dissertation author was the primary researcher and writer for the paper. The permission to reproduce the paper was granted by the Royal Society of Chemistry, copyright 2017.

1.4 References

1. James, S. L., Metal-organic frameworks. *Chem. Soc. Rev.* **2003**, *32* (5), 276-288.
2. Eddaoudi, M.; Kim, J.; Rosi, N.; Vodak, D.; Wachter, J.; O'keeffe, M.; Yaghi, O. M., Systematic design of pore size and functionality in isoreticular MOFs and their application in methane storage. *Science* **2002**, *295* (5554), 469-472.
3. Serra-Crespo, P.; Ramos-Fernandez, E. V.; Gascon, J.; Kapteijn, F., Synthesis and characterization of an amino functionalized MIL-101 (Al): separation and catalytic properties. *Chem. Mater.* **2011**, *23* (10), 2565-2572.
4. Kandiah, M.; Nilsen, M. H.; Usseglio, S.; Jakobsen, S.; Olsbye, U.; Tilset, M.; Larabi, C.; Quadrelli, E. A.; Bonino, F.; Lillerud, K. P., Synthesis and stability of tagged UiO-66 Zr-MOFs. *Chem. Mater.* **2010**, *22* (24), 6632-6640.
5. Chui, S. S.-Y.; Lo, S. M.-F.; Charmant, J. P.; Orpen, A. G.; Williams, I. D., A chemically functionalizable nanoporous material [Cu₃(TMA)₂(H₂O)₃]_n. *Science* **1999**, *283* (5405), 1148-1150.

6. Park, K. S.; Ni, Z.; Côté, A. P.; Choi, J. Y.; Huang, R.; Uribe-Romo, F. J.; Chae, H. K.; O'Keeffe, M.; Yaghi, O. M., Exceptional chemical and thermal stability of zeolitic imidazolate frameworks. *PNAS*. **2006**, *103* (27), 10186-10191.
7. Li, J.-R.; Kuppler, R. J.; Zhou, H.-C., Selective gas adsorption and separation in metal-organic frameworks. *Chem. Soc. Rev.* **2009**, *38* (5), 1477-1504.
8. Rowsell, J. L.; Spencer, E. C.; Eckert, J.; Howard, J. A.; Yaghi, O. M., Gas adsorption sites in a large-pore metal-organic framework. *Science* **2005**, *309* (5739), 1350-1354.
9. Kreno, L. E.; Leong, K.; Farha, O. K.; Allendorf, M.; Van Duyne, R. P.; Hupp, J. T., Metal-organic framework materials as chemical sensors. *Chem. Rev.* **2011**, *112* (2), 1105-1125.
10. Horcajada, P.; Serre, C.; Vallet - Regí, M.; Sebban, M.; Taulelle, F.; Férey, G., Metal-organic frameworks as efficient materials for drug delivery. *Angew. Chem. Int. Ed.* **2006**, *118* (36), 6120-6124.
11. Huxford, R. C.; Della Rocca, J.; Lin, W., Metal-organic frameworks as potential drug carriers. *Curr. Opin. Chem. Biol.* **2010**, *14* (2), 262-268.
12. Gascon, J.; Corma, A.; Kapteijn, F.; Llabres i Xamena, F. X., Metal organic framework catalysis: quo vadis? *ACS Catal.* **2013**, *4* (2), 361-378.
13. Ma, L.; Abney, C.; Lin, W., Enantioselective catalysis with homochiral metal-organic frameworks. *Chem. Soc. Rev.* **2009**, *38* (5), 1248-1256.
14. Wang, Z.; Cohen, S. M., Postsynthetic modification of metal-organic frameworks. *Chem. Soc. Rev.* **2009**, *38* (5), 1315-1329.
15. Kirchon, A.; Feng, L.; Drake, H. F.; Joseph, E. A.; Zhou, H.-C., From fundamentals to applications: a toolbox for robust and multifunctional MOF materials. *Chem. Soc. Rev.* **2018**, *47* (23), 8611-8638.
16. Deng, H.; Doonan, C. J.; Furukawa, H.; Ferreira, R. B.; Towne, J.; Knobler, C. B.; Wang, B.; Yaghi, O. M., Multiple functional groups of varying ratios in metal-organic frameworks. *Science* **2010**, *327* (5967), 846-850.
17. Sun, Y.; Sun, L.; Feng, D.; Zhou, H. C., An In Situ One - Pot Synthetic Approach towards Multivariate Zirconium MOFs. *Angew. Chem. Int. Ed.* **2016**, *55* (22), 6471-6475.

18. Wang, L. J.; Deng, H.; Furukawa, H.; Gándara, F.; Cordova, K. E.; Peri, D.; Yaghi, O. M., Synthesis and characterization of metal–organic framework-74 containing 2, 4, 6, 8, and 10 different metals. *Inorg. Chem.* **2014**, *53* (12), 5881-5883.
19. Yuan, S.; Chen, Y. P.; Qin, J.; Lu, W.; Wang, X.; Zhang, Q.; Bosch, M.; Liu, T. F.; Lian, X.; Zhou, H. C., Cooperative cluster metalation and ligand migration in zirconium metal–organic frameworks. *Angew. Chem. Int. Ed.* **2015**, *54* (49), 14696-14700.
20. Liu, Q.; Cong, H.; Deng, H., Deciphering the spatial arrangement of metals and correlation to reactivity in multivariate metal–organic frameworks. *J. Am. Chem. Soc.* **2016**, *138* (42), 13822-13825.
21. Farha, O. K.; Mulfort, K. L.; Thorsness, A. M.; Hupp, J. T., Separating solids: Purification of metal-organic framework materials. *J. Am. Chem. Soc.* **2008**, *130* (27), 8598-8599.
22. Stock, N.; Biswas, S., Synthesis of metal-organic frameworks (MOFs): routes to various MOF topologies, morphologies, and composites. *Chem. Rev.* **2011**, *112* (2), 933-969.
23. Cohen, S. M., The postsynthetic renaissance in porous solids. *J. Am. Chem. Soc.* **2017**, *139* (8), 2855-2863.
24. Tanabe, K. K.; Cohen, S. M., Postsynthetic modification of metal–organic frameworks—a progress report. *Chem. Soc. Rev.* **2011**, *40* (2), 498-519.
25. Cohen, S. M., Postsynthetic methods for the functionalization of metal–organic frameworks. *Chem. Rev.* **2011**, *112* (2), 970-1000.
26. Wang, Z.; Cohen, S. M., Postsynthetic covalent modification of a neutral metal–organic framework. *J. Am. Chem. Soc.* **2007**, *129* (41), 12368-12369.
27. Tanabe, K. K.; Wang, Z.; Cohen, S. M., Systematic functionalization of a metal–organic framework via a postsynthetic modification approach. *J. Am. Chem. Soc.* **2008**, *130* (26), 8508-8517.
28. Garibay, S. J.; Wang, Z.; Tanabe, K. K.; Cohen, S. M., Postsynthetic modification: a versatile approach toward multifunctional metal-organic frameworks. *Inorg. Chem.* **2009**, *48* (15), 7341-7349.
29. Fracaroli, A. M.; Siman, P.; Nagib, D. A.; Suzuki, M.; Furukawa, H.; Toste, F. D.; Yaghi, O. M., Seven post-synthetic covalent reactions in tandem leading to enzyme-like complexity within metal–organic framework crystals. *J. Am. Chem. Soc.* **2016**, *138* (27), 8352-8355.

30. Burrows, A. D.; Frost, C. G.; Mahon, M. F.; Richardson, C., Post - Synthetic Modification of Tagged Metal–Organic Frameworks. *Angew. Chem. Int. Ed.* **2008**, *120* (44), 8610-8614.
31. Kawamichi, T.; Kodama, T.; Kawano, M.; Fujita, M., Single - Crystalline Molecular Flasks: Chemical Transformation with Bulky Reagents in the Pores of Porous Coordination Networks. *Angew. Chem. Int. Ed.* **2008**, *120* (42), 8150-8152.
32. Huang, A.; Caro, J., Covalent post - functionalization of zeolitic imidazolate framework ZIF - 90 membrane for enhanced hydrogen selectivity. *Angew. Chem. Int. Ed.* **2011**, *50* (21), 4979-4982.
33. Burrows, A. D.; Frost, C. G.; Mahon, M. F.; Richardson, C., Sulfur-tagged metal–organic frameworks and their post-synthetic oxidation. *Chem. Commun.* **2009**, *0* (28), 4218-4220.
34. Jiang, H.-L.; Feng, D.; Liu, T.-F.; Li, J.-R.; Zhou, H.-C., Pore surface engineering with controlled loadings of functional groups via click chemistry in highly stable metal–organic frameworks. *J. Am. Chem. Soc.* **2012**, *134* (36), 14690-14693.
35. Evans, J. D.; Sumby, C. J.; Doonan, C. J., Post-synthetic metalation of metal–organic frameworks. *Chem. Soc. Rev.* **2014**, *43* (16), 5933-5951.
36. Wu, C.-D.; Hu, A.; Zhang, L.; Lin, W., A homochiral porous metal-organic framework for highly enantioselective heterogeneous asymmetric catalysis. *J. Am. Chem. Soc.* **2005**, *127* (25), 8940-8941.
37. Brozek, C. K.; Dincă, M., Ti³⁺-, V^{2+/3+}-, Cr^{2+/3+}-, Mn²⁺-, and Fe²⁺-substituted MOF-5 and redox reactivity in Cr- and Fe-MOF-5. *J. Am. Chem. Soc.* **2013**, *135* (34), 12886-12891.
38. Burnett, B. J.; Barron, P. M.; Hu, C.; Choe, W., Stepwise synthesis of metal–organic frameworks: replacement of structural organic linkers. *J. Am. Chem. Soc.* **2011**, *133* (26), 9984-9987.
39. Xu, Y.; Vermeulen, N. A.; Liu, Y.; Hupp, J. T.; Farha, O. K., SALE - Ing a MOF - Based “ Ship of Theseus. ” Sequential Building - Block Replacement for Complete Reformulation of a Pillared - Paddlewheel Metal - Organic Framework. *Eur. J. Inorg. Chem.* **2016**, *2016* (27), 4345-4348.

40. Pullen, S.; Fei, H.; Orthaber, A.; Cohen, S. M.; Ott, S., Enhanced photochemical hydrogen production by a molecular diiron catalyst incorporated into a metal–organic framework. *J. Am. Chem. Soc.* **2013**, *135* (45), 16997-17003.
41. Fei, H.; Shin, J.; Meng, Y. S.; Adelhardt, M.; Sutter, J. r.; Meyer, K.; Cohen, S. M., Reusable oxidation catalysis using metal-monocatecholato species in a robust metal–organic framework. *J. Am. Chem. Soc.* **2014**, *136* (13), 4965-4973.
42. Fei, H.; Cohen, S. M., Metalation of a thiocatechol-functionalized Zr (IV)-based metal–organic framework for selective C–H functionalization. *J. Am. Chem. Soc.* **2015**, *137* (6), 2191-2194.
43. Li, T.; Kozłowski, M. T.; Doud, E. A.; Blakely, M. N.; Rosi, N. L., Stepwise ligand exchange for the preparation of a family of mesoporous MOFs. *J. Am. Chem. Soc.* **2013**, *135* (32), 11688-11691.
44. Lee, J.; Farha, O. K.; Roberts, J.; Scheidt, K. A.; Nguyen, S. T.; Hupp, J. T., Metal–organic framework materials as catalysts. *Chem. Soc. Rev.* **2009**, *38* (5), 1450-1459.
45. Fujita, M.; Kwon, Y. J.; Washizu, S.; Ogura, K., Preparation, clathration ability, and catalysis of a two-dimensional square network material composed of cadmium (II) and 4, 4'-bipyridine. *J. Am. Chem. Soc.* **1994**, *116* (3), 1151-1152.
46. Henschel, A.; Gedrich, K.; Kraehnert, R.; Kaskel, S., Catalytic properties of MIL-101. *Chem. Commun.* **2008**, (35), 4192-4194.
47. Metzger, E. D.; Brozek, C. K.; Comito, R. J.; Dincă, M., Selective dimerization of ethylene to 1-butene with a porous catalyst. *ACS Cent. Sci.* **2016**, *2* (3), 148-153.
48. Comito, R. J.; Fritzsche, K. J.; Sundell, B. J.; Schmidt-Rohr, K.; Dincă, M., Single-site heterogeneous catalysts for olefin polymerization enabled by cation exchange in a metal–organic framework. *J. Am. Chem. Soc.* **2016**, *138* (32), 10232-10237.
49. Metzger, E. D.; Comito, R. J.; Hendon, C. H.; Dincă, M., Mechanism of Single-Site Molecule-Like Catalytic Ethylene Dimerization in Ni-MFU-4 l. *J. Am. Chem. Soc.* **2017**, *139* (2), 757-762.
50. Comito, R. J.; Wu, Z.; Zhang, G.; Lawrence III, J. A.; Korzyński, M. D.; Kehl, J. A.; Miller, J. T.; Dincă, M., Stabilized Vanadium Catalyst for Olefin Polymerization by Site Isolation in a Metal–Organic Framework. *Angew. Chem. Int. Ed.* **2018**, *57* (27), 8135-8139.

51. Takaishi, S.; DeMarco, E. J.; Pellin, M. J.; Farha, O. K.; Hupp, J. T., Solvent-assisted linker exchange (SALE) and post-assembly metallation in porphyrinic metal–organic framework materials. *Chem. Sci.* **2013**, *4* (4), 1509-1513.
52. Meng, L.; Cheng, Q.; Kim, C.; Gao, W. Y.; Wojtas, L.; Chen, Y. S.; Zaworotko, M. J.; Zhang, X. P.; Ma, S., Crystal Engineering of a Microporous, Catalytically Active fcu Topology MOF Using a Custom - Designed Metalloporphyrin Linker. *Angew. Chem. Int. Ed.* **2012**, *51* (40), 10082-10085.
53. Feng, D.; Gu, Z. Y.; Li, J. R.; Jiang, H. L.; Wei, Z.; Zhou, H. C., Zirconium - metalloporphyrin PCN - 222: mesoporous metal - organic frameworks with ultrahigh stability as biomimetic catalysts. *Angew. Chem. Int. Ed.* **2012**, *51* (41), 10307-10310.
54. Zhang, L.; Yuan, S.; Feng, L.; Guo, B.; Qin, J. S.; Xu, B.; Lollar, C.; Sun, D.; Zhou, H. C., Pore - Environment Engineering with Multiple Metal Sites in Rare - Earth Porphyrinic Metal - Organic Frameworks. *Angew. Chem. Int. Ed.* **2018**, *57* (18), 5095-5099.
55. Johnson, J. A.; Zhang, X.; Reeson, T. C.; Chen, Y.-S.; Zhang, J., Facile control of the charge density and photocatalytic activity of an anionic indium porphyrin framework via in situ metalation. *J. Am. Chem. Soc.* **2014**, *136* (45), 15881-15884.
56. Shaw, M. H.; Twilton, J.; MacMillan, D. W., Photoredox catalysis in organic chemistry. *J. Org. Chem.* **2016**, *81* (16), 6898-6926.
57. Wang, C.; Xie, Z.; deKrafft, K. E.; Lin, W., Doping metal–organic frameworks for water oxidation, carbon dioxide reduction, and organic photocatalysis. *J. Am. Chem. Soc.* **2011**, *133* (34), 13445-13454.
58. Yoon, M.; Srirambalaji, R.; Kim, K., Homochiral metal–organic frameworks for asymmetric heterogeneous catalysis. *Chem. Rev.* **2011**, *112* (2), 1196-1231.

**Chapter 2 : Photocatalytic Metal-Organic Frameworks for Aerobic Oxidation of
Arylboronic Acids**

2.1 Introduction

Photoactive MOFs have attracted increasing attention for use in a variety of catalytic applications.¹ Mahata et al. first reported the use of a MOF as a photocatalyst to degrade organic pollutants in 2006.² The majority of studies on photoactive MOFs have focused on functionalization of MOFs to achieve light harvesting and drive H₂ evolution and CO₂ reduction.³ Li and co-workers incorporated Ru carbonyl complex for photocatalytic CO₂ reduction under visible-light irradiation.⁴ The ability of amine-functionalized MOFs to undergo photoinduced charge separation was demonstrated in several reports, exhibiting photochemical CO₂ reduction activities.⁵⁻⁹ In other studies, MOFs were shown to catalyze organic transformations under light irradiation.¹⁰ Duan and co-workers incorporated a triphenylamine photoredox group into Zn-based MOFs, which can catalyze a light-driven α -alkylation reaction.¹¹

During the last decade, Ru(bpy)₃ and related complexes have been shown to be efficient photocatalysts for organic synthesis.¹² The Yoon and MacMillan groups first employed Ru(bpy)₃ to perform [2+2] cycloadditions¹³ and α -alkylation of aldehydes,¹⁴ respectively. Stephenson and co-workers disclosed a photoredox reductive dehalogenation of activated alkyl halides mediated by Ru(bpy)₃.¹⁵ Ru(bpy)₃ and Ir(ppy)₃ have also been used in aza-Henry reactions,¹⁶ aerobic amine coupling,¹⁷ hydroxylation of arylboronic acids,¹⁸ sulfide oxidation,¹⁹ and radical chemistry.²⁰ Considering the high cost of these precious metal-based photocatalysts, a heterogeneous, easily reusable system could be of substantial value.

To produce such a recyclable catalyst, functionalization of MOF linkers with Ru or Ir catalytic sites has proven to be an efficient approach, as discussed in chapter 1. The Lin group reported doping MOFs with Ru and Ir complexes via direct solvothermal synthesis to produce

MOFs that can catalyze the aza-Henry reaction, an amine coupling reaction, and oxidation of thioanisole.²¹ In addition to this important report, there remain many other reactions of interest and improvements to the catalyst performance, crystallinity, and loading of catalytic sites that are yet to be achieved.

MOFs with the ability to catalyze aerobic oxidations have been developed in recent years, which utilize molecular oxygen as a green oxidant.²²⁻²³ Herein, we incorporate a Ru photocatalyst into a robust UiO-67 (UiO = University of Oslo) framework via postsynthetic modification (PSM) to get nearly quantitative metal loadings with retention of crystallinity and porosity. The resulting MOFs exhibit efficient photocatalytic activity for aerobic oxidation of arylboronic acids to the corresponding phenols under light irradiation. Importantly, MOFs serve as a matrix to enhance the stability of the active sites, achieving recyclable catalytic performance over five cycles without significant loss of activity.

2.2 Synthesis and Characterization of MOFs Incorporated with Polypyridyl Ruthenium Photocatalyst

The robust UiO-67 framework, consisting of Zr(IV)-based secondary building blocks ($\text{Zr}_6\text{O}_4(\text{OH})_4$) and biphenyl ligands, was selected as a platform to incorporate $[\text{Ru}(\text{bpy})_2(\text{dcbpy})]^{2+}$ (bis(2,2'-bipyridine)(5,5'-dicarboxy-2,2'-bipyridine)ruthenium(II)). Attempts to directly synthesize UiO-67-Ru(bpy)₃ gave low loadings of Ru, presumably due to the steric bulk of the complex.²¹ We also employed a postsynthetic exchange (PSE) approach²⁴ to substitute the biphenyl ligand in UiO-67 with $[\text{Ru}(\text{bpy})_2(\text{H}_2\text{dcbpy})]\text{Cl}_2$; however, no enhancement of Ru loading, compared to direct synthesis, was observed under the PSE

conditions used (85 °C for 24 h in DMF, MeCN, or EtOH/H₂O). Therefore, we turned to PSM to improve the incorporation of the Ru(II) complex (Figure 2-1).

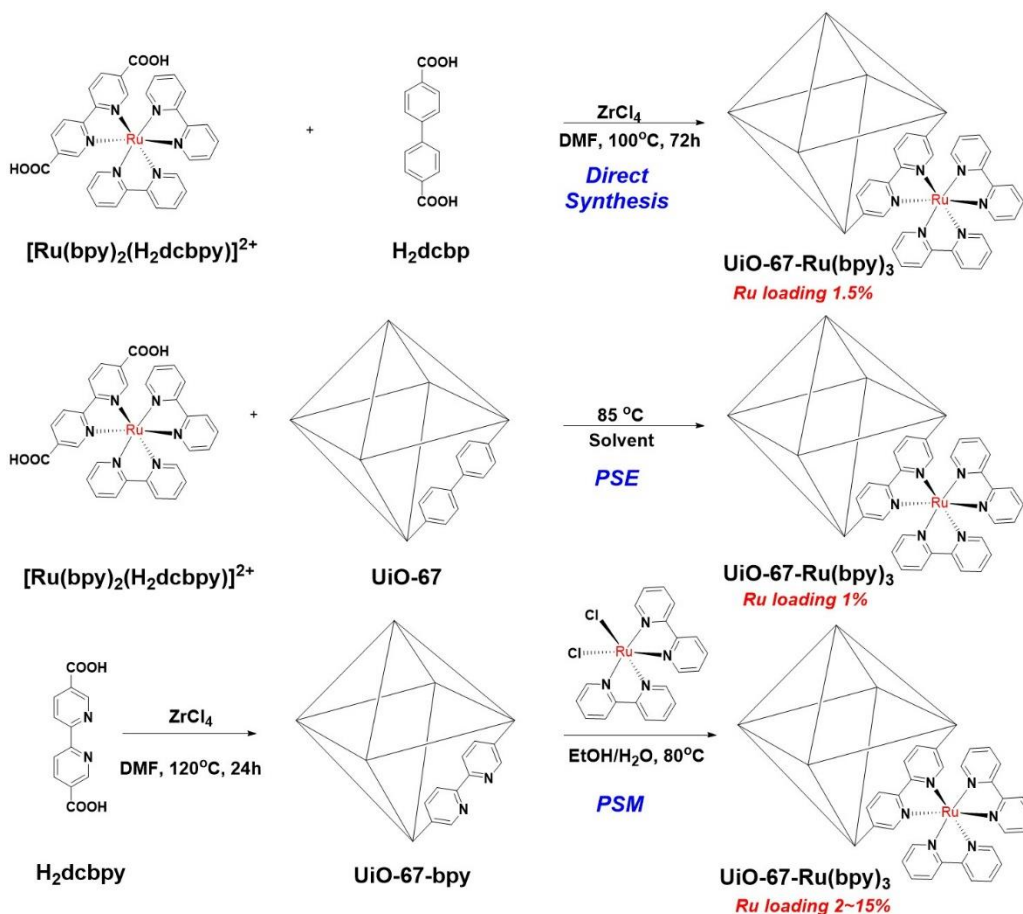


Figure 2-1 Synthesis of UiO-67-Ru(bpy)₃ using three different synthetic strategies.

Using a mixed-ligand strategy, H₂dcbpy ([2,2'-bipyridine]-5,5'-dicarboxylic acid) and H₂dcbp ([1,1'-biphenyl]-4,4'-dicarboxylic acid) were used to obtain a MOF containing both ligands.²⁵ Solvothermal synthesis using a molar ratio of 1:3 of H₂dcbpy and H₂dcbp with ZrCl₄ and benzoic acid (as a modulator) in DMF at 120 °C for 24 h gave a UiO-67 derivative containing ~25% of the dcbpy²⁻ ligand (UiO-67-bpy_{0.25}). Postsynthetic modification (PSM, Figure 2-1) via a metalation of this MOF with 0.3 equivalents of Ru(bpy)₂Cl₂ in EtOH/H₂O at 80 °C for 2 h, followed by centrifugation and washing with fresh EtOH for 3 days, afforded the

desired UiO-67-Ru(bpy)₃ with ~10% Ru loading (UiO-67-[Ru(bpy)₃]_{0.1}). PSM metalation of UiO-67 derivatives containing a higher percentage of dcbpy²⁻ (50~100%) resulted in a loss of framework stability, as evidenced by powder X-ray diffraction (PXRD, Figure 2-4).

The formation of Ru complexes and the degree of PSM were clearly characterized by ¹H NMR after digesting UiO-67-Ru(bpy)₃ in D₃PO₄/d₆-DMSO. This analysis was possible because Ru(bpy)₂(dcbpy) remains intact under these MOF digestion conditions. Integration of the proton resonances for Ru(bpy)₂(dcbpy) and dcbp²⁻ confirmed the degree of Ru modification, which could be tuned from 2% to 15% by varying the reaction time from 1~24 h (Figure 2-2). PXRD confirmed the retention of the UiO-67 topology (Figure 2-3) after metalation. The TGA trace of UiO-67-[Ru(bpy)₃]_{0.1} exhibits a decomposition temperature of ~400 °C, which is ~100 °C lower than that of the unmetalated MOF (Figure 2-5). In addition, UiO-67-[Ru(bpy)₃]_{0.1} exhibited a BET surface area of 1803±164 m²/g, which is high, but lower than the BET surface area of the parent MOF UiO-67-bpy_{0.25} (2425±25 m²/g, Figure 2-6).

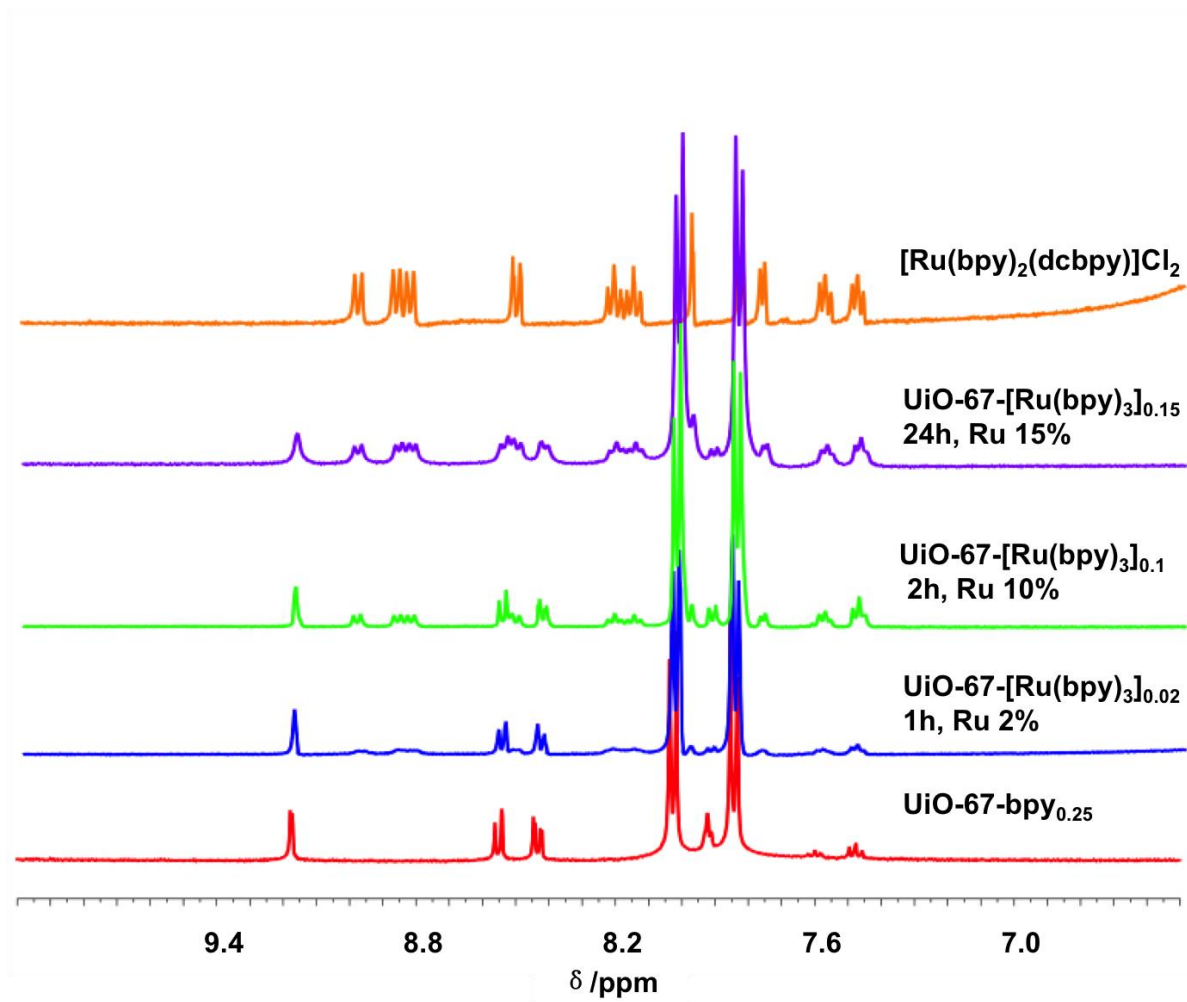


Figure 2-2 ^1H NMR ($\text{D}_3\text{PO}_4/\text{d}^6\text{-DMSO}$ digested) of UiO-67- $\text{Ru}(\text{bpy})_3$ containing different amount of Ru complex.

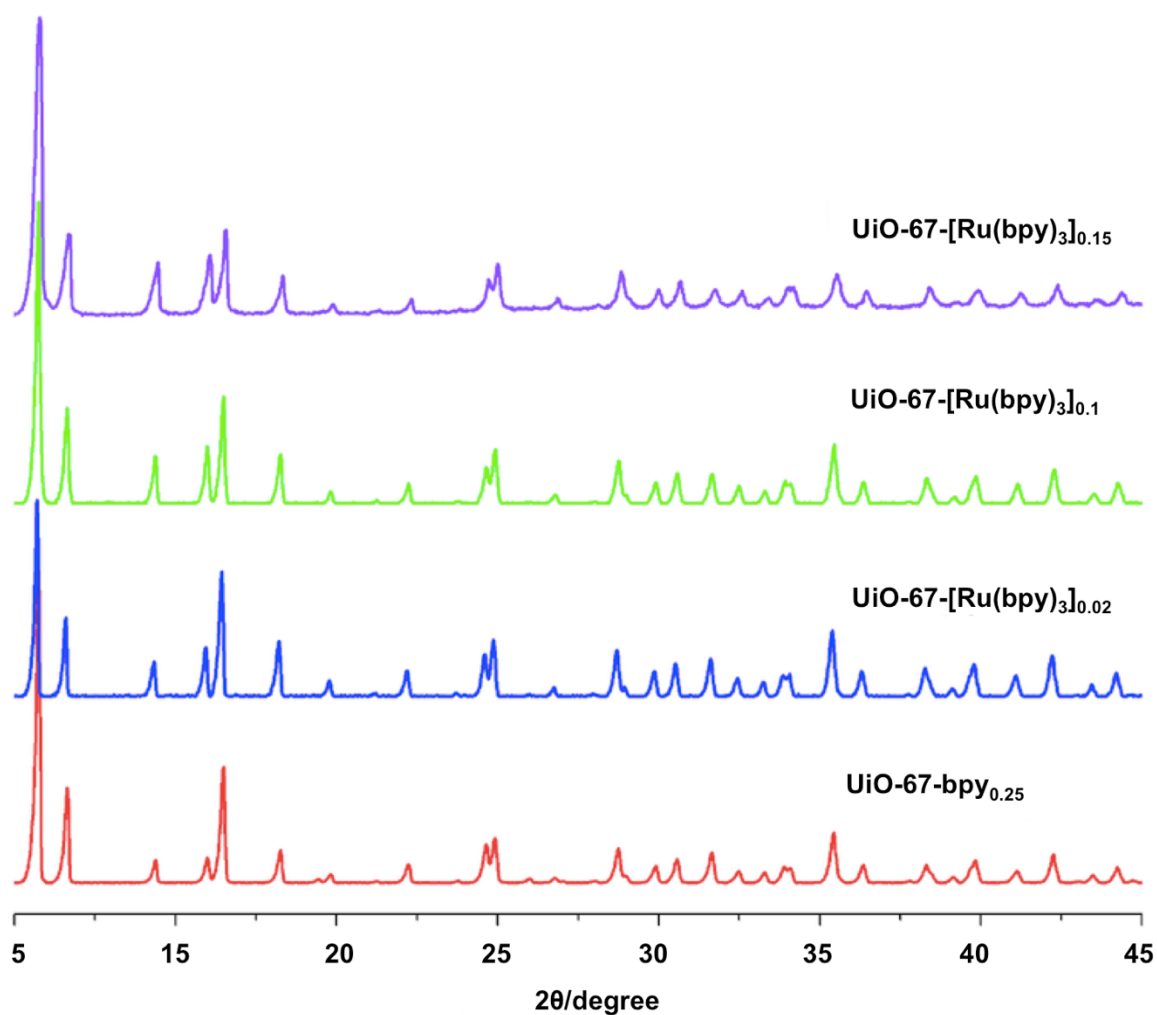


Figure 2-3 PXRD of UiO-67-Ru(bpy)₃ containing different amount of Ru complex.

2.3 MOF Catalysis for Aerobic Oxidation of Arylboronic Acids

It is well known that phenols are among the most important intermediates and building blocks in the pharmaceutical and chemical industry.²⁶ Arylboronic acids can be hydroxylated by strong oxidizing agents such as oxone, hydrogen peroxide, or *meta*-chloroperoxybenzoic acid (MCPBA), which are usually used in stoichiometric amounts and carefully controlled to avoid over-oxidation.²⁷⁻³⁰ In pursuit of environmentally friendly methods, Cu(II) and Pd(II)

catalysts have been investigated for oxidative hydroxylation of arylboronic acids with molecular oxygen, albeit using a stoichiometric strong base (KOH or NaOH).³¹⁻³³ Scaiano et al. reported the photocatalytic hydroxylation of boronic acids with methylene blue as photosensitizer with high efficiency.³⁴ Xiao and co-workers reported photocatalytic aerobic oxidative hydroxylation mediated by a Ru complex.¹⁸ However, the use of a homogeneous $\text{Ru}(\text{bpy})_3^{2+}$ catalyst poses challenges including product separation and high cost. Herein, UiO-67- $[\text{Ru}(\text{bpy})_3]_{0.1}$ is shown to act as an efficient and recyclable heterogeneous photocatalyst for aerobic oxidative hydroxylation of arylboronic acids.

As a benchmark reaction, phenylboronic acid was chosen as a substrate. As shown in Table 2-1, incubating a mixture of phenylboronic acid, *N,N*-diisopropylethylamine (*i*Pr₂NEt), and UiO-67- $[\text{Ru}(\text{bpy})_3]_{0.1}$ as catalyst in MeOH using a photochemical reactor ($\lambda = 365$ nm) led to an ~81% yield of phenol after 24 h. Other solvents, such as DMF, H₂O, and CH₃CN produced lower yields than obtained in MeOH. The overall yield (81%) using UiO-67- $[\text{Ru}(\text{bpy})_3]_{0.1}$ is good, but slightly lower than a homogeneous reference system ($\text{Ru}(\text{bpy})_3\text{Cl}_2$, yield ~95%). The lower yield may be due to incomplete light penetration through the MOF material. Interestingly, pristine UiO-67- $\text{bpy}_{0.25}$ gave ~22% conversion under irradiation with UV light after 1 day, indicating a photocatalytic ability similar to ZrO_2 .³⁵ However, a control experiment with no photocatalyst showed no conversion upon UV and visible light irradiation (Table 2-1, Entry 4). No product was observed when the reaction was carried out in the absence of light even in the presence of photocatalyst (Table 2-1, Entry 5), confirming the photochemical nature of this oxidation. O₂ was confirmed to be the oxidizing agent, as a control reaction under an N₂ atmosphere also gave no product (Table 2-1, Entry 6). Heterogeneity of UiO-67- $[\text{Ru}(\text{bpy})_3]_{0.1}$ was confirmed by filtration of the catalyst after 4h (Yield 10%), resulting in no further increase

on product after 44h. This suggests that UiO-67-[Ru(bpy)₃]_{0.1} is a true heterogeneous catalyst with no catalytically active species released into the solution.

Table 2-1 Summary of results for the aerobic oxidative hydroxylation of arylboronic acids using UiO-67-[Ru(bpy)₃]_{0.1} as catalyst.^a

Entry	Catalyst	Light	Atmosphere	Yield (%) ^b	Yield (%) ^c
1	UiO-67-[Ru(bpy) ₃] _{0.1}	+	Air	81(7)	77(3)
2	Ru(bpy) ₃ Cl ₂	+	Air	>95	>95
3	UiO-67-bpy _{0.25}	+	Air	22(2)	0
4	None	+	Air	0	0
5	UiO-67-[Ru(bpy) ₃] _{0.1}	-	Air	0	0
6	UiO-67-[Ru(bpy) ₃] _{0.1}	+	N ₂	0	0

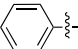
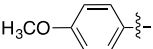
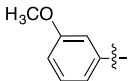
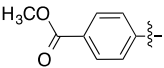
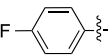
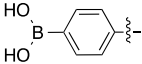
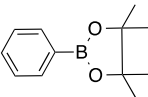
^a Reaction conditions: phenylboronic acid (0.5 mmol), *N,N*-diisopropylethylamine (0.6 mmol), UiO-67-[Ru(bpy)₃]_{0.1} = [Ru] (5 mol%) in 5 mL MeOH open to air with light irradiation at room temperature for 24 h. ^b λ = 365 nm. ^c 23W compact fluorescent bulb. ^{b,c} Yield is based on ¹H NMR analysis.

To examine recyclability, experiments were performed using the same batch of MOF for the oxidation of 4-methoxyphenylboronic acid for 48 h over five successive catalytic cycles. Between each run, the catalyst was recovered by centrifugation, washed with MeOH, and dried under vacuum at room temperature. The catalyst gave good yields, albeit with slightly lower activity after the fourth run (Figure 2-7, 2-8). The lower yield may be due to some loss in the Ru species (see ICP-OES results below), or simply due to incomplete recovery of the catalyst materials over several cycles. Importantly, the robust nature of the UiO-67 platform allowed the photocatalyst to be highly stable even under the mildly basic reaction conditions required (as confirmed by PXRD, Figure 2-9). ¹H NMR showed that there is minimal leaching of the

Ru complex from the MOF after one catalytic run (Figure 2-10; although a small degree of dcbp²⁻ ligand was observed in the reaction solution, Figure 2-11). After 5 cycles, inductively coupled plasma-optical emission spectroscopy (ICP-OES) confirmed an atomic ratio of 1:0.106 (Zr/Ru), ~10% lower than fresh UiO-67-[Ru(bpy)₃]_{0.1} which gave an atomic ratio of 1:0.118 (Zr/Ru).

Table 2-2 Scope of substrate conversion using UiO-67-[Ru(bpy)₃]_{0.1} as catalyst.

$$\text{Ar}-\text{B} \begin{matrix} \text{OH} \\ | \\ \text{OH} \end{matrix} \xrightarrow[\text{MeOH, RT, 48h, } h\nu]{i\text{Pr}_2\text{NEt, [Ru]}} \text{Ar}-\text{OH}$$

Entry	Ar-	Yield (%) ^a	Yield (%) ^b
1		81(7)	80(5)
2		74(2)	72(2)
3		76(3)	70(2)
4		>95	>95
5		50(5)	47(3)
6		20(3)	15(2)
7		>95	91(1)

^a $\lambda = 365 \text{ nm}$. ^b 23W compact fluorescent bulb. ^{a, b} Yield determined by ¹H NMR from three independent experiments.

The scope of near-UV and visible light-induced photocatalytic aerobic oxidative hydroxylation of arylboronic acids is summarized in Table 2 (Figure 2-12 ~ 2-16). The majority of substrates were oxidized to aryl alcohols in good to excellent yields, while conversions under

irradiation of visible light are a little lower than UV light, probably due to weaker power of visible-light source. A higher conversion efficiency was observed when treating with electron-rich arylboronic acids (Table 2-2, Entry 2-4). (4-Fluorophenyl)boronic acid (Table 2-2, Entry 5) shows lower yield, which is consistent with homogeneous system.¹⁸ 1,4-Phenylenediboronic acid also proved to be suitable substrate for this reaction, but with a lower conversion (~20%) for In conclusion, an example of a heterogeneous photocatalyst for the aerobic oxidative hydroxylation of arylboronic acids was prepared by incorporating polypyridyl ruthenium complexes into a UiO-67 MOF via a combination of using a mixed ligand MOF with PSM. The synthesized UiO-67-[Ru(bpy)₃]_{0.1} photocatalyst is stable and active over several cycles, providing a platform to recover and reuse this precious metal-containing catalyst.

2.4 Conclusion

In conclusion, an example of a heterogeneous photocatalyst for the aerobic oxidative hydroxylation of arylboronic acids was prepared by incorporating polypyridyl ruthenium complexes into a UiO-67 MOF via a combination of using a mixed ligand MOF with PSM. The synthesized UiO-67-[Ru(bpy)₃]_{0.1} photocatalyst is stable and active over several cycles, providing a platform to recover and reuse this precious metal-containing catalyst.

2.5 Experimental

General Methods

Starting materials and solvents were purchased and used without further purification from commercial suppliers (Sigma-Aldrich, Alfa Aesar, EMD, TCI, Cambridge Isotope Laboratories, Inc., and others). Proton nuclear magnetic resonance spectra (¹H NMR) were recorded on a

Varian FT-NMR spectrometer (400 MHz). Chemical shifts were quoted in parts per million (ppm) referenced to the appropriate solvent peak or 0 ppm for TMS. A Rayonet Photochemical reactor (Model RPR-200) was used for photocatalysis reactions equipped with near-UV lamps ($\lambda = 365$ nm). Compact fluorescent bulb (23W, 1600lumen) was used as visible-light source. Centrifugation was performed using a Beckman Coulter Allegra X-22R Centrifuge, with a fixed-angle rotor at 6800 rpm for 10 min.

Experimental Procedures

Synthesis of UiO-67-bpy_{0.25}. ZrCl₄ (120 mg, 0.514 mmol), benzoic acid (1.88g, 15.4 mmol), H₂bpdC (biphenyldicarboxylic acid, 94 mg, 0.39 mmol), and H₂bpydc (2,2'-bipyridine-5,5'-dicarboxylic acid, 31 mg, 0.13 mmol) were placed in a vial with 20 mL of DMF. The solids were dispersed via sonication for ~10 min, followed by incubation at 120 °C for 24 h. After cooling, solids were collected by centrifugation and the solvent was decanted. The solids were washed with DMF (2×20 mL), followed by soaking in ethanol (EtOH) for 3 d, and the solution was exchanged with fresh EtOH (10 mL) every 24 h. After 3 d of soaking, the solids were collected via centrifugation and dried under vacuum.

Using PSM to prepare UiO-67-[Ru(bpy)₃]_{0.1}. UiO-67-bpy_{0.25} (35.5 mg, 0.1 mmol) and *cis*-Ru(bpy)₂Cl₂ (*cis*-bis(2,2'-bipyridine)dichlororuthenium(II) hydrate) (14.6 mg, 0.03 mmol) were placed in a scintillation vial with 1 mL EtOH and 1 mL H₂O. The solids were dispersed via sonication for ~10 min, followed by incubation at 80 °C for 2 h. After cooling, solids were collected by centrifugation and the solvent was decanted. The solids were washed once with H₂O (20 mL) and twice with EtOH (20 mL), followed by soaking in EtOH for 3 d, with the

solution exchanged with fresh EtOH (10 mL) every 24 h. After 3 d of soaking, the solids were collected via centrifugation and dried under vacuum.

Aerobic oxidation reaction catalyzed by UiO-67-[Ru(bpy)₃]_{0.1}. Arylboronic acid (0.5 mmol), *N,N*-diisopropylethylamine (0.6 mmol), and UiO-67-[Ru(bpy)₃]_{0.1} (100 mg, 5 mol%) were placed in a 20 mL round-bottom flask with 5 mL MeOH. After sonication for 10 min, the flask was opened to air and put into a photoreactor ($\lambda = 365$ nm) equipped with a cooling fan for 24 h. For visible-light reaction, a 23W compact fluorescent bulb (1600 lumen) was put under the round-bottom flask at 5 cm distance in a fume hood. A condenser was connected to the round-bottom flask to prevent solvent evaporation. After the reaction was complete, the supernatant was separated by centrifugation and evaporated before being analyzed by ¹H NMR (in CD₃OD). Some leaching of biphenyl dicarboxylic acid ligand is observed in analysis, and control experiments were performed by soaking UiO-67-[Ru(bpy)₃]_{0.1} in reactants solution without photoredox catalysis (no light) (see Figure 2-11). To test recyclability, the supernatant was decanted from the catalyst after 48 h reaction and the catalyst was washed with MeOH (3 × 10 mL). The washed MOFs were directly used for the next round oxidation catalysis for the same substrate.

Powder X-ray Diffraction (PXRD) Analysis. ~20–30 mg of UiO-67-bpy material was dried under vacuum prior to PXRD analysis. PXRD data were collected at ambient temperature on a Bruker D8 Advance diffractometer at 40 kV, 40 mA for Cu K α ($\lambda = 1.5418$ Å), with a scan speed of 1 sec/step, a step size of 0.02° in 2 θ , and a 2 θ range of ~5 to 45° (sample dependent). The experimental background was corrected using the Jade 5.0 software package.

Digestion and Analysis by ¹H NMR. ~10 mg of UiO-67-bpy material was dried under vacuum and digested with sonication in 600 μ L *d*₆-DMSO and 10 μ L of 40% HF.

Approximately 10 mg UiO-67-Ru(bpy)₃ was suspended in a 0.1 M solution (1 mL) of D₃PO₄ in D₂O/*d*₆-DMSO (prepared by mixing 11.9 mg of a solution of D₃PO₄ (85% in D₂O) with 1 mL *d*₆-DMSO) and stirred at room temperature for 5 h. The solution was filtered through cotton and placed in an NMR tube.

BET Surface Area Analysis. ~50 mg of UiO-67-bpy material was evacuated on a vacuum line overnight at room temperature. The sample was then transferred to a pre-weighed sample tube and degassed at 105 °C on an Micromeritics ASAP 2020 Adsorption Analyzer for a minimum of 12 h or until the outgas rate was <5 mm Hg. The sample tube was re-weighed to obtain a consistent mass for the degassed exchanged MOF. BET surface area (m²/g) measurements were collected at 77 K by N₂ on a Micromeritics ASAP 2020 Adsorption Analyzer using the volumetric technique, and the surface areas reported for each material is the average of three independent samples.

Thermalgravimetric Analysis. ~10-15 mg of UiO-67-bpy material was used for TGA measurements, after BET analysis (activated). Samples were analyzed under a stream of N₂ using a TA Instrument Q600 SDT running from room temperature to 800 °C with a scan rate of 5 °C/min.

2.6 Appendix

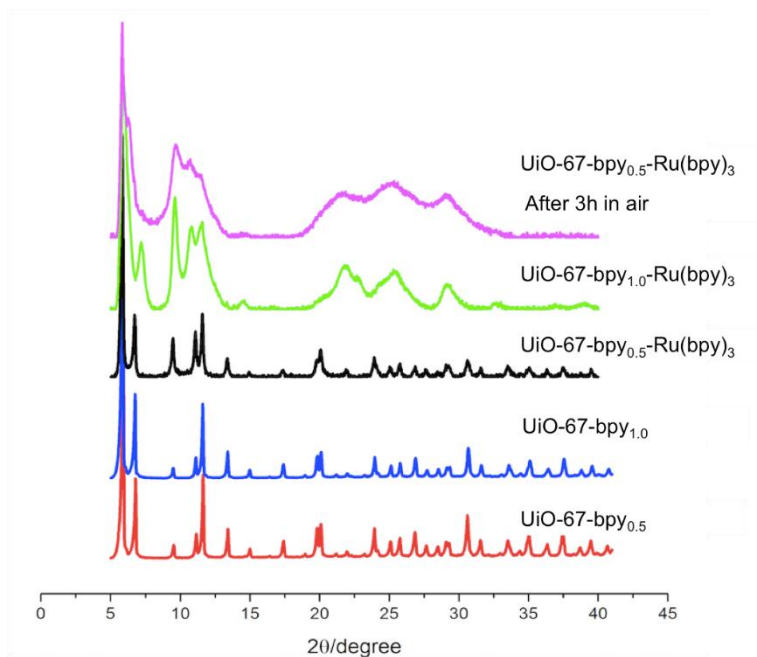


Figure 2-4 PXRD of UiO-67-bpy_{0.5}, UiO-67-bpy_{1.0}, and their metalated derivatives (PSM for 1 h).

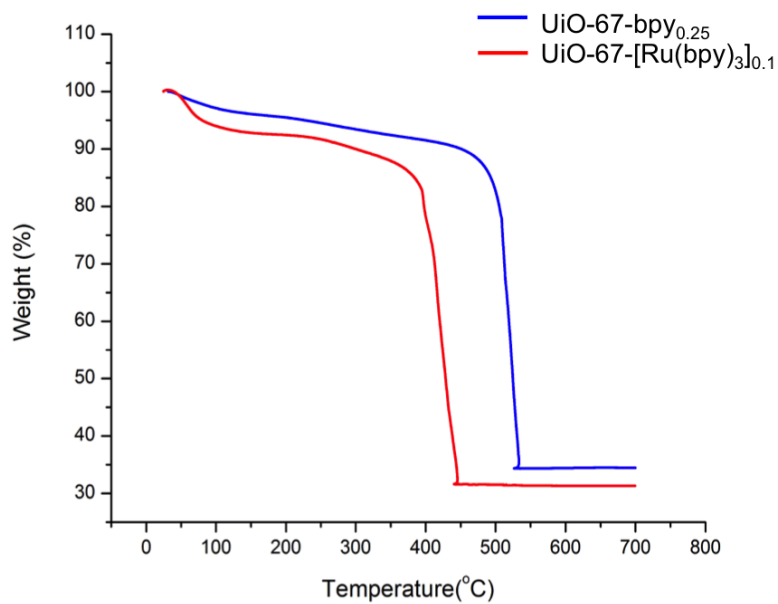


Figure 2-5 TGA of UiO-67-bpy_{0.25} (blue) and UiO-bpy-[Ru(bpy)₃]_{0.1} (red).

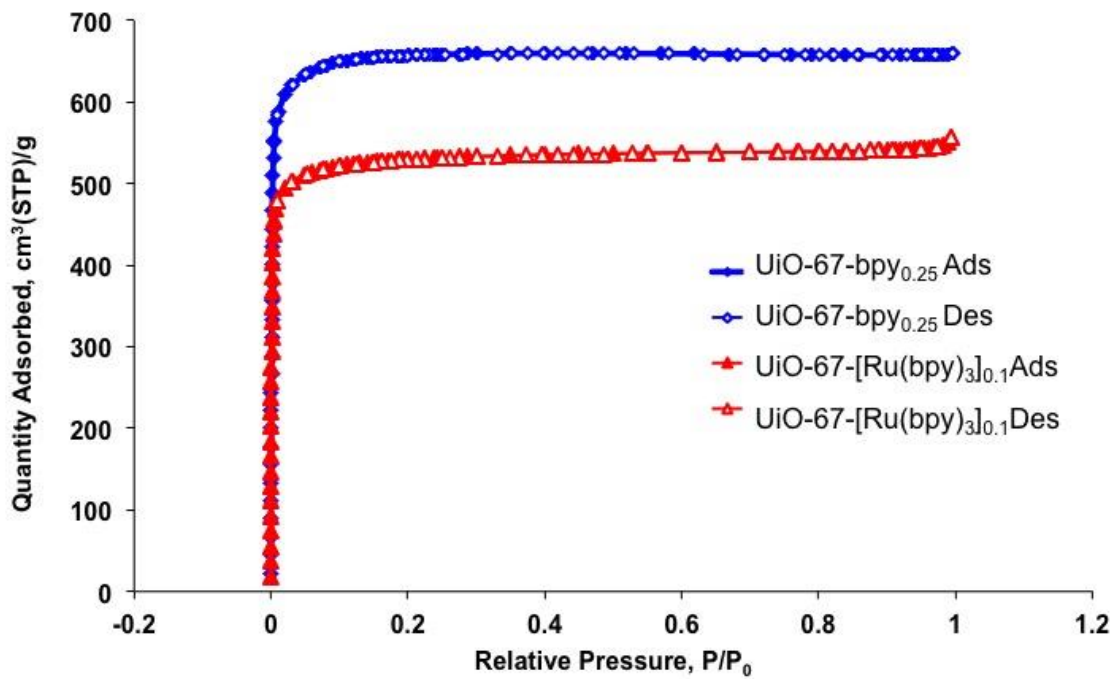


Figure 2-6 N₂ isotherms of UiO-67-bpy_{0.25} and UiO-67-[Ru(bpy)₃].

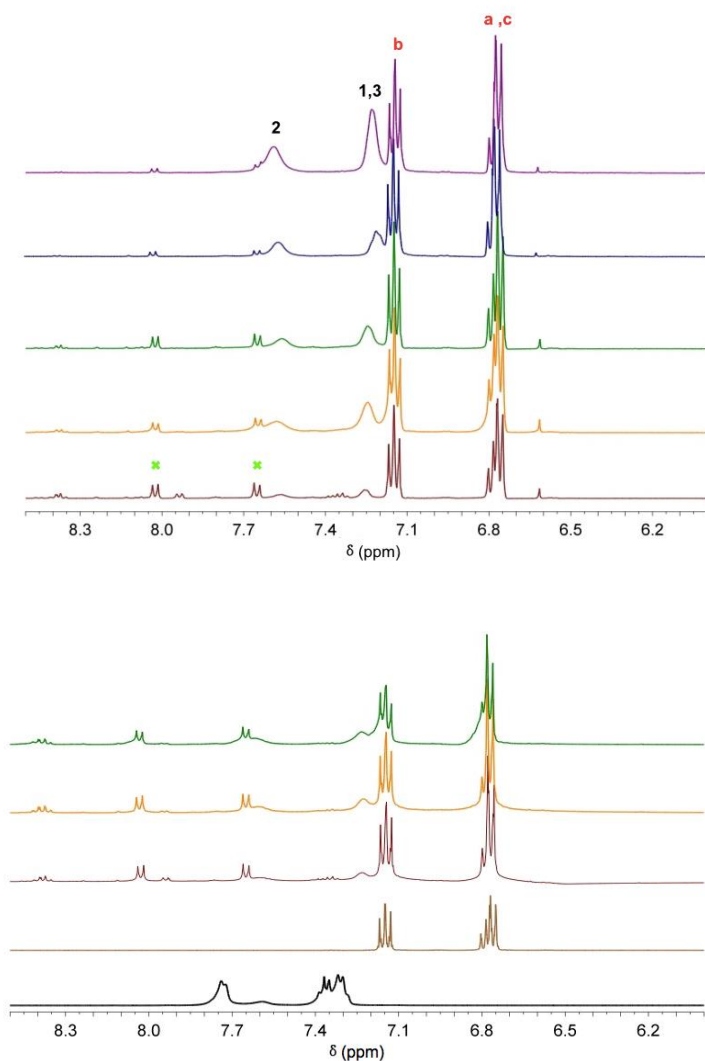
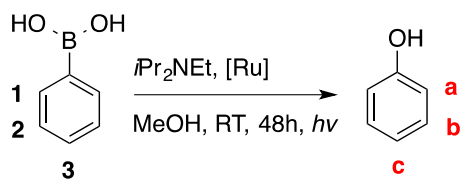


Figure 2-7 ^1H NMR of oxidation of phenylboronic acid. Top: ^1H NMR of 5 cycles of aerobic oxidation of phenylboronic acid using $\text{UiO-67-}[\text{Ru}(\text{bpy})_3]_{0.1}$ as catalyst under near-UV irradiation (peaks for substrate and product are labeled): Run 1 (dark red, yield 81%); Run 2 (orange, yield 72%); Run 3 (green, yield 74%); Run 4 (blue, yield 73%); and Run 5 (dark magenta, yield 57%). Bottom: ^1H NMR of phenyl boronic acid (black), phenol (brown) and 3 cycles of aerobic oxidation of phenylboronic acid using $\text{UiO-67-}[\text{Ru}(\text{bpy})_3]_{0.1}$ as catalyst under visible-light irradiation: Run 1 (dark red, yield 85%); Run 2 (orange, yield 78%); Run 3 (green, yield 78%). Some dcbp^{2-} ligand (\times) is observed in the reaction mixture after photocatalysis (see Figure 2-11).

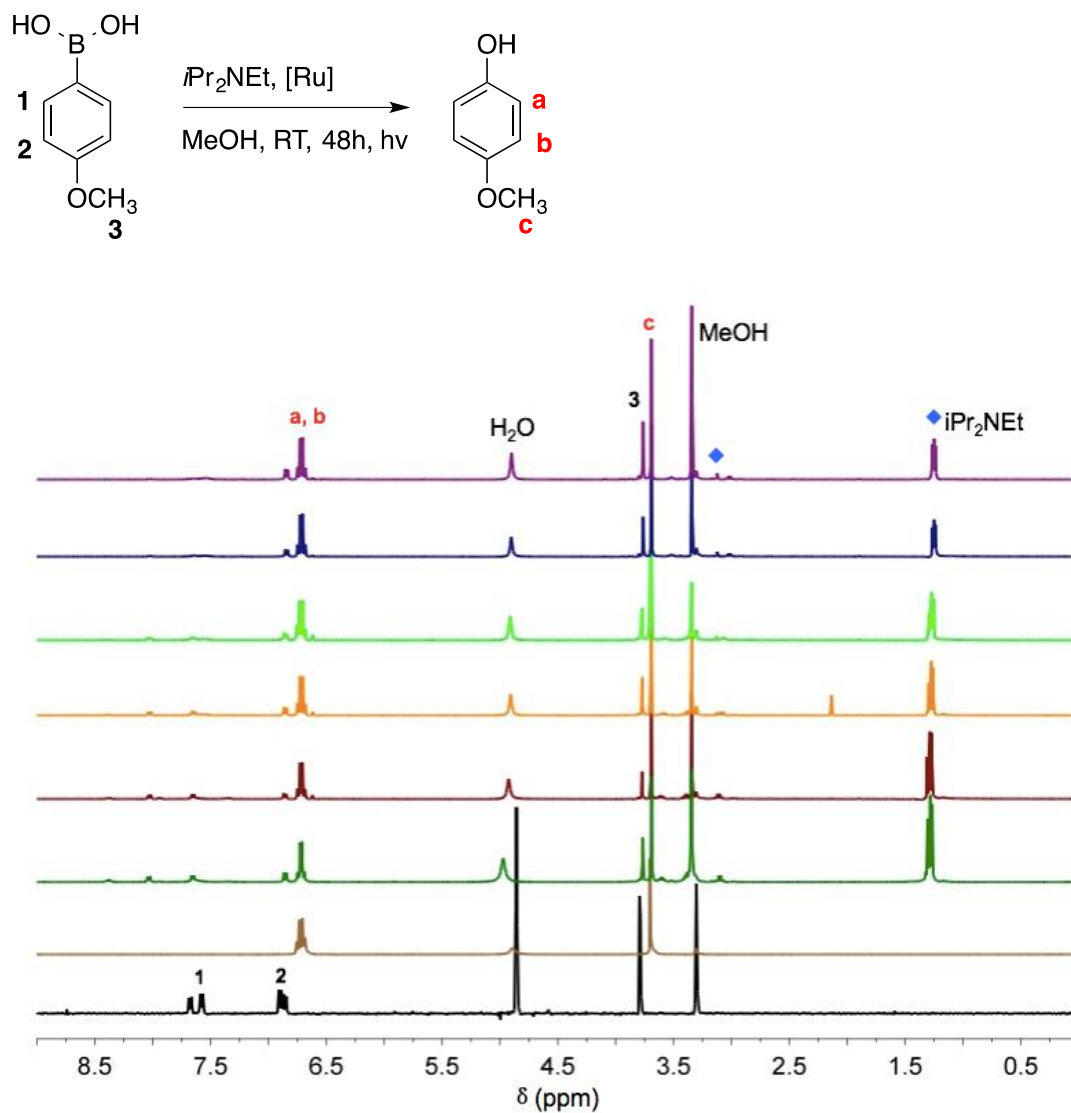


Figure 2-8 $^1\text{H NMR}$ of 4-methoxyphenylboronic acid (black), 4-methoxyphenol (brown), aerobic oxidation of 4-methoxyphenylboronic acid using $\text{UiO-67-}[\text{Ru}(\text{bpy})_3]_{0.1}$ as catalyst under visible-light irradiation (dark green, Yield 72%) and 5 cycles under near-UV irradiation: Run 1 (dark red, Yield 76%), Run 2 (orange, Yield 72%), Run 3 (green, Yield 72%), Run 4 (dark blue, Yield 73%) and Run 5 (dark magenta, Yield 66%).

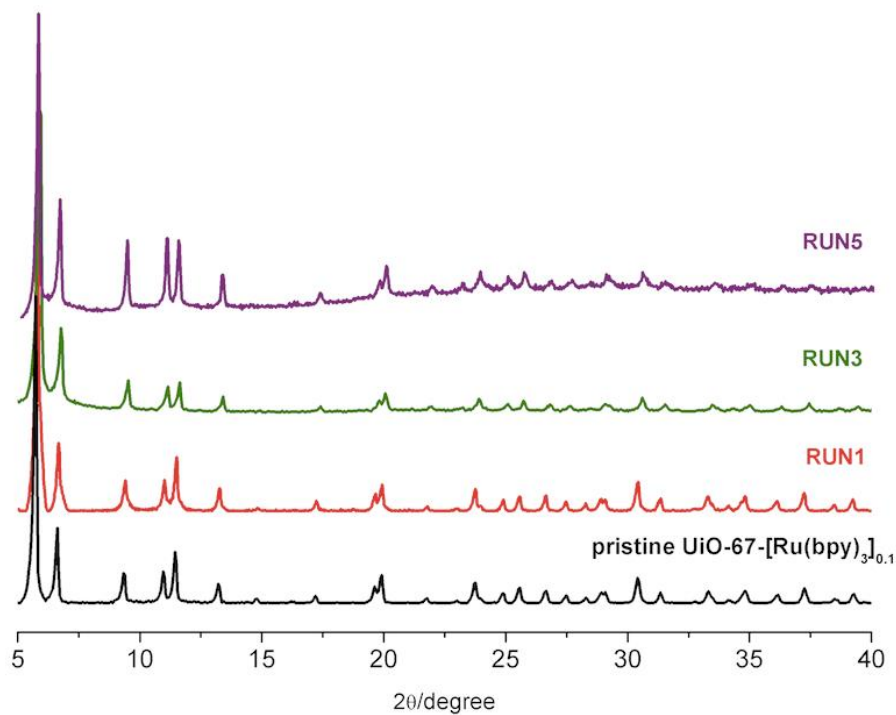


Figure 2-9 PXRD of 5 cycles of UiO-67-[Ru(bpy)₃]_{0.1} catalyst.

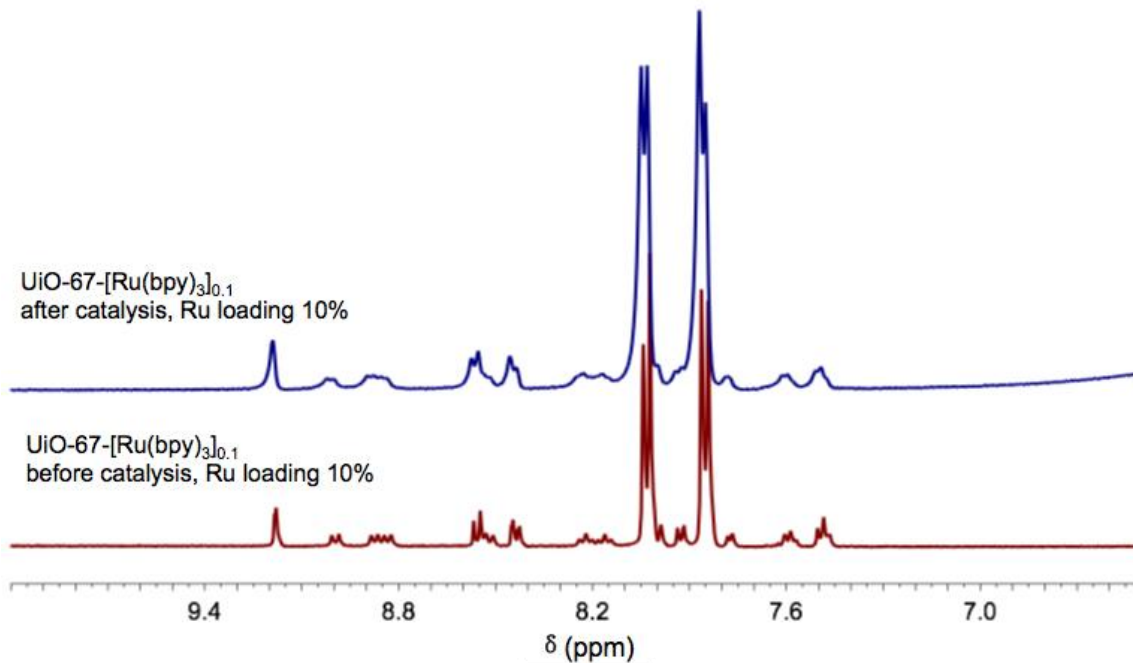


Figure 2-10 ¹H NMR of digested UiO-67-[Ru(bpy)₃]_{0.1} before (red) and after (blue) catalysis showing minimal or no loss in Ru(bpy)₃ from the MOF.

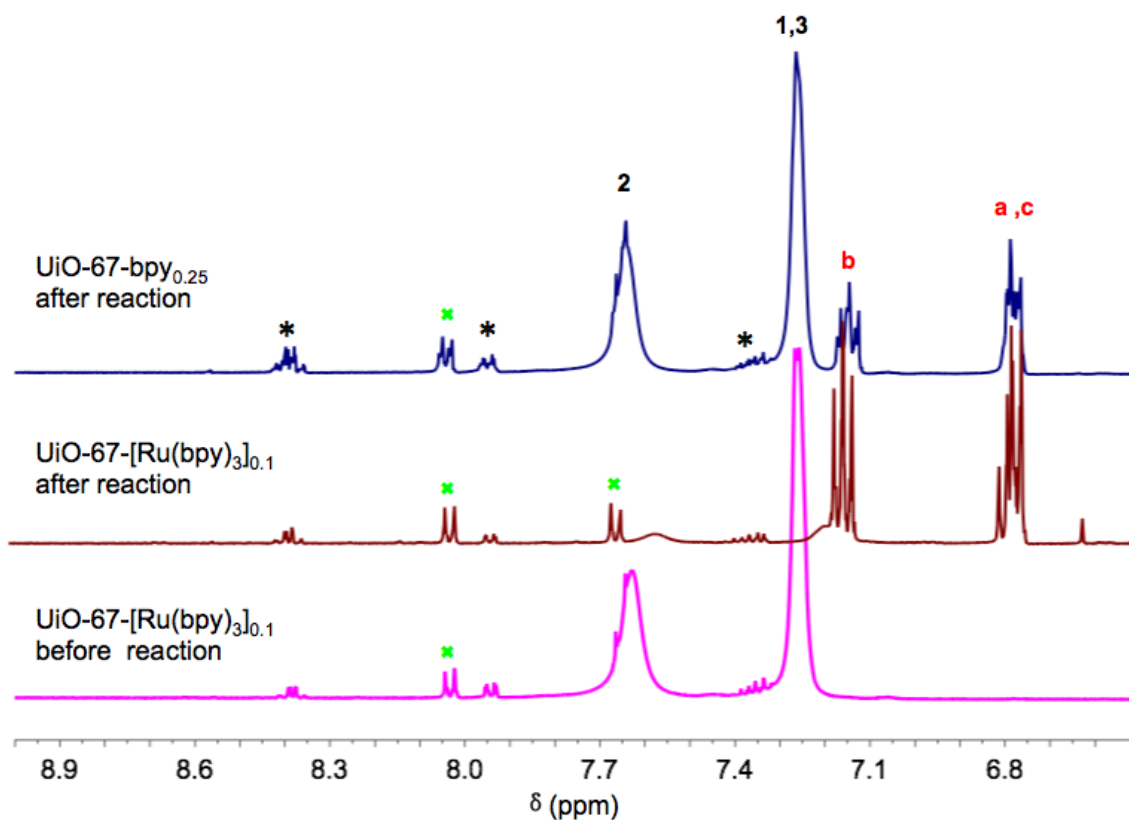
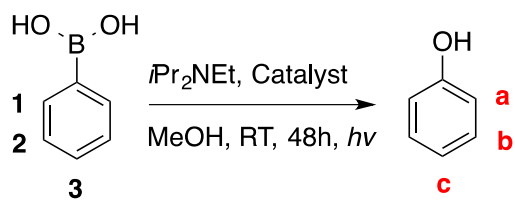


Figure 2-11 ^1H NMR of oxidation of phenylboronic acid using UiO-67- $[\text{Ru}(\text{bpy})_3]_{0.1}$ as catalyst (before reaction, magenta; after reaction, dark red) and UiO-67- $\text{bpy}_{0.25}$ as catalyst (after reaction, dark blue). Both reaction mixtures show some degree of dcbp^{2-} ligand (\times) before and after photocatalysis. The dcbp^{2-} ligand may be leaching from within the MOF (incomplete washing, trapped in pores) or from the MOF itself (partial degradation). Peaks denoted with asterisks represent a small amount of unidentified impurities.

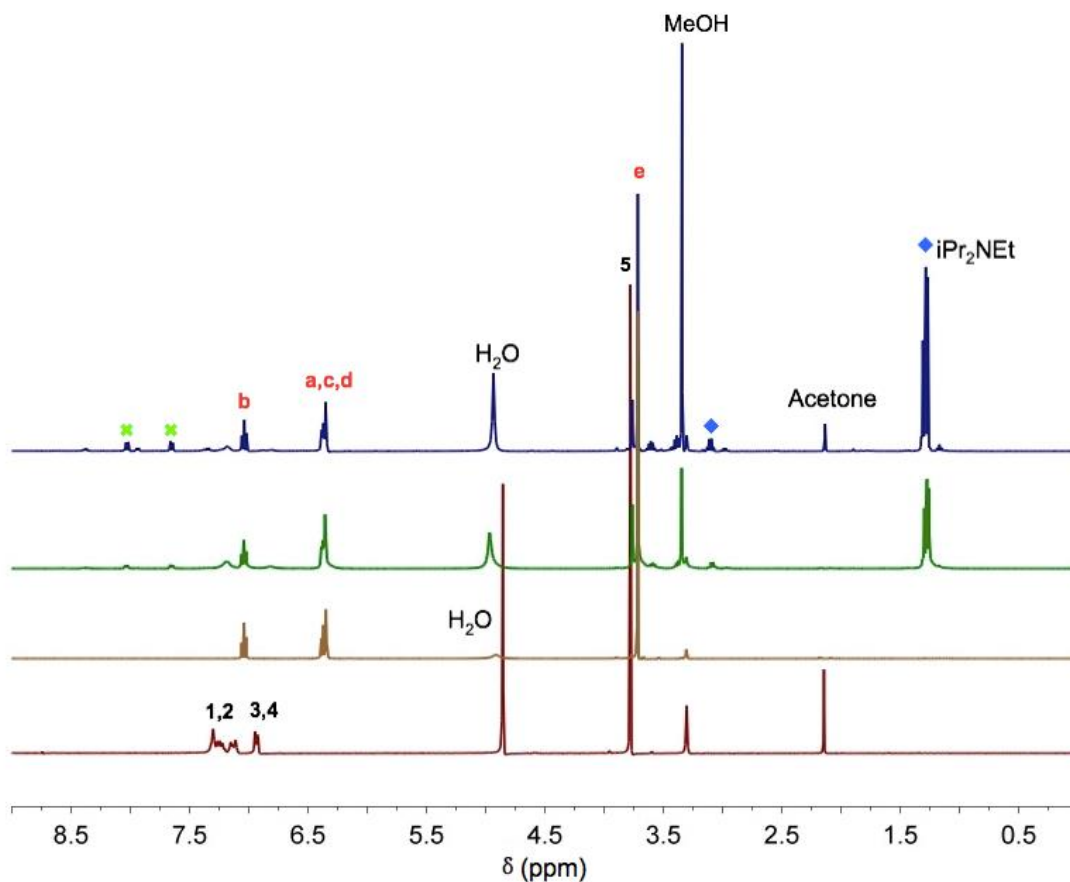
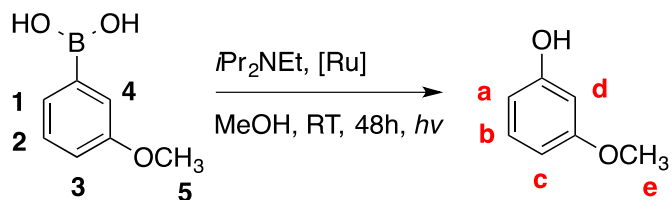


Figure 2-12 $^1\text{H NMR}$ of 3-methoxyphenylboronic acid (dark red), 3-methoxyphenol (brown), reaction mixture after photocatalysis under visible-light irradiation (dark green, Yield ~72%) and near UV light irradiation (dark blue, Yield ~79%). Some dcbp²⁻ ligand (*) is observed in the reaction mixture after photocatalysis (see Figure 2-11).

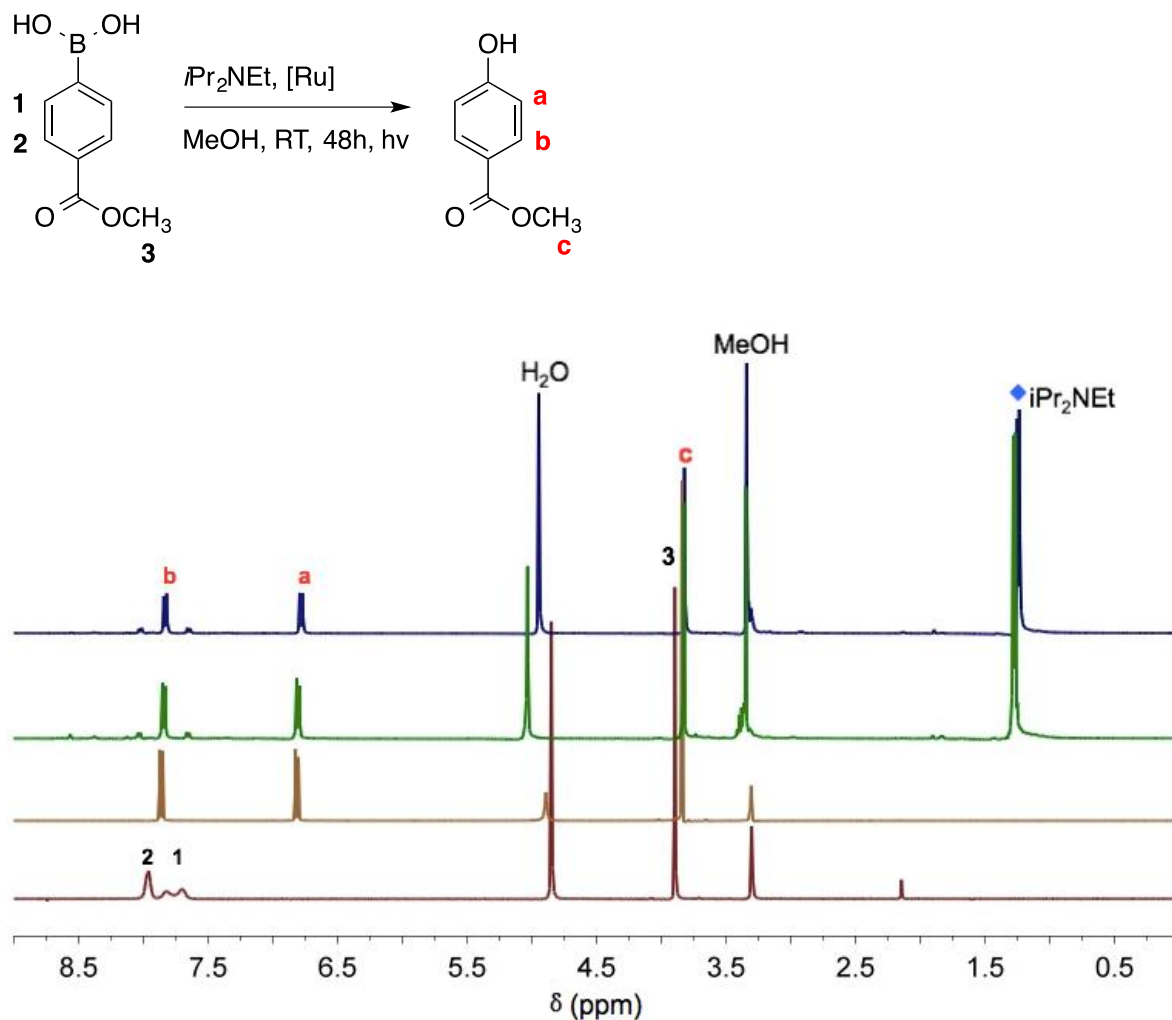


Figure 2-13 $^1\text{H NMR}$ of 4-(methoxycarbonyl)phenylboronic acid (dark red), methyl 4-hydroxybenzoate (brown) and reaction mixture after photocatalysis under both visible light (dark green, Yield > 95%) and near-UV irradiation (dark blue, Yield > 95%).

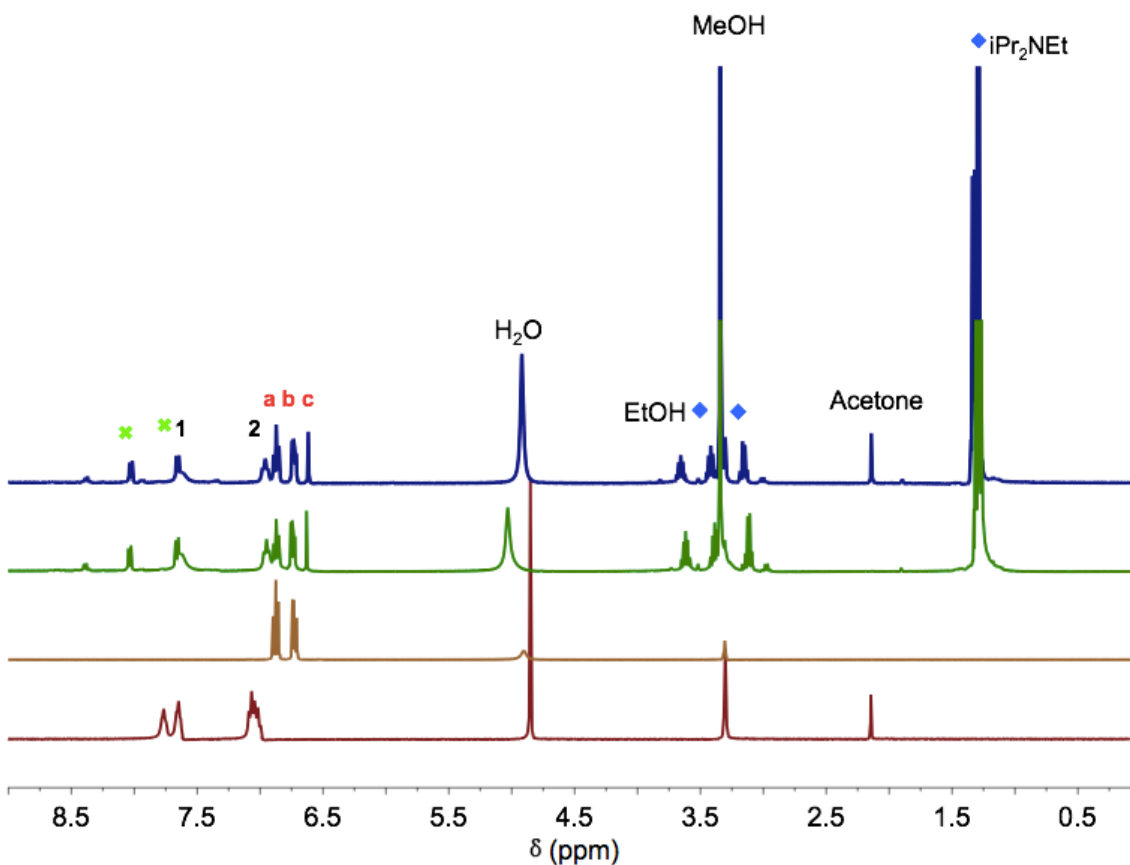
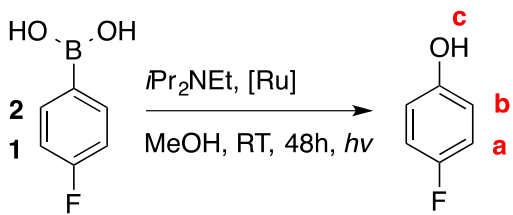


Figure 2-14 ^1H NMR of 4-fluorophenylboronic acid (dark red), 4-fluorophenol (brown), reaction mixture after photocatalysis under both visible-light irradiation (dark green, Yield ~50%) and near-UV irradiation (dark blue, Yield ~55%). Some dcbp²⁻ ligand (✖) is observed in the reaction mixture after photocatalysis (see Figure 2-11).

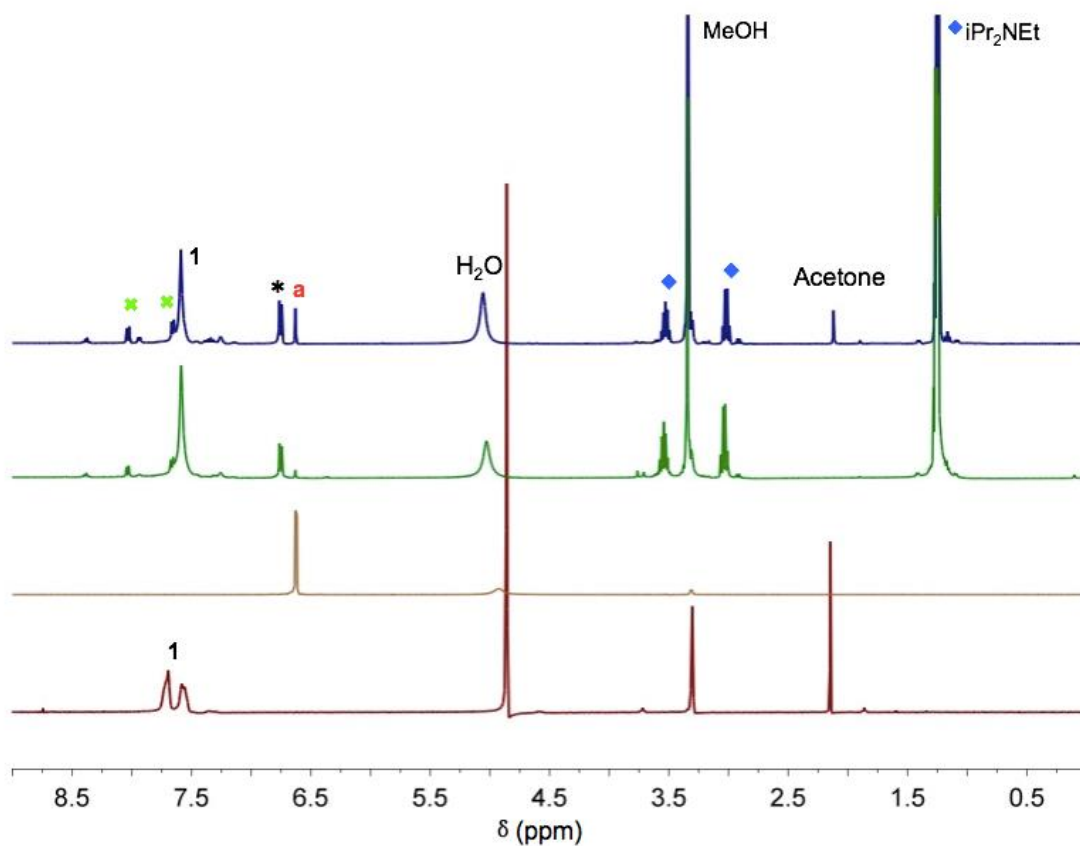
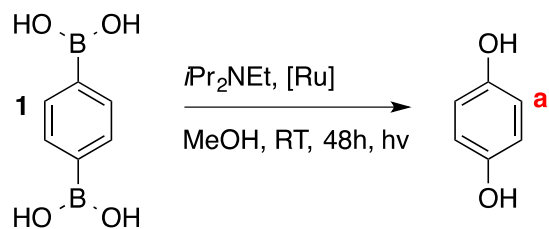


Figure 2-15 $^1\text{H NMR}$ of 1,4-phenylenediboronic acid (dark red), hydroquinone (brown), mixture after reaction under visible-light irradiation (dark green, Yield 15%) and near-UV irradiation (dark blue, Yield 23%). Peaks denoted with asterisks came from benzoquinone, oxidation product of hydroquinone. dcbp^{2-} ligand (x) is observed in the reaction mixture after photocatalysis (see Figure 2-11).

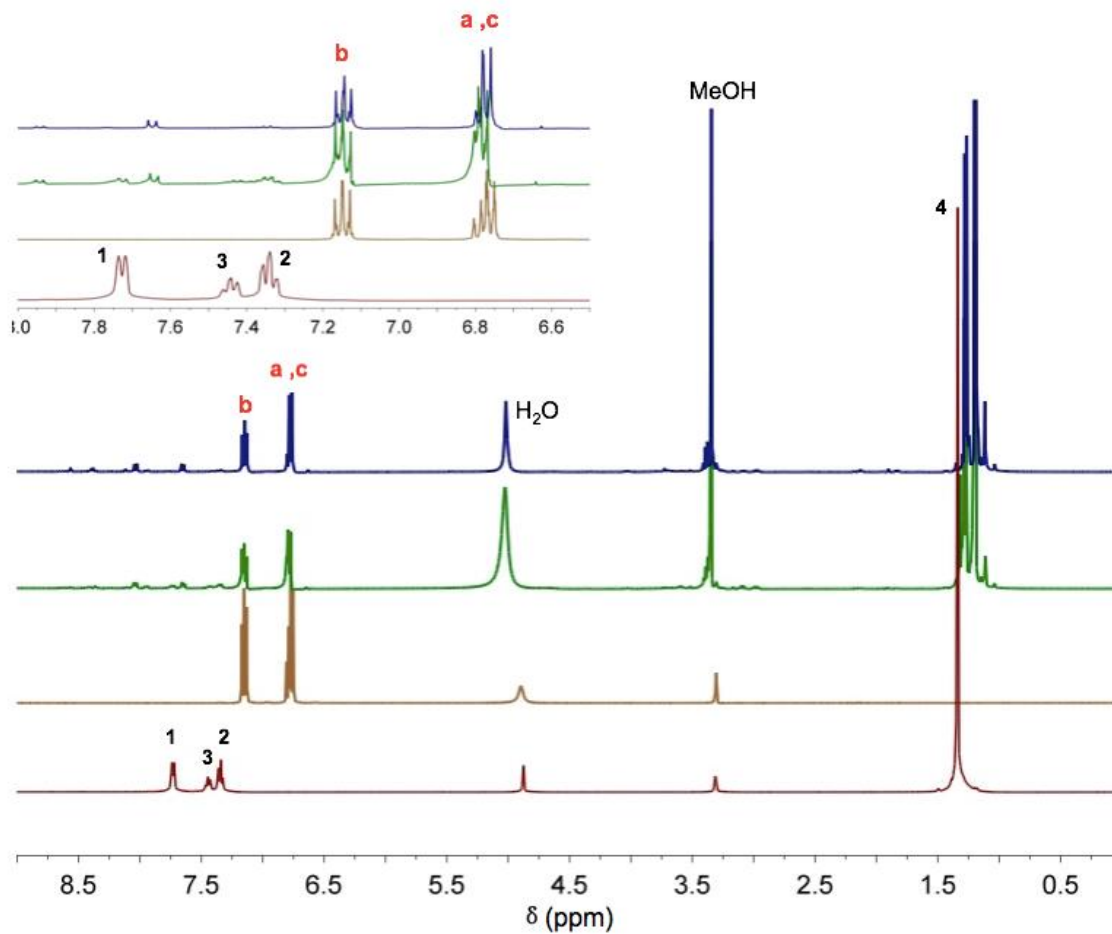
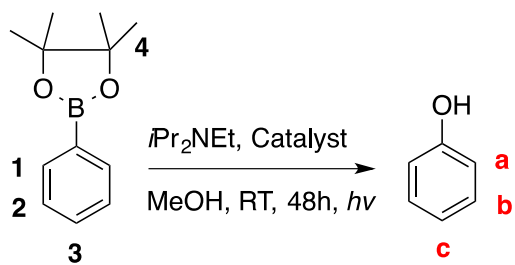


Figure 2-16 $^1\text{H NMR}$ of phenylboronic acid pinacol ester (dark red), phenol (brown) and reaction mixture after photocatalysis under both visible-light (dark green, Yield 91%) and near-UV irradiation (dark blue, Yield > 95%).

2.7 Acknowledgments

Text, tables, and figures in this chapter are, in large part, reprints of materials published in the following paper: Xiao Yu and Seth M. Cohen*, "Photocatalytic Metal-organic Frameworks for the Aerobic Oxidation of Arylboronic Acids" *Chem. Commun.* **2015**, *51*, 9880-9883. The dissertation author was the primary researcher for the data presented and was the primary author of this publication. The permissions to reproduce this material were granted by the Royal Society of Chemistry, copyright 2015.

2.8 References

1. Zhang, T.; Lin, W., Metal-organic frameworks for artificial photosynthesis and photocatalysis. *Chem Soc Rev* **2014**, *43* (16), 5982-93.
2. P. Mahata; G. Madras; S. Natarajan, Novel Photocatalysts for the Decomposition of Organic Dyes Based on Metal-Organic Framework Compounds. *J. Phys. Chem. B.* **2006**, *110* (28), 13759-13768.
3. Fateeva, A.; Chater, P. A.; Ireland, C. P.; Tahir, A. A.; Khimyak, Y. Z.; Wiper, P. V.; Darwent, J. R.; Rosseinsky, M. J., A water-stable porphyrin-based metal-organic framework active for visible-light photocatalysis. *Angew. Chem. Int. Ed.* **2012**, *51* (30), 7440-4.
4. D. Sun; Y. Gao; J. Fu; X. Zeng; Chen, Z.; Li, Z., Construction of a supported Ru complex on bifunctional MOF-253 for photocatalytic CO₂ reduction under visible light. *Chem. Commun.* **2015**, *51* (13), 2645-2648.
5. Horiuchi, Y.; Toyao, T.; Saito, M.; Mochizuki, K.; Iwata, M.; Higashimura, H.; Anpo, M.; Matsuoka, M., Visible-Light-Promoted Photocatalytic Hydrogen Production by Using an Amino-Functionalized Ti(IV) Metal-Organic Framework. *J. Phys. Chem. C.* **2012**, *116* (39), 20848-20853.
6. Long, J.; Wang, S.; Ding, Z.; Wang, S.; Zhou, Y.; Huang, L.; Wang, X., Amine-functionalized zirconium metal-organic framework as efficient visible-light photocatalyst for aerobic organic transformations. *Chem Commun.* **2012**, *48* (95), 11656-8.
7. D. Sun; Y. Fu; W. Liu; L. Ye; D. Wang; L. Yang; X. Fu; Li, Z., Studies on Photocatalytic CO₂ Reduction over NH₂-Uio-66(Zr) and Its Derivatives: Towards a Better

Understanding of Photocatalysis on Metal–Organic Frameworks. *Chem. Eur. J.* **2013**, *19* (42), 14279-14285.

8. D. Wang; R. Huang; W. Liu; D. Sun; Li, Z., Fe-Based MOFs for Photocatalytic CO₂ Reduction: Role of Coordination Unsaturated Sites and Dual Excitation Pathways. *ACS Catal.* **2014**, *4* (12), 4254-4260.

9. Y. Fu; D. Sun; Y. Chen; R. Huang; Z. Ding; X. Fu; Li, Z., An Amine-Functionalized Titanium Metal–Organic Framework Photocatalyst with Visible-Light-Induced Activity for CO₂ Reduction. *Angew. Chem. Int. Ed.* **2012**, *51* (14), 3364-3367.

10. Dhakshinamoorthy, A.; Alvaro, M.; Garcia, H., Aerobic Oxidation of Benzylic Alcohols Catalyzed by Metal–Organic Frameworks Assisted by TEMPO. *ACS Catal.* **2011**, *1* (1), 48-53.

11. Wu, P.; He, C.; Wang, J.; Peng, X.; Li, X.; An, Y.; Duan, C., Photoactive chiral metal-organic frameworks for light-driven asymmetric alpha-alkylation of aldehydes. *J. Am. Chem. Soc.* **2012**, *134* (36), 14991-9.

12. Prier, C. K.; Rankic, D. A.; MacMillan, D. W., Visible light photoredox catalysis with transition metal complexes: applications in organic synthesis. *Chem. Rev.* **2013**, *113* (7), 5322-63.

13. M. A. Ischay; M. E. Anzovino; J. Du; Yoon, T. P., Efficient visible light photocatalysis of [2+ 2] enone cycloadditions. *J. Am. Chem. Soc.* **2008**, *130* (39), 12886-12887.

14. Nicewicz, D. A.; MacMillan, D. W. C., Merging photoredox catalysis with organocatalysis: The direct asymmetric alkylation of aldehydes. *Science* **2008**, *322* (5898), 77-80.

15. J. M. R. Narayanam; J. W. Tucker; C. R. J. Stephenson, Electron-Transfer Photoredox Catalysis: Development of a Tin-Free Reductive Dehalogenation Reaction. *J. Am. Chem. Soc.* **2009**, *131* (25), 8756-8757.

16. A. G. Condie; C. Gonza; Stephenson, C. R. J., Visible-Light Photoredox Catalysis: Aza-Henry Reactions via C-H Functionalization. *J. Am. Chem. Soc.* **2010**, *132* (5), 1464-1465.

17. Rueping, M.; Vila, C.; Szadkowska, A.; Koenigs, R. M.; Fronert, J., Photoredox Catalysis as an Efficient Tool for the Aerobic Oxidation of Amines and Alcohols: Bioinspired Demethylations and Condensations. *ACS Catal.* **2012**, *2* (12), 2810-2815.

18. Zou, Y. Q.; Chen, J. R.; Liu, X. P.; Lu, L. Q.; Davis, R. L.; Jorgensen, K. A.; Xiao, W. J., Highly efficient aerobic oxidative hydroxylation of arylboronic acids: photoredox catalysis using visible light. *Angew. Chem. Int. Ed.* **2012**, *51* (3), 784-8.
19. J. Zen; S. Liou; A. Kumar; M. Hsia, An Efficient and Selective Photocatalytic System for the Oxidation of Sulfides to Sulfoxide. *Angew. Chem. Int. Ed.* **2003**, *115* (5), 597-599.
20. Tucker, J. W.; Nguyen, J. D.; Narayanam, J. M.; Krabbe, S. W.; Stephenson, C. R., Tin-free radical cyclization reactions initiated by visible light photoredox catalysis. *Chem. Commun.* **2010**, *46* (27), 4985-7.
21. Wang, C.; Xie, Z.; deKrafft, K. E.; Lin, W., Doping metal-organic frameworks for water oxidation, carbon dioxide reduction, and organic photocatalysis. *J. Am. Chem. Soc.* **2011**, *133* (34), 13445-54.
22. Song, J.; Luo, Z.; Britt, D. K.; Furukawa, H.; Yaghi, O. M.; Hardcastle, K. I.; Hill, C. L., A multiunit catalyst with synergistic stability and reactivity: a polyoxometalate-metal organic framework for aerobic decontamination. *J. Am. Chem. Soc.* **2011**, *133* (42), 16839-46.
23. H. Liu; Y. Liu; Y. Li; Z. Tang; Jiang, H., Metal-Organic Framework Supported Gold Nanoparticles as a Highly Active Heterogeneous Catalyst for Aerobic Oxidation of Alcohols. *J. Phys. Chem. C.* **2010**, *114* (31), 13362-13369.
24. Deria, P.; Mondloch, J. E.; Karagiari, O.; Bury, W.; Hupp, J. T.; Farha, O. K., Beyond post-synthesis modification: evolution of metal-organic frameworks via building block replacement. *Chem. Soc. Rev.* **2014**, *43* (16), 5896-912.
25. Fei, H.; Cohen, S. M., A robust, catalytic metal-organic framework with open 2,2'-bipyridine sites. *Chem. Commun.* **2014**, *50* (37), 4810-2.
26. Rappoport, Z., *The Chemistry of Phenols*. Wiley-VCH: Weinheim, Germany, 2003; p. 1694.
27. Huang, J.-M.; Chen, D.-S., A Mild and Highly Efficient Conversion of Arylboronic Acids into Phenols by Oxidation with MCPBA. *Synlett* **2013**, *24* (04), 499-501.
28. Mulakayala, N.; Ismail; Kumar, K. M.; Rapolu, R. K.; Kandagatla, B.; Rao, P.; Oruganti, S.; Pal, M., Catalysis by Amberlite IR-120 resin: a rapid and green method for the synthesis of phenols from arylboronic acids under metal, ligand, and base-free conditions. *Tetrahedron Lett.* **2012**, *53* (45), 6004-6007.

29. Bora, U.; Gogoi, A., An Iodine-Promoted, Mild and Efficient Method for the Synthesis of Phenols from Arylboronic Acids. *Synlett* **2012**, 23 (07), 1079-1081.
30. Prakash, G. K. S.; Chacko, S.; Panja, C.; Thomas, T. E.; Gurung, L.; Rasul, G.; Mathew, T.; Olah, G. A., Regioselective Synthesis of Phenols and Halophenols from Arylboronic Acids Using Solid Poly(N-vinylpyrrolidone)/ Hydrogen Peroxide and Poly(4-vinylpyridine)/Hydrogen Peroxide Complexes. *Adv. Synth. Catal.* **2009**, 351 (10), 1567-1574.
31. Inamoto, K.; Nozawa, K.; Yonemoto, M.; Kondo, Y., Micellar system in copper-catalysed hydroxylation of arylboronic acids: facile access to phenols. *Chem. Commun.* **2011**, 47 (42), 11775-7.
32. Kaboudin, B.; Abedi, Y.; Yokomatsu, T., CuII- β -Cyclodextrin Complex as a Nanocatalyst for the Homo- and Cross-Coupling of Arylboronic Acids under Ligand- and Base-Free Conditions in Air: Chemoselective Cross-Coupling of Arylboronic Acids in Water. *Eur. J. Org. Chem.* **2011**, 2011 (33), 6656-6662.
33. Chowdhury, A. D.; Mobin, S. M.; Mukherjee, S.; Bhaduri, S.; Lahiri, G. K., [Pd(L)Cl₂]-Catalyzed Selective Hydroxylation of Arylboronic Acids to Phenols. *Eur. J. Inorg. Chem.* **2011**, 2011 (21), 3232-3239.
34. S. P. Pitre; C. D. McTiernan; H. Ismaili; Scaiano, J. C., Mechanistic Insights and Kinetic Analysis for the Oxidative Hydroxylation of Arylboronic Acids by Visible Light Photoredox Catalysis: A Metal-Free Alternative. *J. Am. Chem. Soc.* **2013**, 135 (36), 13286-13289.
35. S. Botta; J. Navío; M. Hidalgo; G. M. Restrepo; M. I. Litter, Photocatalytic properties of ZrO₂ and Fe/ZrO₂ semiconductors prepared by a sol-gel technique. *J. Photochem. Photobiol. A Chem.* **1999**, 129 (1-2), 89-99.

**Chapter 3 : Photocatalytic Metal-organic Frameworks for Selective 2,2,2-
Trifluoroethylation of Styrenes**

3.1 Introduction

The development of synthetic methods for CF₃-containing compounds has gained increasing attention because of the growing demand in the pharmaceutical and agrochemical industries.¹⁻³ Fluorinated organic compounds can display enhanced lipophilicity, membrane permeability, elevated electronegativity, and resistance to oxidation, making many such compounds promising drug candidates.⁴ As a consequence, substantial efforts have been devoted to the incorporation of -CF₃ groups into various organic structures,⁵⁻⁹ including via direct 2,2,2-trifluoroethylation through CF₃CH₂· radical processes.¹⁰⁻¹²

MOFs are readily functionalized providing versatile platforms for including catalytic sites.¹³⁻¹⁴ The abundant choice of structures imposes size- and shape-selective restrictions through well-defined channels and pores. For example, Long et al. has demonstrated size-selectivity in a Mn-based MOF catalyst for the cyanosilylation of aromatic aldehydes and the Mukaiyama-aldol reaction, because the pores of the MOF are too small to accommodate large substrates.¹⁵ The Li group showed that MOFs can be used in a ‘ship-in-a-bottle’ synthesis to afford selective photochemical products from a cage effect.¹⁶ Regio- and enantioselective reactions can be realized by incorporating stereoselective catalysts into MOFs or confining chiral substrates within the micropores of solid materials.¹⁷⁻²⁰ In one important example, Lin et al. was able to synthesize homochiral MOFs with privileged chiral ligand BINOL (1,1'-bi-2-naphthol), which was used as a heterogeneous asymmetric catalyst upon metalation with Ti, showing complete conversion and high ee for diethylzinc addition to aldehydes.²¹ Other chiral ligands, like BINAP, chiral salens, and L-proline have also been proven to be useful asymmetric catalysts in MOFs for catalyzing other asymmetric reactions.²²⁻²⁴ In many cases, the MOF-

based catalysts show better performance and easier separation/recovery when compared to homogeneous systems.

The ability of Ir(III) polypyridyl complexes, like Ir(ppy)₃, to function as visible light photocatalysts have been recognized and extensively investigated to synthesize fine chemicals.²⁵⁻²⁶ Considering the high cost of these precious metal photoredox catalysts, using MOFs as heterogeneous and easily reusable systems could be of substantial value.²⁷⁻²⁹ Postsynthetic approaches have proven to be useful for preparing single-site catalysts within MOFs.³⁰ In chapter 2, incorporation of catalytic active sites into the Zr(IV)-based UiO-series MOFs has proven to be attractive because of the outstanding chemical stability and robust crystallinity of these materials.³¹⁻³² However, the photocatalytic MOF in chapter 2 was used for simple oxidation reactions, and it did not show improved catalytic properties comparing to its homogeneous counterpart.

Herein, we incorporated [Ir^{III}(ppy)₂(dcbpy)]Cl (bis(4-phenyl-2-pyridine)(5,5'-dicarboxyl-2,2'-bipyridine)iridium(III) chloride) and [Ir^{III}(ppy^F)₂(dcbpy)]Cl (bis(2-(2,4-difluorophenyl)-5-(trifluoromethyl)pyridine)(5,5'-dicarboxyl-2,2'-bipyridine)iridium(III) chloride) into the UiO-67 framework via postsynthetic modification (PSM). The resulting MOFs exhibit efficient photocatalytic ability and high selectivity for 2,2,2-trifluoroethylation of styrenes under visible-light irradiation at ambient atmosphere. Notably, the UiO-67-Ir(L)₂ catalysts were observed to show selectivity for the reaction products that were reversed when compared to homogenous Ir(III) analogs. The solid-state catalyst exhibited a 'MOF effect',¹⁷ apparently confining intermediate radicals within the pores and suppressing the formation of an undesirable dimerization side product. This is distinct from conventional size-selectivity observed with MOFs that simply excludes large substrates from diffusing and reacting inside

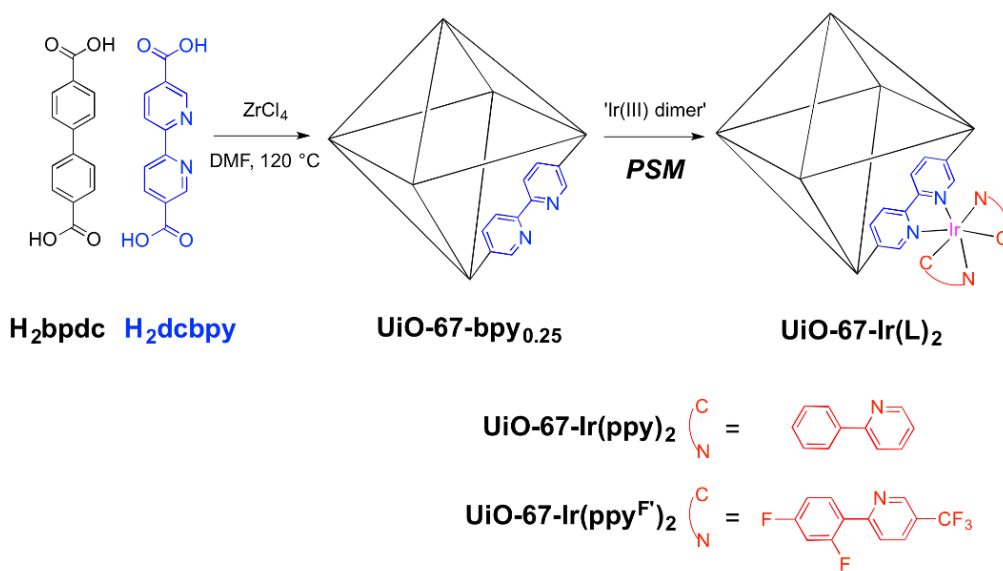
the MOF micropores. To the best of our knowledge, this is the first time the use of a MOF-based catalyst has been shown to dramatically change the reaction trajectory to give a more desirable product outcome/distribution when compared to the analogous homogenous system.

3.2 MOF Synthesis and Characterization

The parent UiO-67-bpy_{0.25} framework was prepared using solvothermal conditions containing a mixture of ZrCl₄, H₂bpdca (biphenyldicarboxylic acid)/H₂dc bpy (2,2'-bipyridine-dicarboxylic acid) ligands, and benzoic acid (as a modulator) at 120 °C in DMF for 24 h (Figure 3-1). Two Ir(III) dimers, [Ir(ppy)₂Cl]₂ and [Ir(ppy^F)₂Cl]₂, were synthesized by combining IrCl₃•H₂O with the corresponding phenylpyridine ligands in 2-ethoxyethanol/H₂O at 100 °C for 24h. Framework metalation (PSM) of UiO-67-bpy_{0.25} using these dimeric precursors was monitored by ¹H NMR. This was achieved after digestion of the MOFs in D₃PO₄/*d*⁶-DMSO, where the kinetically inert Ir(III) complexes remained intact even under these dissolution conditions. Integration of the proton resonances for the Ir(III) complexes and the free dc bpy²⁻ ligands confirmed the degree of PSM, which is tunable by varying the modification time. For example, UiO-67-bpy_{0.25} was combined with 0.3 equivalent of [Ir(ppy)₂Cl]₂ in CH₂Cl₂/MeOH at 55 °C for 24 h to produce the desired UiO-67-Ir(ppy)₂ with 20% overall Ir(III) loading in UiO-67-bpy_{0.25} (~80% metalation of the bipyridine sites, Figure 3-4). Similarly, PSM with [Ir(ppy^F)₂Cl]₂ for 72 h in CH₂Cl₂/MeOH at 55 °C afforded UiO-67-Ir(ppy^F)₂ with 9% overall Ir(III) loading (~36% metalation of the bipyridine sites, Figure 3-4). ICP-MS analysis was used to further quantify the Ir loading, showing that Ir:Zr ratio is 1:5.3 for UiO-67-Ir(ppy)₃ (after 24 h metalation) and 1:10.8 for UiO-67-Ir(ppy^F)₃ (after 72 h metalation), which is consistent with the aforementioned NMR data. For UiO-67-Ir(ppy)₂, the amount of Ir(III) complex included

can be controlled between 2% to 20% by varying the PSM time from 2 to 24 h. UiO-67-Ir(ppy^{F'})₂ required longer reaction times to produce higher loadings, as even at 24 h PSM only 4% metalation was achieved. Powder X-ray diffraction (PXRD) confirmed the retention of UiO-67 topology after PSM (Figure 3-2). In addition, permanent porosity was observed for all MOFs as evidenced by N₂ adsorption at 77 K (Figure 3-6). Type I isotherms were obtained for both of UiO-67-Ir MOFs with ~2100 m²/g BET surface area for UiO-67-Ir(ppy)₂ and ~2000 m²/g for UiO-67-Ir(ppy^{F'})₂, indicating microporous structures (Table 3-3). With successful incorporation of photocatalytic Ir(III) complexes into a robust MOF, we sought to investigate its photocatalytic ability for trifluoroethylation.

Synthesis of UiO-67-Ir:



Homogeneous Ir catalysts:

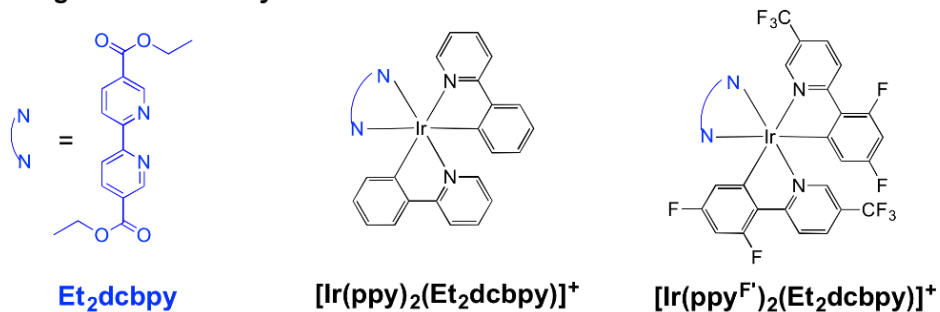


Figure 3-1 Synthesis of UiO-67-Ir via PSM and homogeneous Ir catalysts.

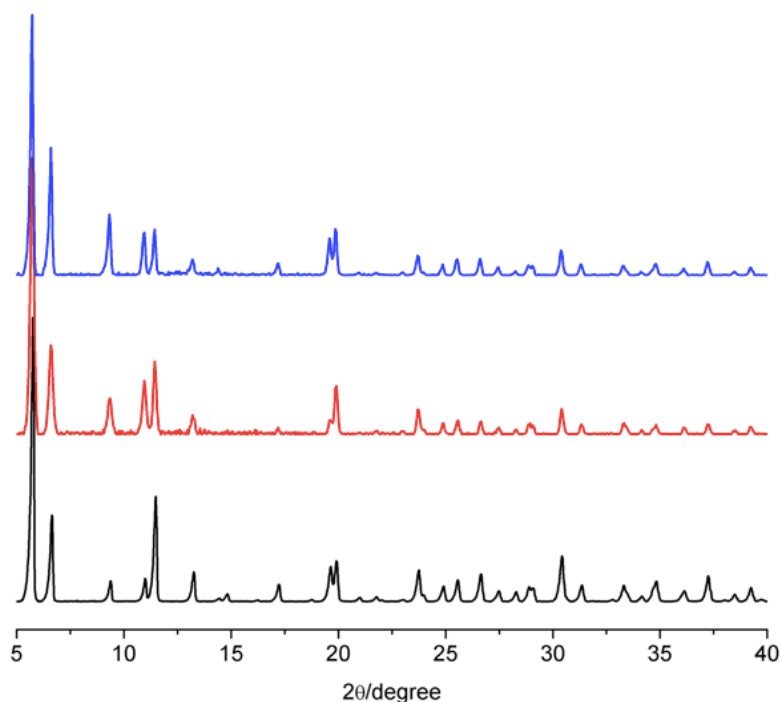


Figure 3-2 PXRD of UiO-67-bpy_{0.25} (black), UiO-67-Ir(ppy)₂ (red) and UiO-67-Ir(ppy^F)₂ (blue).

3.3 Catalytic Reactions

As a benchmark reaction, 4-methoxystyrene was used as a substrate with CF₃CH₂I in acetonitrile/H₂O under visible-light irradiation, with N, N-diisopropylethylamine as a base. These reactions were monitored by use of gas chromatography-mass spectrometry (GC-MS). Using UiO-67-Ir(ppy)₂ (20% loading after PSM, ~5 mol% Ir), quantitative conversion resulted in a 60% yield of the hydroxytrifluoroethyl product **A** (Table 3-1, Entry 4). Encouragingly, UiO-67-Ir(ppy^F)₂ (9% loading after PSM, ~5 mol% Ir) was able to improve the yield of the desired product **A** to 76% (Table 3-1, Entry 5). By comparison, three homogeneous photocatalysts: Ir(ppy)₃, [Ir(ppy)₂(Et₂dc bpy)]Cl, [Ir(ppy^F)₂(Et₂dc bpy)]Cl (Figure 3-1) were employed to catalyze the same reaction but produced a high yield of an undesired dimerization side product **C**, with only 10%, 20%, and 32% yields of the preferred hydroxytrifluoroethyl

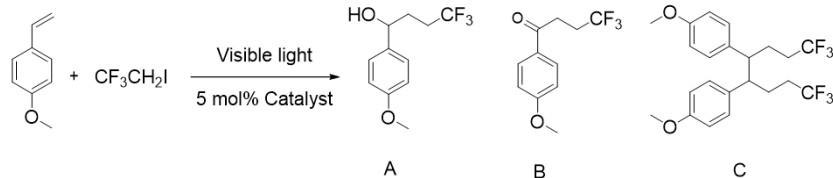
product **A**, respectively (Table 3-1, Entry 1-3). The reversal of selectivity for the hydroxytrifluoroethyl versus dimer product generated from the UiO-67-Ir MOFs, when compared to the homogeneous catalysts, is likely due to the confined space within the MOF pores, which suppresses the dimerization of the benzyl radicals, thereby reducing the yield of product **C** (Figure 3-3). Some over-oxidation to the ketone derivative of product **A** was also found after 48 h of photocatalysis (Table 3-4).³³

In order to gain a better understanding of the catalytic reaction, appropriate control experiments were conducted. First, product **A** cannot be converted to product **C** upon prolonged light irradiation in the presence of these photocatalysts, pointing to confinement as the source of the MOF selectivity. Second, in the absence of a photocatalyst no conversion was observed upon visible-light irradiation (Table 3-1, Entry 6). When the same reaction conditions were employed, but using UiO-67-bpy_{0.25} as catalyst, no products were obtained, indicating that Ir(III) is the catalytic active site (Table 3-1, Entry 7). Furthermore, no product was observed when the reaction was carried out in the absence of light even in the presence of UiO-67-Ir(ppy^{F'})₂, confirming the light-driven nature of the reaction (Table 3-1, Entry 8).

Time-dependent experiments were conducted to compare the catalytic activity of the MOF and homogeneous catalysts, which showed the homogeneous catalyst Ir(ppy)₃ gives a faster conversion, but lower selectivity for product **A** (Figure 3-7). The effect of water content in the reaction, under both an air and oxygen atmosphere, was evaluated. These experiments showed that water can promote hydroxytrifluoroethyl difunctionalization (Figure 3-8) under either atmosphere. With the homogeneous catalyst Ir(ppy)₃, molecular oxygen is used as a radical scavenger to decrease the formation of dimer product. In light of this, photocatalytic reactions performed under an N₂ atmosphere with UiO-67-Ir(ppy^{F'})₂ as a catalyst generated only

trace amount of dimer **C** (conversion and yield <1%) and no other products were formed. This is in stark contrast to the homogeneous catalyst Ir(ppy)₃, which produces ~60% of dimer **C** under the same conditions. These results further confirm our proposed mechanism (Figure 3-3) where the selectivity for the reaction with the MOF catalysts originates from site isolation within the MOF structure, and not solely from differences in the rates of reaction as a function of oxygen or air.

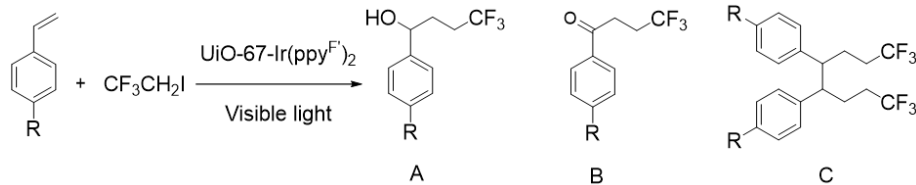
To test the heterogeneity of UiO-67-Ir(ppy^F)₂, a hot filtration experiment was carried out after 4 h of photocatalysis, after which no further conversion of substrate was observed. Furthermore, no significant leaching of iridium was observed, as evidenced by ICP-OES analysis of the filtrate (<0.1 ppm Ir). UiO-67-Ir(ppy^F)₂ also exhibited excellent recyclability with good yields and high selectivity over three cycles (Table 3-4). Between each run, the catalyst was recovered, and directly used for the next reaction. The crystallinity was maintained after each cycle, which was confirmed by PXRD (Figure 3-11), showing the robust nature of UiO-67 platform even under the mildly basic conditions and stirring required for these reactions.

Table 3-1 Conversions and yields of photocatalytic trifluoroethylation of styrene.^a

Entry	Catalyst	$h\nu$	%Con	Yield ^b A/B/C %
1	Ir(ppy) ₃	+	99	10/9/80
2	[Ir(ppy) ₂ (Et ₂ dc bpy)]Cl	+	99	20/7/72
3	[Ir(ppy ^F) ₂ (Et ₂ dc bpy)]Cl	+	99	32/8/60
4	UiO-67-Ir(ppy) ₂	+	99	60/11/28
5	UiO-67-Ir(ppy ^F) ₂	+	99	76/18/2
6	No Catalyst	+	0	0
7	UiO-67-bpy _{0.25}	+	0	0
8	UiO-67-Ir(ppy ^F) ₂	-	0	0

^aReaction conditions: 4-methoxystyrene (0.1 mmol), 2-iodo-1,1,1-trifluoroethane (0.3 mmol), N,N-Diisopropylethylamine (0.3 mmol), acetonitrile (2 mL) and water (200 μ L), catalyst (5 mol%), 32 W compact fluorescent bulb, room temperature under air atmosphere for 48 h. ^bDetermined by GC-MS.

The substrate scope of the photocatalytic trifluoroethylation reaction was tested and is summarized in Table 3-2. The majority of substrates gave quantitative conversions and all showed high selectivity for hydroxytrifluoroethyl over dimerization products using 5 mol% UiO-67-Ir(ppy^F)₂ as catalyst. A higher conversion efficiency was observed with electron-rich styrenes (Table 3-2, Entry 1-3). 4-Bromostyrene (Table 3-2, Entry 4) shows lower conversion because of the electron-withdrawing nature of the bromine group, which is consistent with other reports of these photocatalysts.¹⁰ Larger substrates, such as 4-vinylbiphenyl, also proved to be a suitable substrate for the reaction, giving quantitative conversion and good selectivity.

Table 3-2 Substrate scope using UiO-67-Ir(ppy^{F'})₂ as photocatalyst.^a

Entry	Substrate	%Con	Yield ^b A/B/C %
1		99	76/18/2
2		95	70/20/4
3		83	74/9/0
4		49	43/6/0
5		97	60/0/0

^aReaction conditions: styrene substrate (0.1 mmol), 2-iodo-1,1,1-trifluoroethane (0.3 mmol), N,N-Diisopropylethylamine (0.3 mmol), acetonitrile (2 mL) and water (200 μ L), UiO-67-Ir(ppy^{F'})₂ as catalyst (5 mol%), 32 W compact fluorescent bulb, room temperature under air atmosphere for 48h. ^bDetermined by GC-MS

3.4 Conclusion

In conclusion, PSM is shown to be an efficient functionalization method to incorporate photocatalytic, cyclometalated iridium complexes into a robust UiO-67 material. The resulting MOF systems were used as heterogeneous photocatalysts for trifluoroethylation reactions of styrenes with high yields under visible-light irradiation, for at least three cycles without significant loss of activity. Most importantly, the MOF catalysts favored the formation of the desired hydroxytrifluoroethyl products, while suppressing dimerization of benzyl radicals that results in undesirable byproducts. This is in stark contrast when compared to the homogeneous catalysts, and is likely due to confined space within the pores of MOF structure. This

unprecedented product selectivity shows a new feature of the ‘MOF effect’ and may be useful for other chemical reactions where suppressing the formation of undesirable byproducts is a challenge.

3.5 Experimental

General Methods. Starting materials and solvents were purchased and used without further purification from commercial suppliers (Sigma-Aldrich, Alfa Aesar, EMD, TCI, Cambridge Isotope Laboratories, Inc., and others). Proton nuclear magnetic resonance spectra (^1H NMR) were recorded on a Varian FT-NMR spectrometer (400 MHz). Chemical shifts were quoted in parts per million (ppm) referenced to the appropriate solvent peak or 0 ppm for TMS. Gas-chromatography mass-spectroscopy (GC-MS) was recorded on an Agilent instrument (Agilent 6890N/5975). Centrifugation was performed using a Beckman Coulter Allegra X-22R Centrifuge, with a fixed-angle rotor at 6800 rpm for 10 min.

Synthesis of UiO-67-bpy_{0.25}. ZrCl_4 (120 mg, 0.514 mmol), benzoic acid (1.88g, 15.4 mmol), H_2bpdc (biphenyldicarboxylic acid, 94 mg, 0.39 mmol), and H_2dcbpy (2,2'-bipyridine-5,5'-dicarboxylic acid, 31 mg, 0.13 mmol) were placed in a vial with 20 mL of DMF. The solids were dispersed via sonication for ~10 min, followed by incubation at 120 °C for 24 h. After cooling, solids were collected by centrifugation and the solvent was decanted. The solids were washed with DMF (2×20 mL), followed by soaking in ethanol (EtOH) for 3 d, and the solution was exchanged with fresh EtOH (10 mL) every 24 h. After 3 d of soaking, the solids were collected via centrifugation and dried under vacuum to produce white powder MOF.

Synthesis of UiO-67-Ir(ppy)₂ via PSM. Diiridium complex $[\text{Ir}(\text{ppy})_2\text{Cl}]_2$ was synthesized by using the published procedure.²⁷ $[\text{Ir}(\text{ppy})_2\text{Cl}]_2$ (11mg, 0.015 mmol) was dissolved in

dichloromethane (1 mL) and MeOH (1 mL). UiO-67-bpy_{0.25} (35.53 mg, 0.1 mmol) was added into the solution. The mixture was sonicated for 10 min to disperse UiO particles in solution, followed by incubation at 55 °C for 24h to produce orange UiO-67-Ir(ppy)₂ with 20% Ir loading. The solid was washed with dichloromethane (3 × 15 mL) and methanol (3 × 15 mL), followed by soaking in methanol for 3 days, and the solution was exchanged with fresh methanol every 24h. For further analysis, the solids were collected via centrifugation and dried under vacuum.

Synthesis of UiO-67-Ir(ppy^{F'})₂ via PSM. Diiridium complex [Ir(ppy^{F'})₂Cl]₂ was synthesized by following the published procedure.²⁶ [Ir(ppy^{F'})₂Cl]₂ (15mg, 0.015 mmol) was dissolved in dichloromethane (1 mL) and MeOH (1 mL). UiO-67-bpy_{0.25} (35.53 mg, 0.1 mmol) was added into the solution. The mixture was sonicated for 10 min to disperse UiO particles in solution, followed by incubation at 55 °C for 72h to produce bright yellow UiO-67-Ir(ppy^{F'})₂ with 9% Ir loading. The solids were washed with dichloromethane (3 × 15 mL) and methanol (3 × 15 mL), followed by soaking in methanol for 3 days, and the solution was exchanged with fresh methanol every 24h. For further analysis, the solids were collected via centrifugation and dried under vacuum.

Synthesis of bis(4-phenyl-2-pyridine)(5,5'-diethoxycarboxyl-2,2'-bipyridine)iridium(III) chloride ([Ir(ppy)₂(Et₂dc bpy)]Cl). [Ir(ppy)₂(Et₂dc bpy)]Cl was synthesized by following reported procedure.²⁷

Synthesis of bis(2-(2,4-difluorophenyl)-5-(trifluoromethyl)pyridine)(5,5'-diethoxycarboxyl-2,2'-bipyridine)iridium(III) chloride ([Ir(ppy^{F'})₂(Et₂dc bpy)]Cl). [Ir((ppy^{F'})₂Cl)₂ (285mg, 0.19 mmol) and (2,2'-bipyridine)-5,5'-dicarboxylic acid diethyl ester (112 mg, 0.37 mmol) were suspended in 15 mL 1:1 MeCN/CHCl₃ under nitrogen. After refluxing overnight, evaporation of the solvent under reduced pressure yielded a yellow solid.

The solid was purified by silica column with DCM/MeOH 30% to produce target complex (200mg, 55%). ^1H NMR (CDCl_3): 9.96 (d, 2H), 8.92 (dd, 2H), 8.5 (d, 2H), 8.41 (s, 2H), 8.08 (d, 2H), 7.57 (s, 2H), 6.70 (t, 2H), 5.27 (d, 2H), 4.35 (q, 4H), 1.33 (t, 6H).

Photocatalytic trifluoroethylation reaction under air. Styrene substrate (0.1 mmol), 2-Iodo-1,1,1-trifluoroethane (0.3 mmol) and N,N-Diisopropylethylamine (0.3 mmol) were mixed and dissolved in 2 mL acetonitrile and 200 μL water in a 10 mL round-bottom flask. UiO-67- $\text{Ir}(\text{ppy}^{\text{F}})_2$ (5 mol% w.r.t Ir complex, 25mg) was added to the solution and sonicated for 5 mins. The mixture was irradiated by a 32 W compact fluorescent bulb at room temperature under air atmosphere for 48h with stirring. After the reaction was complete, the supernatant was separated by centrifugation, 30 μL supernatant was diluted in 1 mL acetone and analyzed by GC-MS. Time-dependent catalysis experiments were carried out under same condition, using GC-MS to monitor conversion and yield during process. To test recyclability, the supernatant was decanted from the catalyst after 48h reaction and the catalyst was washed with acetonitrile (3×10 mL). The washed MOFs were directly used for the next round trifluoroethylation catalysis for the same substrate.

Photocatalytic trifluoroethylation reaction under N_2 . In a 10 mL Schlenk flask, 4-methoxystyrene (0.1 mmol), 2-Iodo-1,1,1-trifluoroethane (0.3 mmol) and N,N-Diisopropylethylamine (0.3 mmol) were mixed and dissolved in 2 mL anhydrous acetonitrile. Catalyst ($\text{Ir}(\text{ppy})_3$ or UiO-67- $\text{Ir}(\text{ppy}^{\text{F}})_2$, 0.005 mol) was added into the solution. The mixture was degassed and backfilled with N_2 using freeze-pump-thaw method. The reaction mixture was irradiated by a 32W compact fluorescent bulb at room temperature for 24h with stirring. After the reaction was complete, the supernatant was separated by centrifugation, 30 μL supernatant was diluted in 1 mL acetone and analyzed by GC-MS.

Powder X-ray Diffraction (PXRD) Analysis. ~20-30 mg of UiO-67 derivative material was dried under vacuum prior to PXRD analysis. PXRD data were collected at ambient temperature on a Bruker D8 Advance diffractometer at 40 kV, 40 mA for Cu K α (λ = 1.5418 Å), with a scan speed of 1 sec/step, a step size of 0.02° in 2 θ , and a 2 θ range of ~5 to 40° (sample dependent). The experimental background was corrected using the Jade 5.0 software package.

Digestion and Analysis by ¹HNMR. ~10 mg of UiO-67-bpy material was dried under vacuum and digested with sonication in 600 μ L *d*₆-DMSO and 10 μ L of 40% HF. Approximately 10 mg UiO-67-Ir was suspended in a 0.1 M solution (1 mL) of D₃PO₄ in D₂O/*d*⁶-DMSO (prepared by mixing 11.9 mg of a solution of D₃PO₄ (85% in D₂O) with 1 mL *d*⁶-DMSO) and sonicated for 20 mins. The solution was filtered through cotton and placed in an NMR tube.

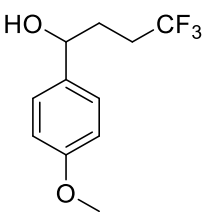
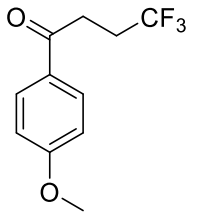
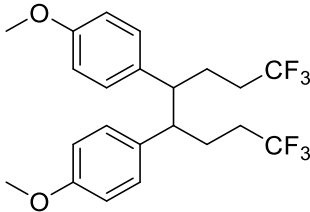
BET Surface Area Analysis. ~50 mg of UiO-67 derivative material was evacuated on a vacuum line overnight at room temperature. The sample was then transferred to a pre-weighed sample tube and degassed at 105 °C on an Micromeritics ASAP 2020 Adsorption Analyzer for a minimum of 12 h or until the outgas rate was <5 mm Hg. The sample tube was re-weighed to obtain a consistent mass for the degassed exchanged MOF. BET surface area (m²/g) measurements were collected at 77 K by N₂ on a Micromeritics ASAP 2020 Adsorption Analyzer using the volumetric technique, and the surface areas reported for each material is the average of three independent samples.

3.6 Appendix

Table 3-3 BET surface areas of UiO MOFs.

Entry	MOF	BET (m ² /g)
1	UiO-67-bpy _{0.25}	2480 ± 55
2	UiO-67-Ir(ppy) ₂	2118 ± 21
3	UiO-67-Ir(ppy ^F) ₂	2002 ± 18

Table 3-4 Recyclability test of UiO-67-Ir(ppy^F)₂ for trifluoroethylation of 4-methoxystyrene.

Product			
Cycle 1 yield (%) ^a	74	16	5
Cycle 2 yield (%) ^a	77	16	3
Cycle 3 yield (%) ^a	76	20	2

^aBased on GC-MS analysis

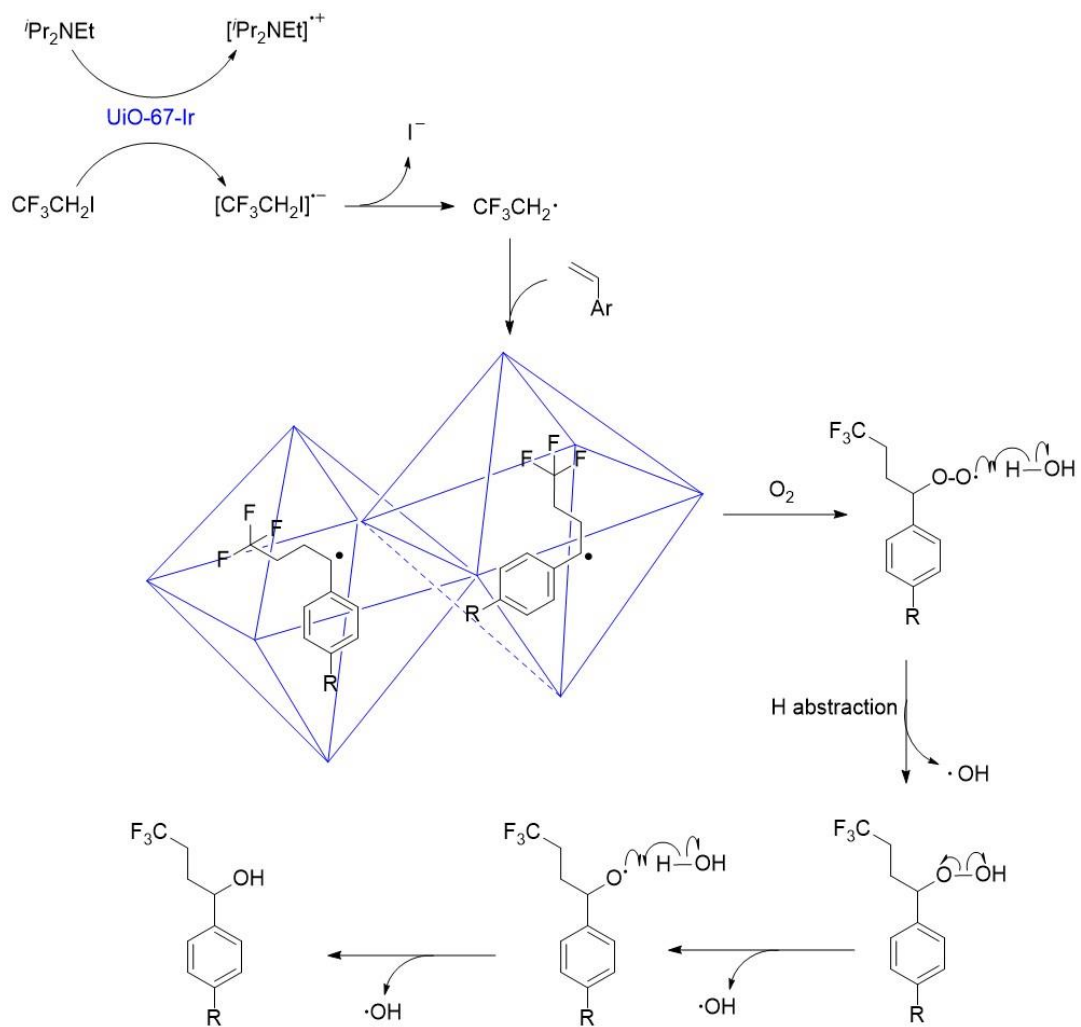


Figure 3-3 Proposed mechanism of UiO-67-Ir catalyzed trifluoroethylation reaction.

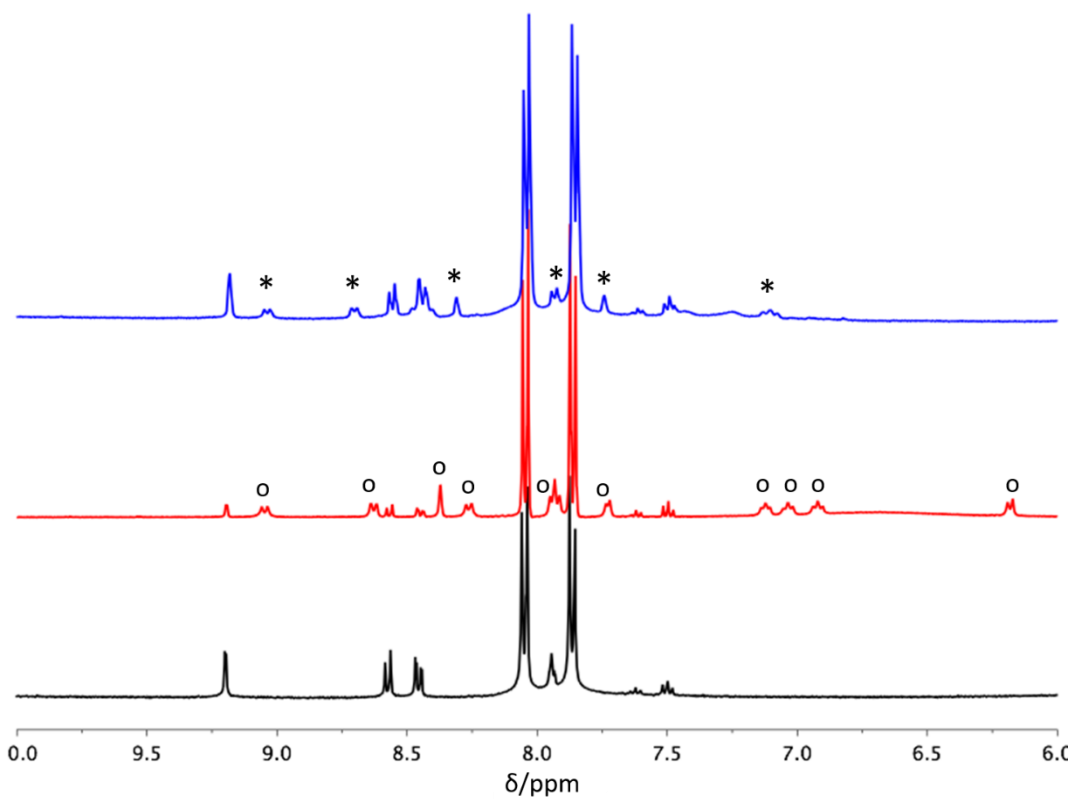


Figure 3-4 ^1H NMR ($\text{D}_3\text{PO}_4/\text{d}^6\text{-DMSO}$) of digested UiO-67-bpy $_{0.25}$ (black), UiO-67-Ir(ppy) $_2$ (red, with $[\text{Ir}(\text{ppy})_2(\text{dcbpy})]^+$ denoted by “o”) and UiO-67-Ir(ppy $^{\text{F}}$) $_2$ (blue, with $[\text{Ir}(\text{ppy}^{\text{F}})_2(\text{dcbpy})]^+$ denoted by “*”).

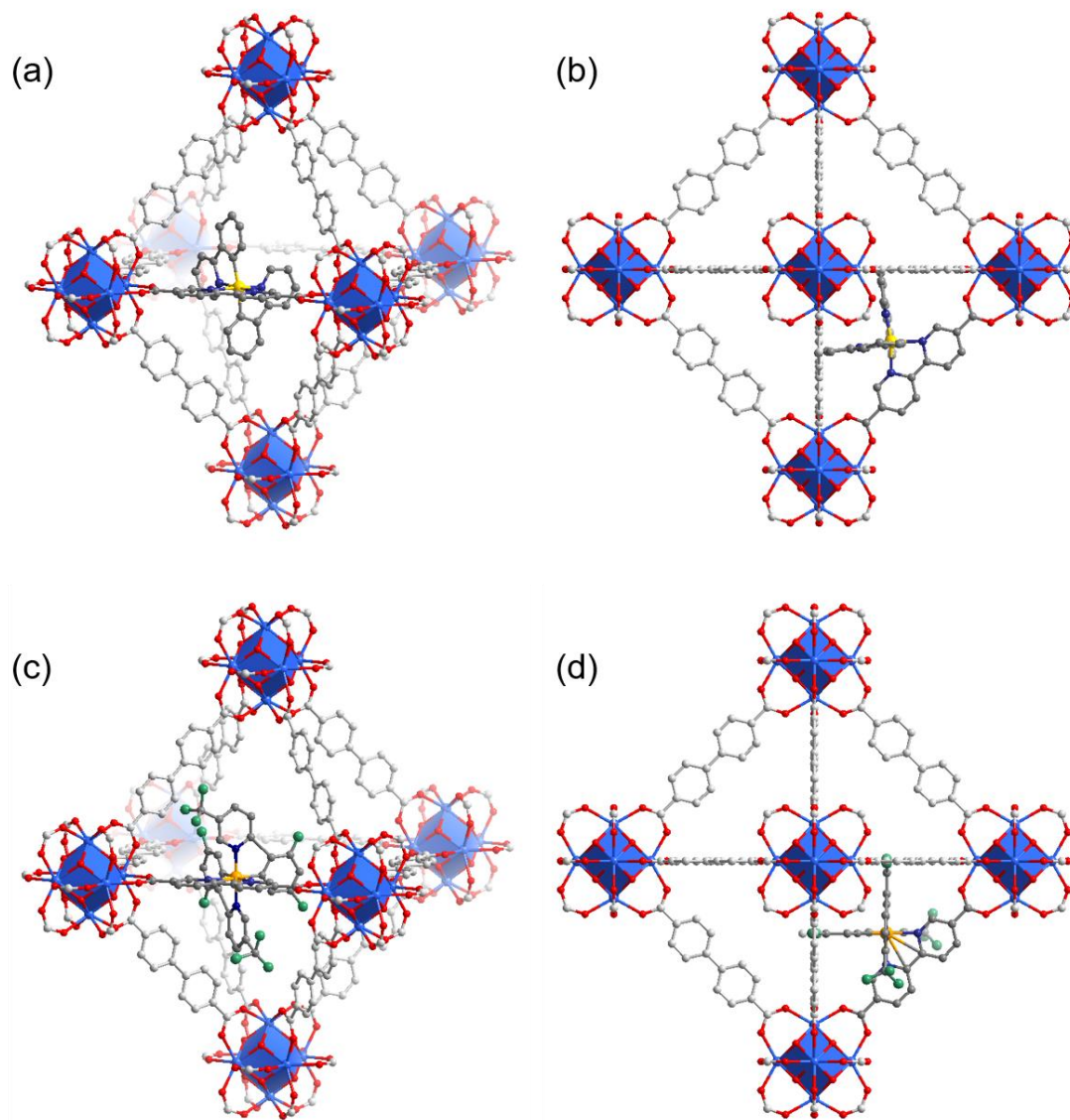


Figure 3-5 Models of UiO-67-Ir MOFs. (a),(b) UiO-67-Ir(ppy)₂; (c),(d) UiO-67-Ir(ppy^F)₂.

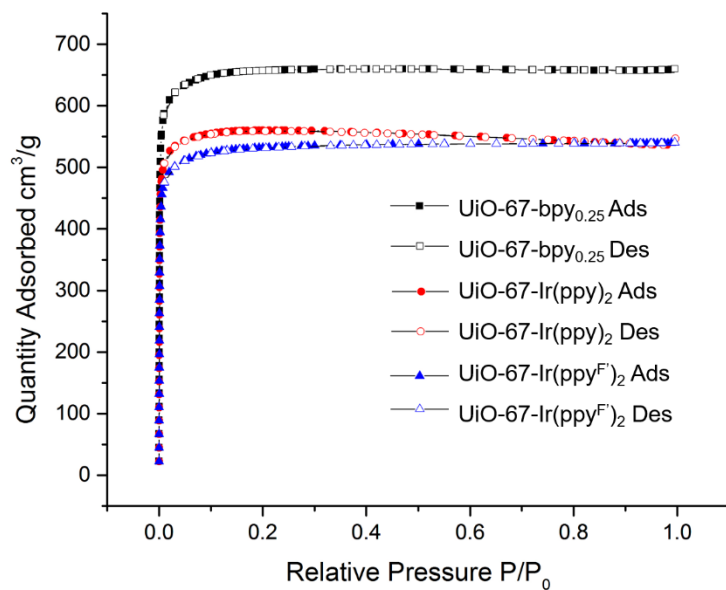


Figure 3-6 N₂ adsorption at 77K for UiO-67-Ir MOFs.

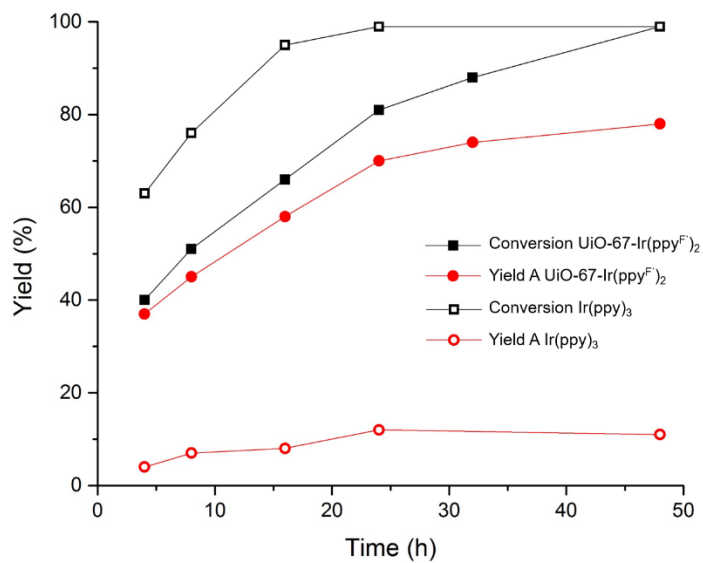


Figure 3-7 Time-dependent catalysis by UiO-67-Ir(ppy^F)₂ and Ir(ppy)₃.

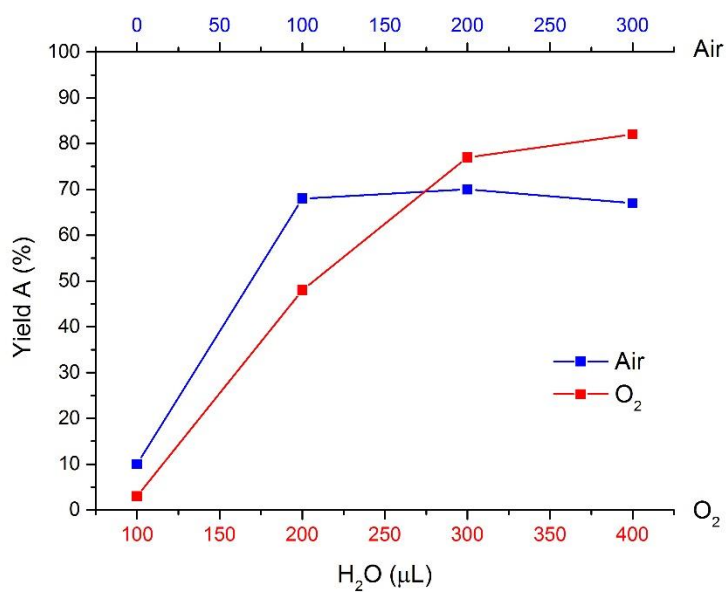


Figure 3-8 Effect of water content on hydroxytrifluoroethylation catalyzed by UiO-67-Ir(ppy^{F'})₂.

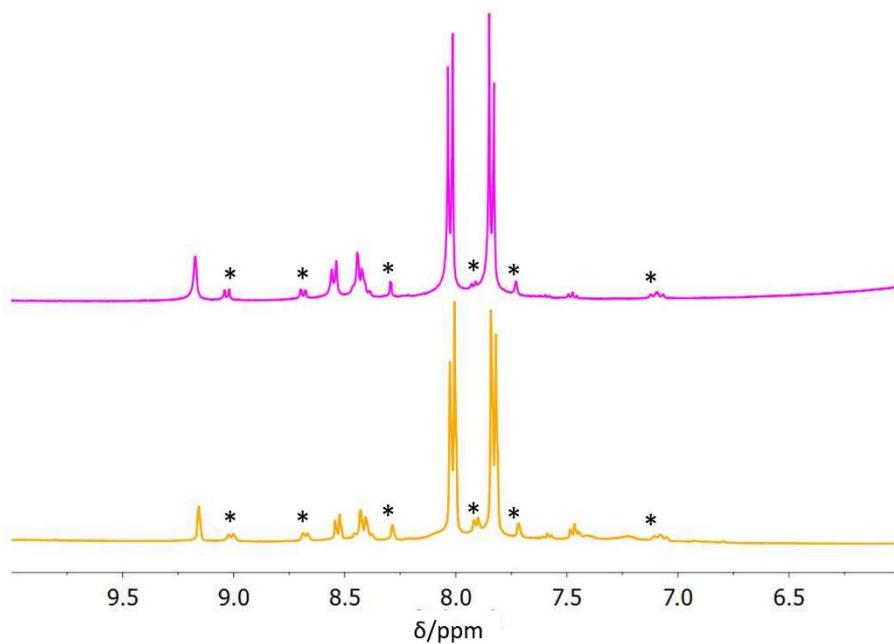


Figure 3-9 ¹H NMR of digested UiO-67-Ir(ppy^{F'})₂ before (orange) and after (pink) catalytic reaction (with [Ir(ppy^{F'})₂(dcbpy)]⁺ denoted by “*”).

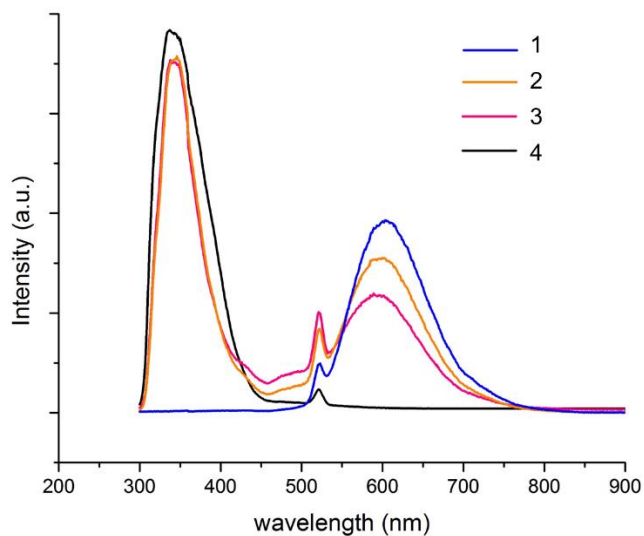


Figure 3-10 Photoluminescent spectra (excitation $\lambda = 261$ nm) of (1). $\text{Ir}(\text{ppy}^{\text{F}^{\prime}})_2(\text{Et}_2\text{dcby})\text{Cl}$; (2). digested As-synthesized $\text{UiO-67-Ir}(\text{ppy}^{\text{F}^{\prime}})_2$; (3). digested $\text{UiO-67-Ir}(\text{ppy}^{\text{F}^{\prime}})_2$ after catalytic reaction; (4). digested $\text{UiO-67-bpy}_{0.25}$.

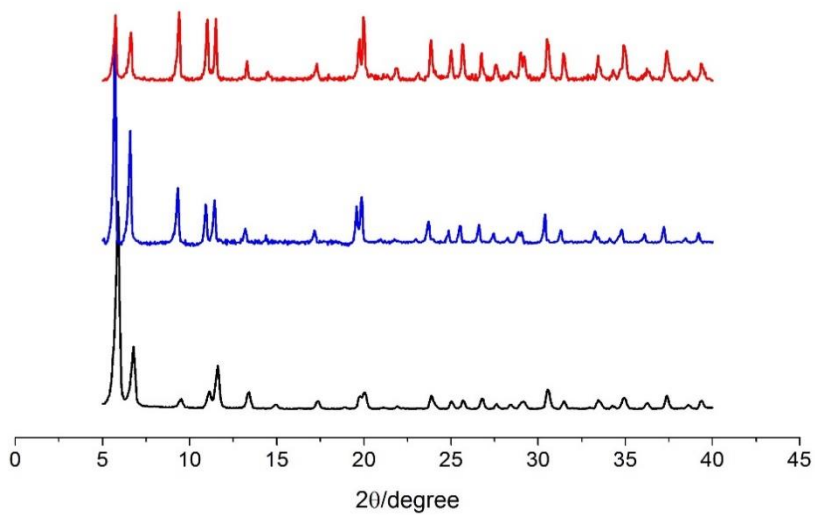


Figure 3-11 PXRD of $\text{UiO-67-Ir}(\text{ppy}^{\text{F}^{\prime}})_2$ after cycle 1 (black), cycle 2 (blue) and cycle 3 (red).

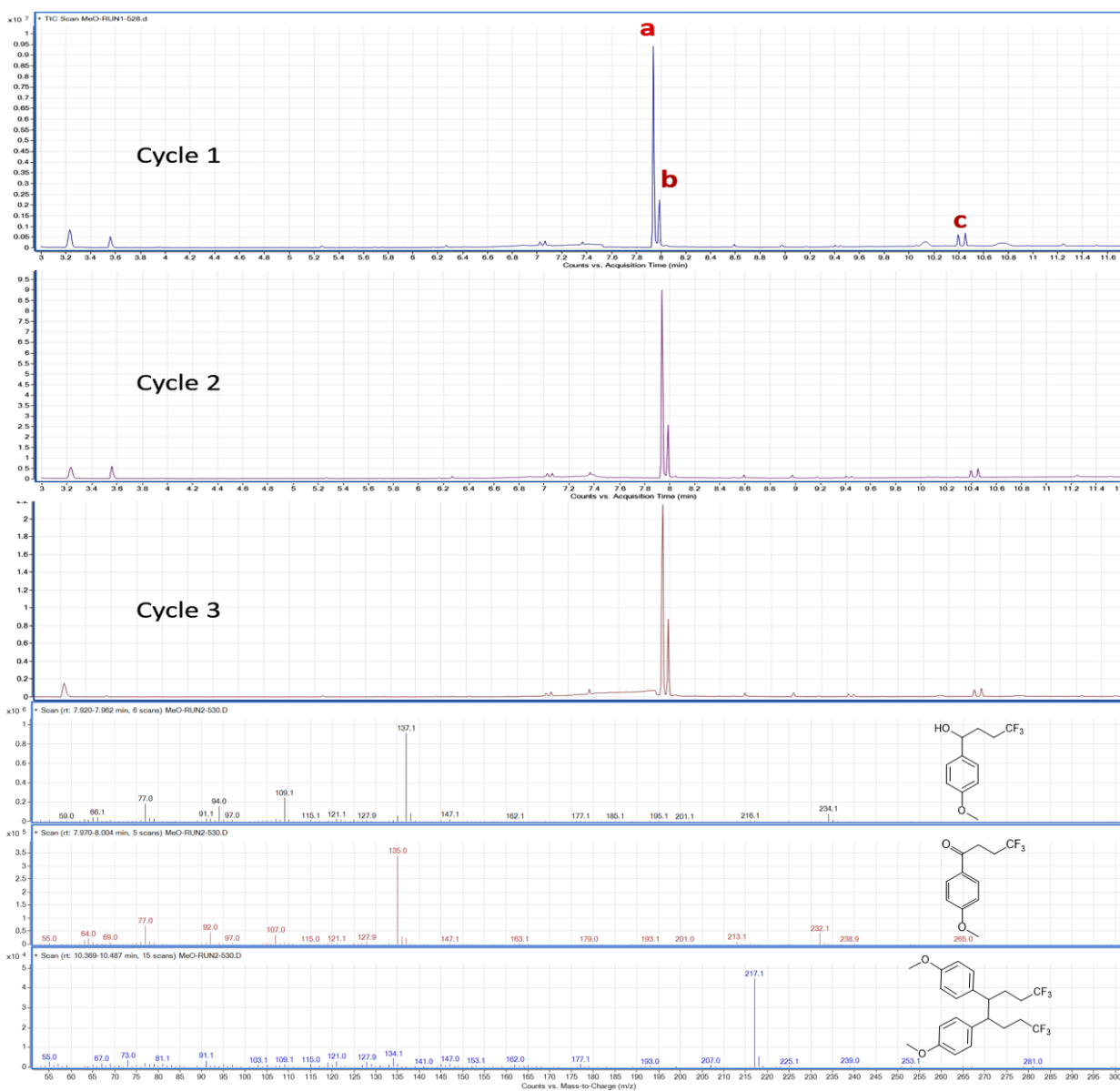
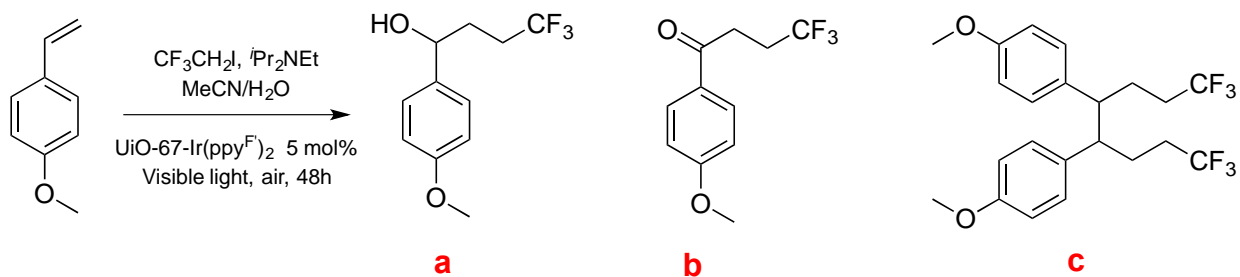


Figure 3-12 GC-MS of 4-methoxystyrene trifluoroethylation reaction catalyzed by UiO-67-Ir(ppy^F)₂ for 3 cycles. First two small peaks are solvent and N, N- Diisopropylethylamine (RT < 4 mins).

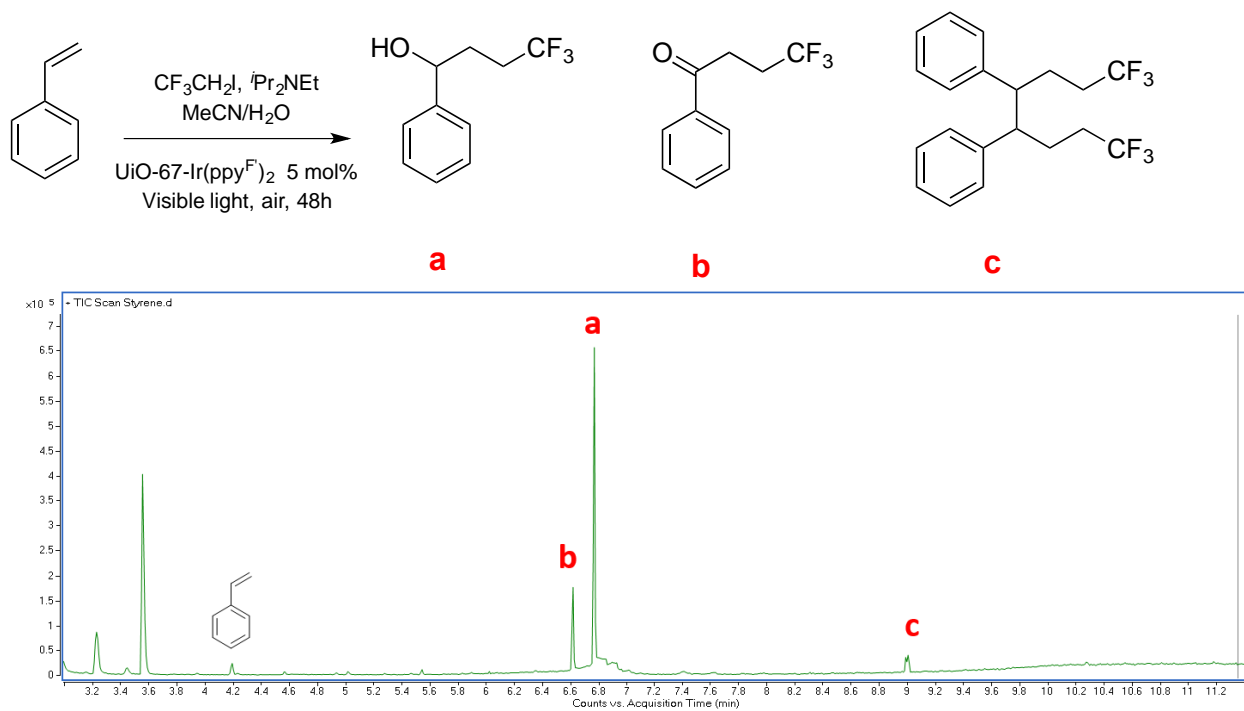


Figure 3-13 GC-MS of styrene trifluoroethylation reaction catalyzed by UiO-67-Ir(ppy^{F'})₂.

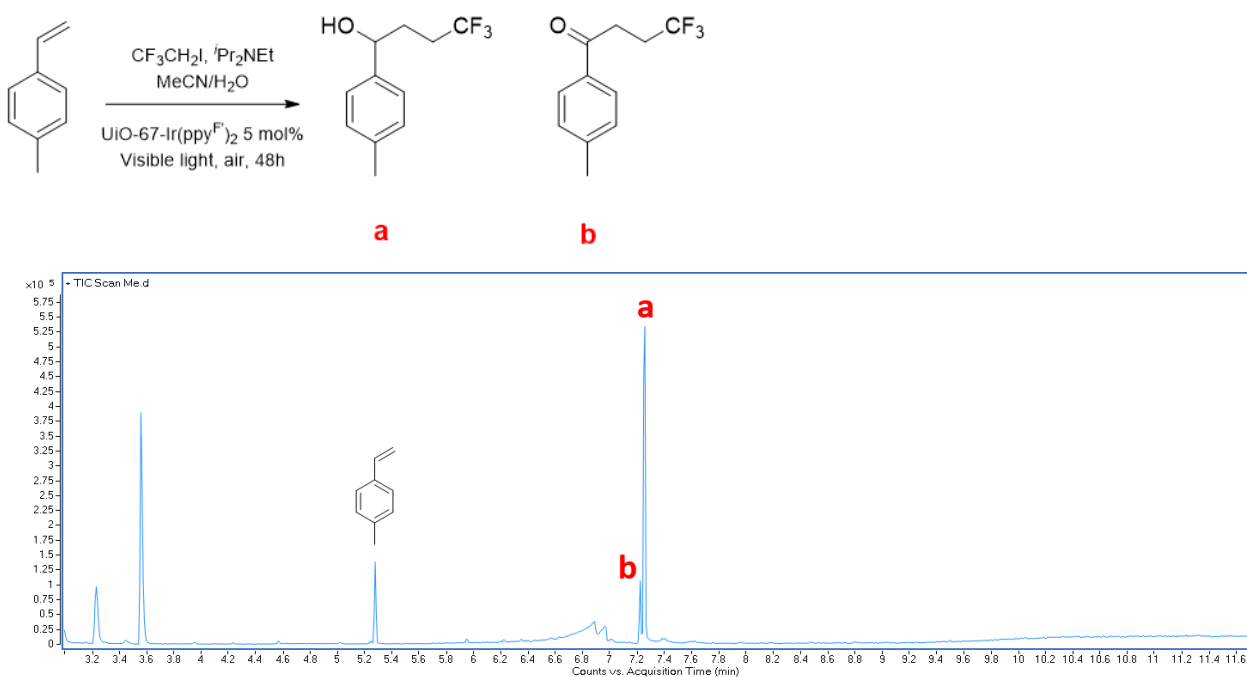


Figure 3-14 GC-MS of 4-methylstyrene trifluoroethylation reaction catalyzed by UiO-67-Ir(ppy^{F'})₂. No dimerization product was found in the reaction mixture.

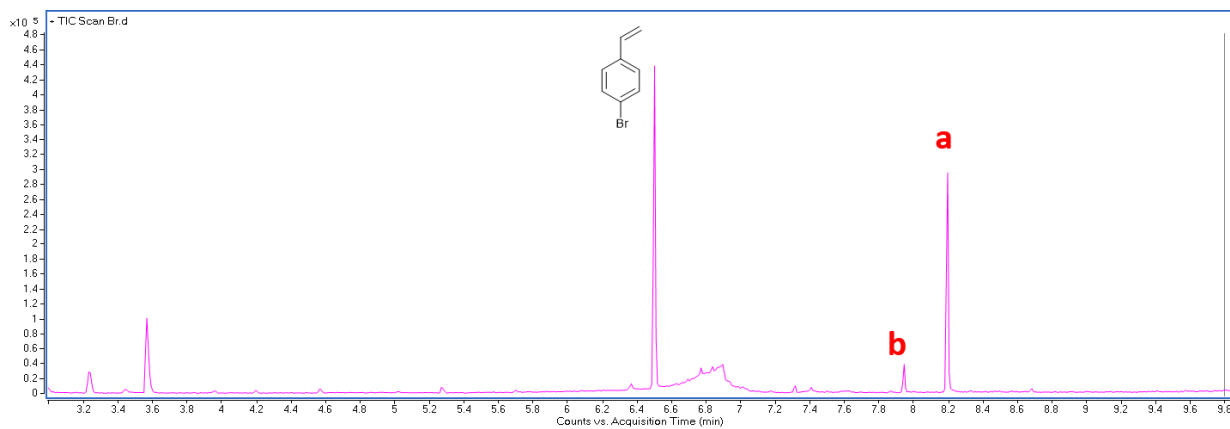
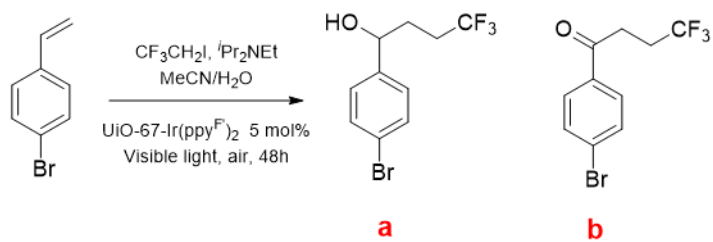


Figure 3-15 GC-MS of 4-bromostyrene trifluoroethylation reaction catalyzed by UiO-67-Ir(ppy^F)₂. No dimerization product was found in the reaction mixture.

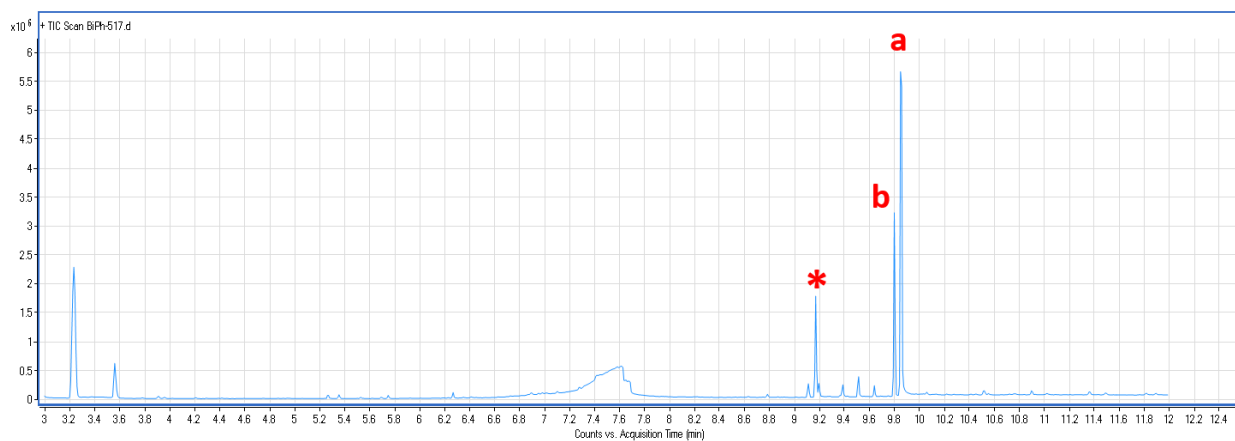
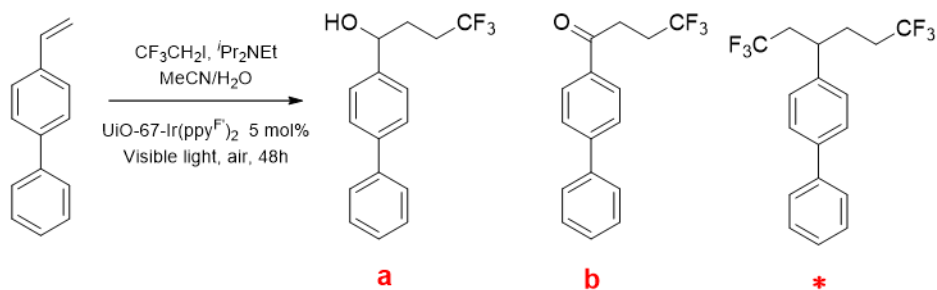


Figure 3-16 GC-MS of 4-vinylbiphenyl trifluoroethylation reaction catalyzed by UiO-67-Ir(ppy^F)₂. No dimerization product was found in the reaction mixture. Isolated yields were used for this substrate because of high boiling point of the products.

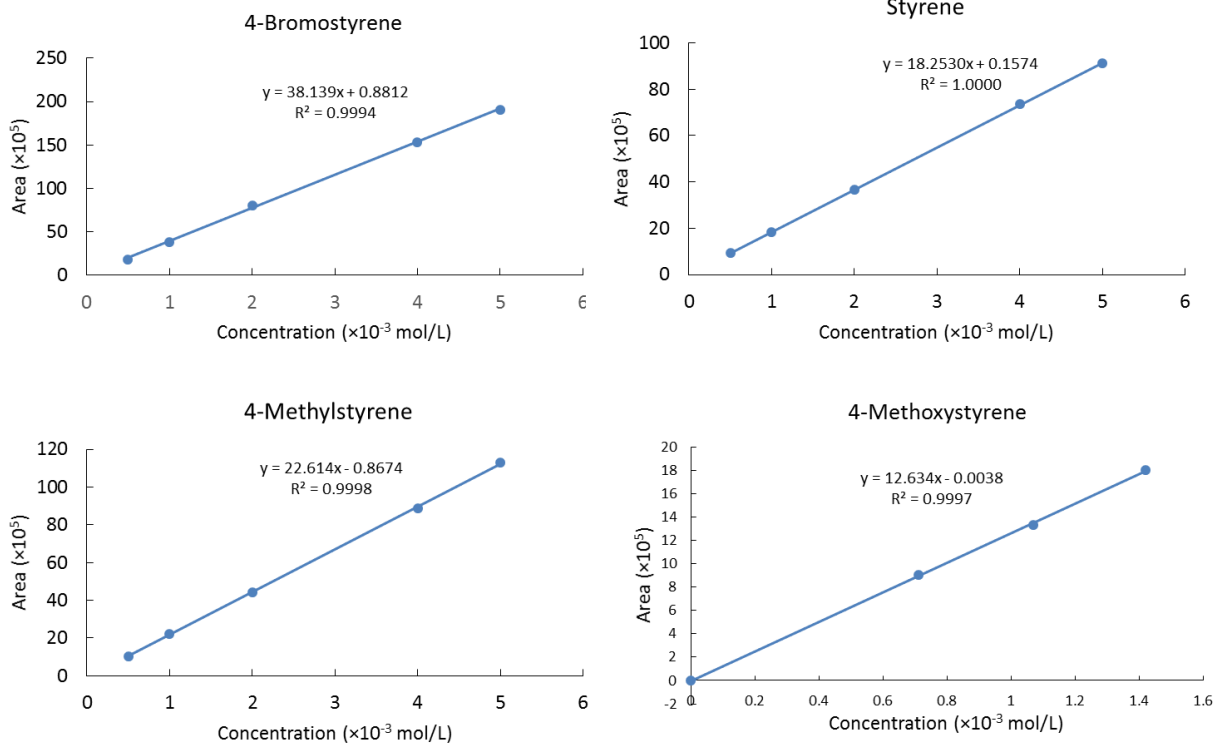


Figure 3-17 GC-MS calibration curves of styrenes.

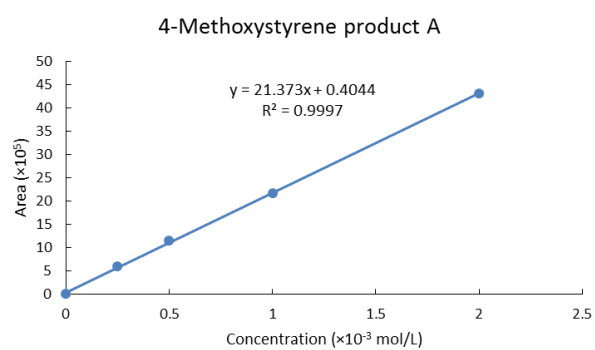
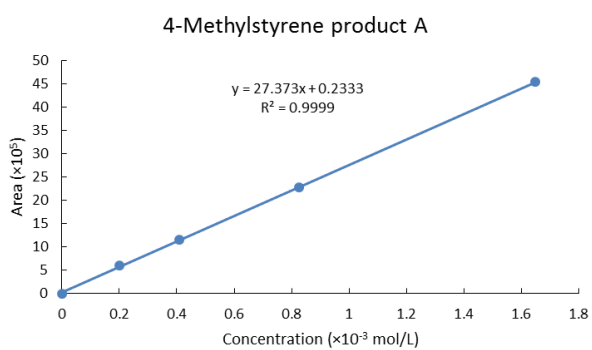
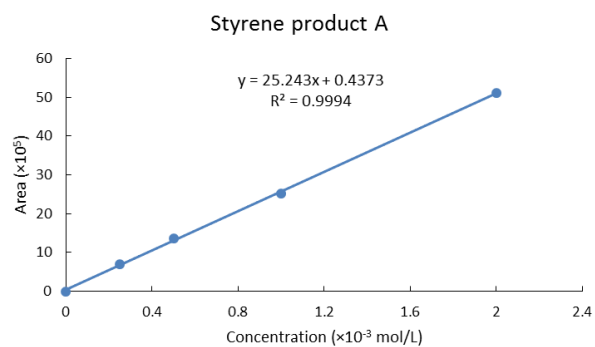
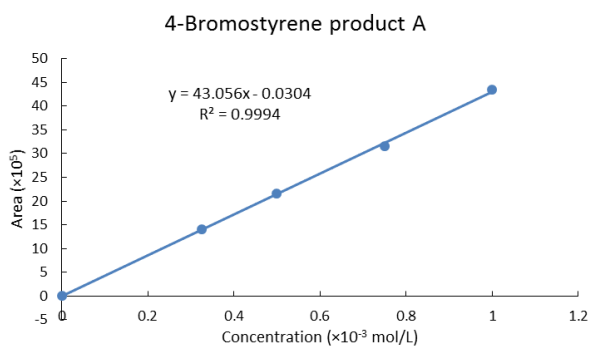


Figure 3-18 GC-MS calibration curves of product A (hydroxyethylation products) of different substrates.

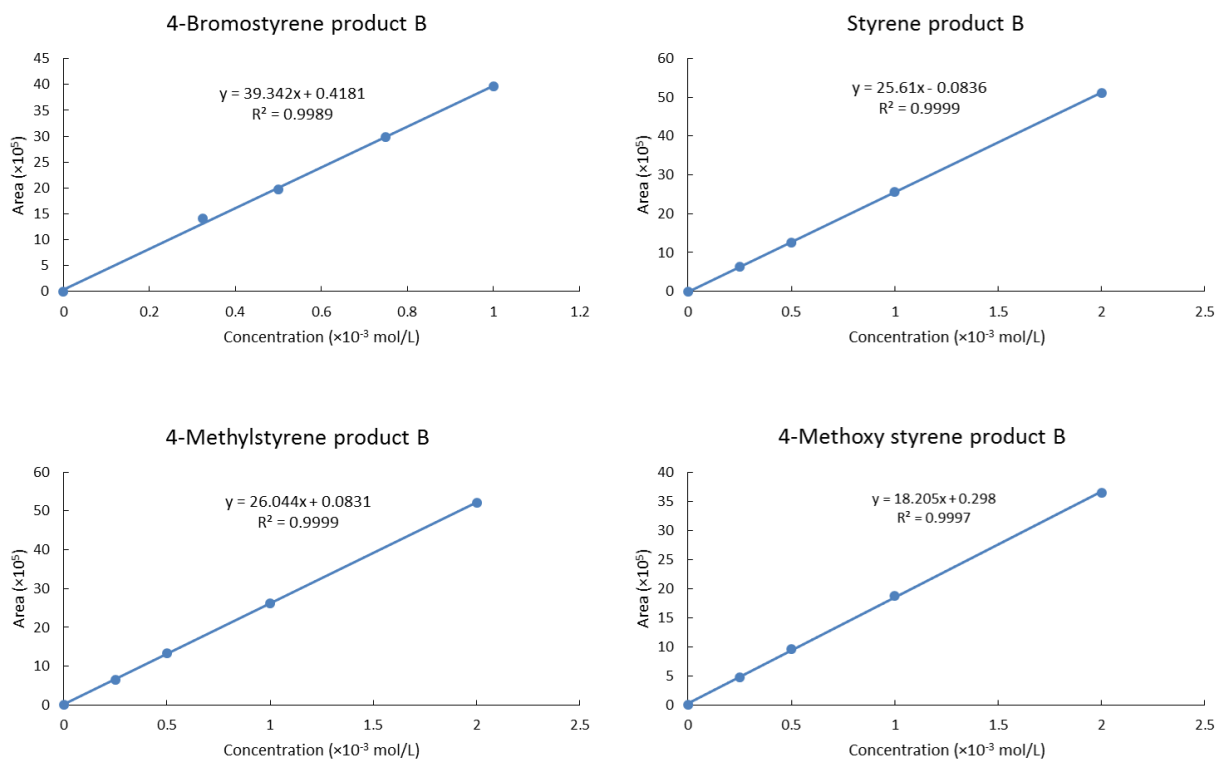


Figure 3-19 GC-MS calibration curves for product B (ketones) of different substrates.

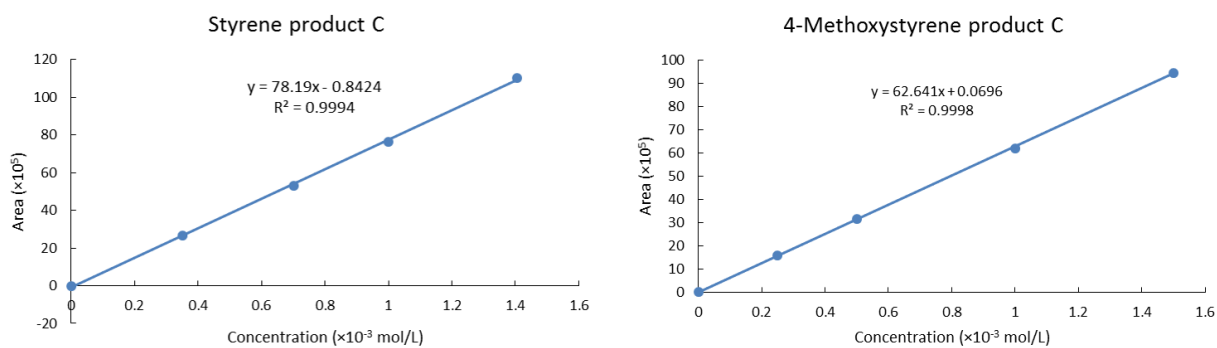


Figure 3-20 GC-MS calibration curves for product C (dimerization products) for two substrates. Other substrates did not show any dimerization product.

3.7 Acknowledgements

Text, tables, and figures in this chapter are, in large part, reprints of materials published in the paper: Xiao Yu and Seth M. Cohen*, “Photocatalytic Metal–Organic Frameworks for Selective 2,2,2-Trifluoroethylation of Styrenes” *J. Am. Chem. Soc.* **2016**, *138*, 12320-12323. The dissertation author was the primary researcher for the data presented and was the primary author of this publication. The permissions to reproduce this material were granted by the American Chemistry Society, copyright 2016.

3.8 References

1. Gouverneur, V.; Seppelt, K., Introduction: fluorine chemistry. *Chem. Rev.* **2015**, *115* (2), 563-565.
2. O'Hagan, D., Understanding organofluorine chemistry. An introduction to the C–F bond. *Chem. Soc. Rev.* **2008**, *37* (2), 308-319.
3. Meanwell, N. A., Synopsis of some recent tactical application of bioisosteres in drug design. *J. Med. Chem.* **2011**, *54* (8), 2529-2591.
4. Purser, S.; Moore, P. R.; Swallow, S.; Gouverneur, V., Fluorine in medicinal chemistry. *Chem. Soc. Rev.* **2008**, *37* (2), 320-330.
5. Furuya, T.; Kamlet, A. S.; Ritter, T., Catalysis for fluorination and trifluoromethylation. *Nature* **2011**, *473* (7348), 470-477.
6. Liu, X.; Xu, C.; Wang, M.; Liu, Q., Trifluoromethyltrimethylsilane: nucleophilic trifluoromethylation and beyond. *Chem. Rev.* **2014**, *115* (2), 683-730.
7. Charpentier, J.; Früh, N.; Togni, A., Electrophilic trifluoromethylation by use of hypervalent iodine reagents. *Chem. Rev.* **2014**, *115* (2), 650-682.
8. Xu, X.-H.; Matsuzaki, K.; Shibata, N., Synthetic methods for compounds having CF₃–S units on carbon by trifluoromethylation, trifluoromethylthiolation, triflylation, and related reactions. *Chem. Rev.* **2014**, *115* (2), 731-764.

9. Tomashenko, O. A.; Grushin, V. V., Aromatic trifluoromethylation with metal complexes. *Chem. Rev.* **2011**, *111* (8), 4475-4521.
10. Li, L.; Huang, M.; Liu, C.; Xiao, J.-C.; Chen, Q.-Y.; Guo, Y.; Zhao, Z.-G., 2, 2, 2-Trifluoroethylation of Styrenes with Concomitant Introduction of a Hydroxyl Group from Molecular Oxygen by Photoredox Catalysis Activated by Visible Light. *Org. Lett.* **2015**, *17* (19), 4714-4717.
11. Kreis, L. M.; Krautwald, S.; Pfeiffer, N.; Martin, R. E.; Carreira, E. M., Photocatalytic synthesis of allylic trifluoromethyl substituted styrene derivatives in batch and flow. *Org. Lett.* **2013**, *15* (7), 1634-1637.
12. Fujiwara, Y.; Dixon, J. A.; O'Hara, F.; Funder, E. D.; Dixon, D. D.; Rodriguez, R. A.; Baxter, R. D.; Herlé, B.; Sach, N.; Collins, M. R., Practical and innate carbon-hydrogen functionalization of heterocycles. *Nature* **2012**, *492* (7427), 95-99.
13. Liu, J.; Chen, L.; Cui, H.; Zhang, J.; Zhang, L.; Su, C.-Y., Applications of metal-organic frameworks in heterogeneous supramolecular catalysis. *Chem. Soc. Rev.* **2014**, *43* (16), 6011-6061.
14. Cohen, S. M.; Zhang, Z.; Boissonault, J. A., Toward "metalloMOFzymes": Metal-Organic Frameworks with Single-Site Metal Catalysts for Small-Molecule Transformations. *Inorg. Chem.* **2016**, *55* (15), 7281-7290.
15. Horike, S.; Dinca, M.; Tamaki, K.; Long, J. R., Size-selective Lewis acid catalysis in a microporous metal-organic framework with exposed Mn²⁺ coordination sites. *J. Am. Chem. Soc.* **2008**, *130* (18), 5854-5855.
16. Pan, L.; Liu, H.; Lei, X.; Huang, X.; Olson, D. H.; Turro, N. J.; Li, J., RPM - 1: A Recyclable Nanoporous Material Suitable for Ship - In - Bottle Synthesis and Large Hydrocarbon Sorption. *Angew. Chem. Int. Ed.* **2003**, *42* (5), 542-546.
17. Farrusseng, D.; Aguado, S.; Pinel, C., Metal-organic frameworks: opportunities for catalysis. *Angew. Chem. Int. Ed.* **2009**, *48* (41), 7502-7513.
18. Wu, P.; He, C.; Wang, J.; Peng, X.; Li, X.; An, Y.; Duan, C., Photoactive chiral metal-organic frameworks for light-driven asymmetric α -alkylation of aldehydes. *J. Am. Chem. Soc.* **2012**, *134* (36), 14991-14999.
19. Sawano, T.; Thacker, N. C.; Lin, Z.; McIsaac, A. R.; Lin, W., Robust, Chiral, and Porous BINAP-Based Metal-Organic Frameworks for Highly Enantioselective Cyclization Reactions. *J. Am. Chem. Soc.* **2015**, *137* (38), 12241-12248.

20. Beyzavi, M. H.; Klet, R. C.; Tussupbayev, S.; Borycz, J.; Vermeulen, N. A.; Cramer, C. J.; Stoddart, J. F.; Hupp, J. T.; Farha, O. K., A hafnium-based metal–organic framework as an efficient and multifunctional catalyst for facile CO₂ fixation and regioselective and enantioselective epoxide activation. *J. Am. Chem. Soc.* **2014**, *136* (45), 15861-15864.
21. Wu, C.-D.; Hu, A.; Zhang, L.; Lin, W., A homochiral porous metal-organic framework for highly enantioselective heterogeneous asymmetric catalysis. *J. Am. Chem. Soc.* **2005**, *127* (25), 8940-8941.
22. Falkowski, J. M.; Sawano, T.; Zhang, T.; Tsun, G.; Chen, Y.; Lockard, J. V.; Lin, W., Privileged phosphine-based metal–organic frameworks for broad-scope asymmetric catalysis. *J. Am. Chem. Soc.* **2014**, *136* (14), 5213-5216.
23. Cho, S.-H.; Ma, B.; Nguyen, S. T.; Hupp, J. T.; Albrecht-Schmitt, T. E., A metal–organic framework material that functions as an enantioselective catalyst for olefin epoxidation. *Chem. Commun.* **2006**, (24), 2563-2565.
24. Banerjee, M.; Das, S.; Yoon, M.; Choi, H. J.; Hyun, M. H.; Park, S. M.; Seo, G.; Kim, K., Postsynthetic modification switches an achiral framework to catalytically active homochiral metal–organic porous materials. *J. Am. Chem. Soc.* **2009**, *131* (22), 7524-7525.
25. Prier, C. K.; Rankic, D. A.; MacMillan, D. W., Visible light photoredox catalysis with transition metal complexes: Applications in organic synthesis. *Chem. Rev.* **2013**, *113* (7), 5322-5363.
26. Tellis, J. C.; Primer, D. N.; Molander, G. A., Single-electron transmetalation in organoboron cross-coupling by photoredox/nickel dual catalysis. *Science* **2014**, *345* (6195), 433-436.
27. Wang, C.; Xie, Z.; deKrafft, K. E.; Lin, W., Doping metal–organic frameworks for water oxidation, carbon dioxide reduction, and organic photocatalysis. *J. Am. Chem. Soc.* **2011**, *133* (34), 13445-13454.
28. Dhakshinamoorthy, A.; Asiri, A. M.; García, H., Metal–Organic Framework (MOF) Compounds: Photocatalysts for Redox Reactions and Solar Fuel Production. *Angew. Chem. Int. Ed.* **2016**, *55* (18), 5414-5445.
29. Yu, X.; Cohen, S. M., Photocatalytic metal–organic frameworks for the aerobic oxidation of arylboronic acids. *Chem. Commun.* **2015**, *51* (48), 9880-9883.
30. Cohen, S. M., Postsynthetic methods for the functionalization of metal–organic frameworks. *Chem. Rev.* **2011**, *112* (2), 970-1000.

31. Thacker, N. C.; Lin, Z.; Zhang, T.; Gilhula, J. C.; Abney, C. W.; Lin, W., Robust and Porous β -Diketiminato-Functionalized Metal–Organic Frameworks for Earth-Abundant-Metal-Catalyzed C–H Amination and Hydrogenation. *J. Am. Chem. Soc.* **2016**, *138* (10), 3501-3509.
32. Zhang, T.; Manna, K.; Lin, W., Metal–Organic Frameworks Stabilize Solution-Inaccessible Cobalt Catalysts for Highly Efficient Broad-Scope Organic Transformations. *J. Am. Chem. Soc.* **2016**, *138* (9), 3241-3249.
33. Rueping, M.; Vila, C.; Szadkowska, A.; Koenigs, R. M.; Fronert, J., Photoredox Catalysis as an Efficient Tool for the Aerobic Oxidation of Amines and Alcohols: Bioinspired Demethylations and Condensations. *ACS Catal.* **2012**, *2* (12), 2810-2815.

Chapter 4 : A Metal-Organic Framework with Exceptional Activity for C–H Bond

Amination

4.1 Introduction

Amine functional groups are of critical importance for bioactive molecules, polymer precursors, and other commodity chemicals. Selective methods for their formation, especially those that reduce synthetic steps and waste generation, have been of long standing interest to the synthetic community.¹ With the advent of late first-row transition-metal catalysts capable of mediating C–H amination of saturated hydrocarbons, direct routes to highly-diversified amine products have become available.² These methods have been inspired by biological systems, most notably the cytochrome P450 class of enzymes that use reactive metal oxo units to effect the activation of hydrocarbon substrates.³⁻⁵ These systems also rely on isolation of the reactive metal-oxo center within a buried protein active site. Accordingly, molecular complexes that perform these transformations must rely on the use of encumbering substituents and highly-active metal-element multiple bonds to achieve reasonable turnover numbers (TONs) before catalyst decomposition. To date, the most active homogenous catalysts for direct amination of hydrocarbon bonds perform with TONs as high as several hundred per active site.^{1, 6-7} Strategies for improving molecular catalysts rely on ancillary-ligand redesign that can increase catalyst stability and lifetime. However, such efforts can also potentially sacrifice substrate accessibility to catalyst active sites. Indeed, in some C–H amination catalysts, increasing steric bulk results in reduced catalyst activity and promotes facile intramolecular catalyst decomposition.⁸

An alternative approach to the use of elaborate ligand architectures is isolation of catalytic sites within a robust, solid-state matrix. The synthetic flexibility of metal-organic frameworks (MOFs) allows for the preparation of metal active sites that are immobilized and separated within a porous lattice.⁹⁻¹⁰ Site isolation via immobilization as part of the MOF lattice

can relax the need to introduce steric encumbrances (as commonly found in molecular catalysts), allowing for facile substrate access to the reactive sites. The use of site isolation within a MOF matrix offers the potential to obtain a catalyst that is resistant to autodegradation, without sacrificing catalytic activity as often required with molecular catalysts.¹¹⁻¹³ Lin et al. have recently reported MOF-based C–H amination systems where a molecular catalyst is constructed on the MOF linkers. This approach has been demonstrated to increase C–H amination catalysis activity 3- to 5-fold relative to homogeneous counterparts.¹⁴⁻¹⁵ Alternatively, the secondary-building units (SBUs) of the MOFs can act as the catalytic active site for multi-electron transformations such as C–H bond amination. This strategy is a departure from embedding molecular-type catalysts into a MOF, and potentially offers both high catalytic activity (i.e. an open active site) and long catalytic lifetimes (i.e. active site stability and isolation) in a single system. Herein, different from functionalized ligands as catalytic sites discussed in chapter 2 and chapter 3, we describe a C–H amination MOF catalyst, based on SBU active sites, with exceptional activity and immortal-like durability.¹⁶

4.2 CPF-5 as Catalyst for Intermolecular C-H Amination

Our search for a MOF with suitable active sites was inspired by first-row transition metal amination catalysts that utilize facially coordinating tripodal ligands,^{8, 17} and studies on MOF catalysts for olefin oligomerization that use related active sites.¹⁸⁻²⁰ Based on these criteria we selected CPF-5 (CPF = coordination porous framework) that has the molecular formula $\text{Mn}_{21}(\text{TZBA})_{12}(\text{HCO}_2)_{18}(\text{H}_2\text{O})_{12}$. CPF-5 is prepared from 4-tetrazolate-benzoic acid (TZBA), ammonium formate, and MnCl_2 to give a MOF with SBUs containing unsaturated Mn(II) sites.²¹ As shown in Fig.4-1, three framework tetrazolate rings bind one Mn(II) center

on each corner of the SBU to form an isolated, tripodal Mn(II) site. Balancing the overall charge of CPF-5 indicates that these Mn(II) sites possess no net charge, indicating that the framework acts as a dianionic ‘ligand’ to the Mn(II) ion. To the best of our knowledge, this dianionic ligand environment is distinct when compared to related tris(pyrazolyl)methane (Tpm, neutral) and tris(pyrazolyl)borate (Tp, monoanionic) ligands.^{8, 17, 22} Being charge neutral, the vacant coordination sites on the Mn(II) center in CPF-5 are capped by three water molecules (Figure 4-1). The bound water molecules can be exchanged by solvents, such as acetonitrile, or substrates for achieving catalysis. Importantly, because these Mn(II) sites are immobilized within the MOF, steric protection is not required to avoid catalyst dimerization, decomposition, etc., making substrate access, binding, and turnover facile.

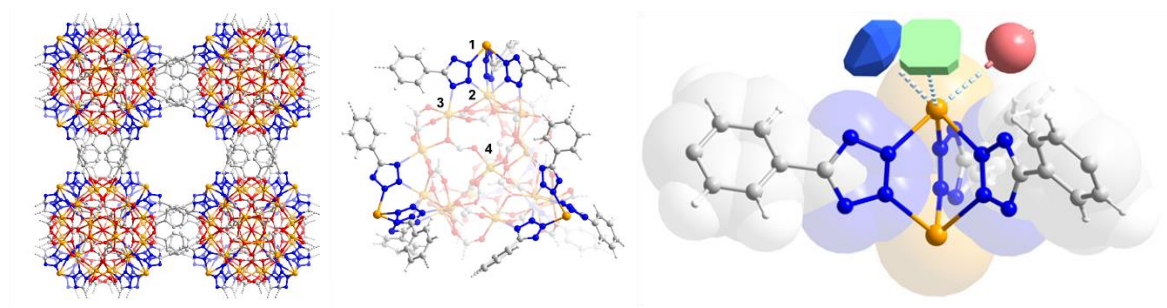
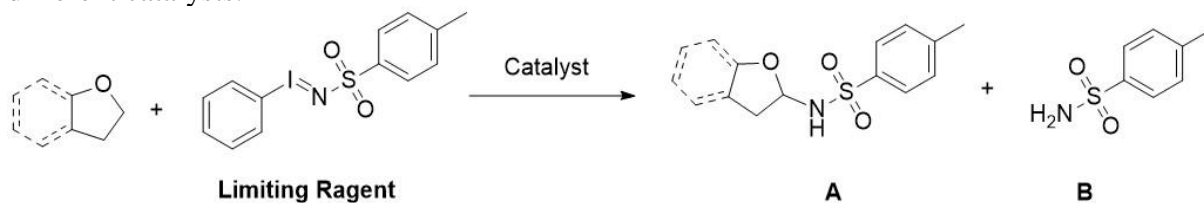


Figure 4-1 The structures of CPF-5 and composition of its SBUs. The CPF-5 contains complex SBUs, but results in large 13.6 Å pores (*left*). The SBUs contain four crystallographic independent Mn(II) ions (*middle*, labeled as Mn1-4), with the tripodal active (position 1) active site highlighted in brighter colors. The facially coordinated Mn(II) in CPF-5 possesses open coordination sites for substrate binding (*right*, depicted as different colored shapes). Mn, orange; C, gray; H, white; N, blue; O, red; Cl, green.

To demonstrate the viability of CPF-5 as a catalyst for intermolecular C–H amination, we treated CPF-5 with the nitrene precursor phenyl-*N*-tosyliodinane (PhI=NTs, 1 equiv) in acetonitrile solution with THF as a substrate (1.0 equiv). The MOF catalyst was used in 1.0 mol% (based on tripodal Mn(II) sites) relative to PhI=NTs. After 30 min at room temperature, ¹H NMR (Figure 4-8) and gas chromatography-mass spectrometry (GC-MS) analysis revealed

85% yield of THF to the α -amination product *N*-(tetrahydro-2-furanyl)-4-toluenesulfonamide (Figure 4-2, Table 4-1). The yield is based on the productive transfer of PhI=NTs to form the α -amination product^{8, 17} with a 1:1 stoichiometry of PhI=NTs to THF. CPF-5 after catalysis was proved to be intact by PXRD (Figure 4-6) and N₂ gas sorption (Figure 4-7). To test the heterogeneity of CPF-5, a hot filtration experiment was conducted after 30 min of catalysis, after which no further conversion of substrate was observed. In addition, ICP-MS shows that the concentration of Mn ion was <5 ppb in the filtered solution, indicating no significant Mn leaching during the reaction. By comparison, similar molecular, homogeneous Mn(II) complexes require 5 mol% catalyst to produce between 32-38% yield of the amination product after 1 h under similar conditions and generally require a large excess of organic substrate to achieve efficient nitrene transfer.⁸ As rudimentary control reactions, a variety of Mn(II) and Mn(III) salts, as well as several other MOFs, were examined, but none yielded the desired product under identical conditions (Table 4-1).

Table 4-1 Amination of tetrahydrofuran (THF) or 2,3-dihydrobenzofuran (BzTHF) with different catalysts.



Entry	Substrate	Catalyst	Time (h)	Yield [†] (%)	
				A	B
1	THF	CPF-5	0.5	85(±3)	15(±3)
2	THF	Mn ^{III} (acac) ₃	12	None	None
3	THF	Mn ^{II} CO ₃	12	None	None
4	THF	Mn ^{II} (OAc) ₂	12	None	None
5	THF	Mn ^{II} Cl ₂	12	Trace	99
6	THF	CPF-5 supernatant [‡]	12	None	None
7	THF	UiO-66(Zr)	12	None	None
8	THF	ZIF-8(Zn)	12	None	None
9	THF	ZIF-67(Co)	12	None	None
10	BzTHF	CPF-5	0.25	98(±2)	Trace
11	BzTHF	Mn ^{III} (acac) ₃	12	None	None
12	BzTHF	Mn ^{II} CO ₃	12	None	None
13	BzTHF	Mn ^{II} (OAc) ₂	12	None	None
14	BzTHF	Mn ^{II} Cl ₂	12	None	100

Conversion was calculated based on PhINTs. [†]Isolated yield was calculated based on ¹H NMR peak integration ratio between the amination product (A) and tosylamide (B). [‡]Supernatant solution obtained post-catalysis from CPF-5; no yield shows that the catalysis observed with CPF-5 is attributable to the MOF and not due to a soluble species.

To explore the catalytic scope of CPF-5, we examined its reactivity with a variety of substrates (Figure. 4-2). Secondary benzylic C–H substrates, such as 1,3-dihydroisobenzofuran (BzTHF) resulted in near quantitative conversion of PhI=NTs to the expected amination

products (Figure 4-9). 2-Methyl-tetrahydrofuran (2-MeTHF) resulted in selective amination at 2° C–H bond (73% yield), thereby showing a preference for less sterically hindered sites. Similarly, less sterically hindered product was more favored when employing 3-methyl-tetrahydrofuran (3-MeTHF) as the substrate, even though two isomers of products were obtained (Figure 4-10). The overall yield of 3-MeTHF amination products is ~65%, with 36% selectivity for the 2-substituted amination product (Figure 4-2) and 64% selectivity for 5-substituted product. Treatment of weaker Lewis basic cycloether substrates, such as tetrahydropyran (THP) afforded the α -aminated product in ~50% yield. 3,4-Dihydro-2H-pyran (DHP) resulted in 56% yield of amination product (Figure 4-11). However, more reactive substrates, such as and 3,4-dihydro-1*H*-2-benzopyran (BzTHP) and dioxane (performed neat) gave the desired amination products in >90% yield (Figure 4-2). Amination of nitrogen and sulfur heterocycles was also examined, but the PhI=NTs reagent dissolved immediately upon addition of these substrates, even in the absence of catalysis, suggesting a rapid reaction between the substrates and PhI=NTs (potentially oxidation into imines or sulfilimide). However, C–H activation was achieved with dibenzyl-methyl-amine (DBMA), where the methylaminated product was formed in 35% yield. Consistent with the amination of 2-MeTHF, the product obtained also suggests the sterically less hindered methyl C–H bond is favored for activation.

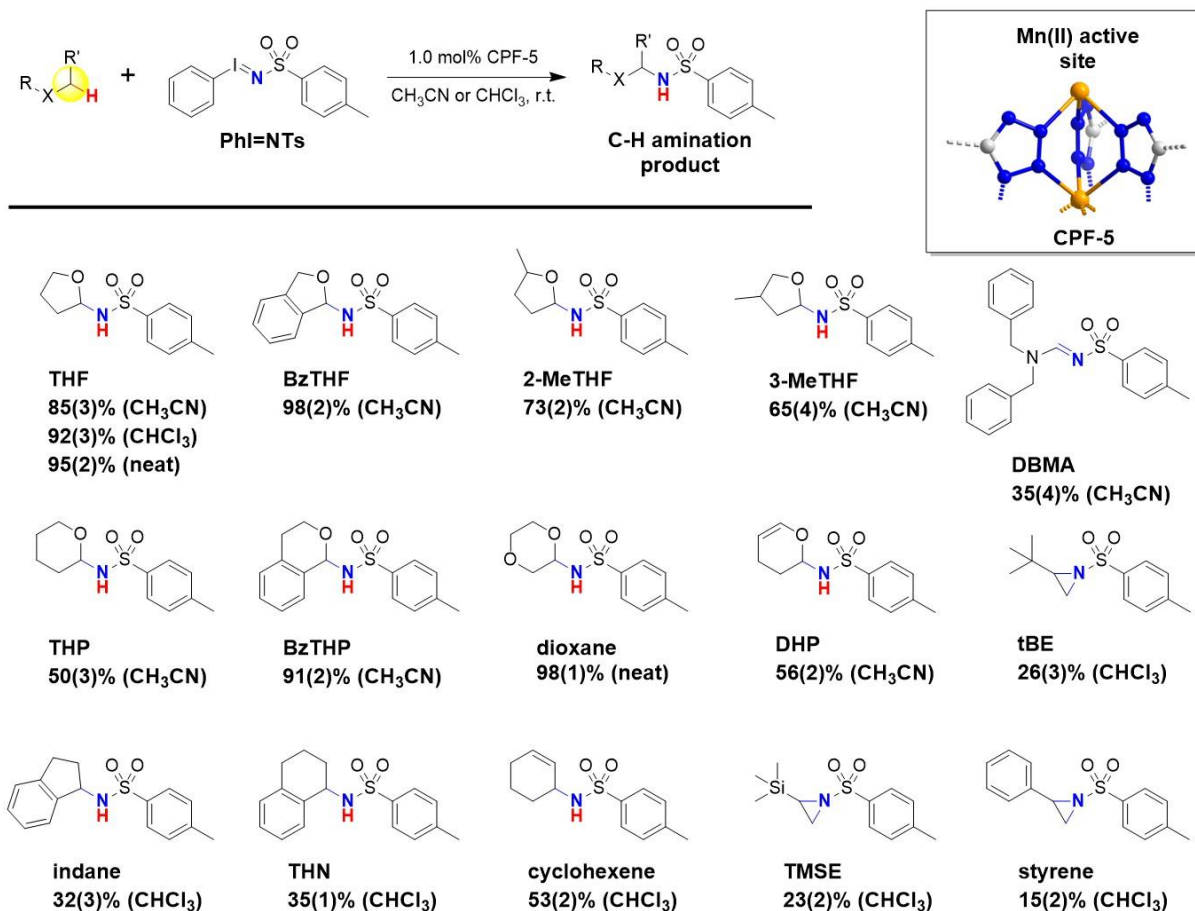


Figure 4-2 Reaction scheme and substrate scope for C–H amination by CPF-5. Yield for 3-MeTHF is the combined yield of two isomers. Isolated yields are shown under each amination product with the solvent system indicated.

CPF-5 can aminate non-coordinating substrates in lower yields, but requires longer reaction times (6 h) and a non-coordinating solvent (CHCl₃ instead of acetonitrile used above).⁸ Using CHCl₃, the benzylic hydrogens of indane and 1,2,3,4-tetrahydronaphthalene (THN) could be aminated in 32% and 35% yield. Similarly, cyclohexene is selectively aminated at the allylic position in 53% yield (Figure 4-12). This is notable, as many molecular C–H amination catalysts based on reactive metal-nitrene species effect both aziridination and C–H amination with olefin substrates.⁸ CPF-5 is capable of olefin aziridination when relatively weak C–H bonds are absent in the substrate, e.g. *t*-butylethylene (tBE, Figure 4-13), trimethylsilylethylene

(TMSE), and styrene, all of which can be converted by CPF-5 to the corresponding aziridines in modest yields (Figure 4-2). However, conversion of benzene or toluene were unsuccessful, suggesting a C–H bond dissociation energy threshold required for productive amination with CPF-5.

Despite the limited substrate scope, the catalytic activity of CPF-5 is most remarkable with respect to catalyst longevity and turnover with coordinating substrates. In this respect, CPF-5 serves as a prototype for site immobilization and isolation of a molecular type species capable of carrying out a difficult, multielectron transformation with high efficiency. To demonstrate catalyst activity and stability, a large-scale reaction involving 50 g of PhI=NTs (1.0 equiv), 24 g of BzTHF (1.5 equiv), and ~1.0 mg of CPF-5 catalyst ($\sim 7 \times 10^{-4}$ mol% of active sites) was performed. Remarkably, the PhI=NTs nitrene precursor was fully consumed after ~2.5 h and 34 g (89% yield) of the desired amination product was recovered. This corresponds to a TON of ~120,000 and turnover frequency (TOF) of $\sim 48,000 \text{ h}^{-1}$. The CPF-5 crystals remained highly active even after this large-scale reaction and could be recovered and reused. These observations suggest that CPF-5 can be regarded as an immortal-like C–H amination catalyst in a manner consistent with some polymerization systems.²³ Compared to many homogeneous C–H activation catalysts, the TON obtained for CPF-5 is 3- to 4-orders of magnitude greater.^{17, 24-26} In addition, CPF-5 outperformed previously reported MOF-based C–H amination catalysts, which only show a 3- to 5-fold improvement in TON¹⁴⁻¹⁵ or TOF¹⁸ when compared to their homogeneous analogues. Indeed, the TON for the amination of BzTHF exceeds that measured in this large-scale experiment, as turnover was limited by the quantity of PhI=NTs available. This suggested to us that with lower yielding substrates, greater product generation could be achieved by continued addition of PhI=NTs. Indeed, when the reaction

between cyclohexene and PhI=NTs stalled at lower conversions (Figure 4-2), successive additions of PhI=NTs continued to drive formation of the amination product (Figure 4-14). To the best of our knowledge, CPF-5 demonstrates record high TON and TOF for a C–H amination catalyst that is unmatched by any other homogenous or heterogeneous catalysts.

To further demonstrate the immortal nature of C–H amination catalysis by CPF-5, a series of experiments involving tandem reactions was performed. Using THF as a substrate, GC-MS was used to monitor product formation (Figure 4-3). In the first experiment, amination of THF with 100 mg of PhI=NTs was completed (~90% yield based on consumption of PhI=NTs) using 1.0 mg of CPF-5 in ~10 min. The reaction mixture was stirred for an additional 20 min, after which another aliquot of THF and PhI=NTs was added. This was repeated four times using the same 1.0 mg of CPF-5 catalyst, with no loss in catalytic activity (Figure 4-3 *top left*). Continuous catalytic activity was observed even when the dwell time between addition of substrate was extended from 20 min to one day (Figure 4-3 *top right*). Similarly, catalytic activity was maintained when different substrates were added to the reaction mixture (THP and THF, Figure 4-3 *bottom left*). Finally, upon catalytic amination of THF with PhI=NTs (for ~20 min), the liquid phase was removed and the same CPF-5 crystals were exposed to fresh THF and PhI=NTs in acetonitrile. Amination of THF dropped slightly with each fresh addition of substrate (Figure 4-3 *bottom right*), perhaps due to the introduction of water during catalyst isolation,⁸ but could be fully recovered by the addition of molecular sieves to the reaction mixture. Similar experiments were carried out with BzTHF and BzTHP, which gave >90% yield over 20 reaction cycles (Figure 4-14), while leaving the CPF-5 single-crystals intact (Table 4-3). Taken together, these experiments further support our conclusion that CPF-5 is a reusable, immortal C–H amination catalyst.¹⁴ It is also notable that CPF-5 does not show any

apparent product inhibition, which may be due to the formation of a high-spin Mn(II) species that are known to exhibit fast ligand dissociation kinetics.²⁷

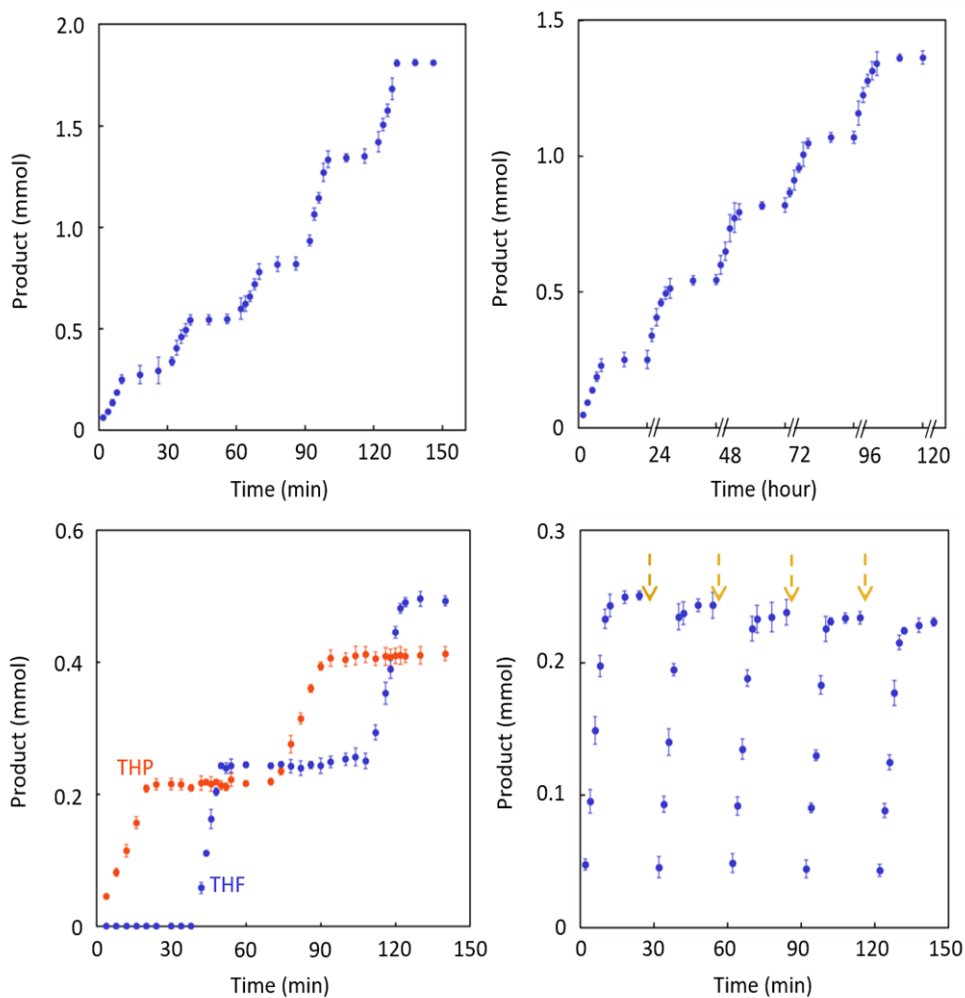


Figure 4-3 Evidence for CPF-5 as an immortal C–H amination catalyst. Using 1.0 mg of CPF-5: (*top left*) Addition of PhI=NTs and THF resulted in conversion to the desired amination product after ~10 min, which could be replicated by addition of fresh reactants added in 30 min intervals (in last two runs, the quantity of reactants was doubled); (*top right*) The same experiment as performed in ‘A’ but with the addition of fresh reactants every 24 h; (*bottom left*) The use of two different substrates, THP (red) and THF (blue) did not impact the activity of the catalyst; (*bottom right*) The CPF-5 catalyst was isolated between additions of fresh reactant in 25 min intervals, showing essentially no change in reaction rate. Arrows indicate the removal of reaction mixture.

4.3 Mechanism Study

An initial examination of the catalytic mechanism was performed using the isotope effect on C–H amination between THF and THF-*d*₈. Measurement of rate constants for product formation from parallel THF/THF-*d*₈ amination reactions resulted in a $k_{\text{H}}/k_{\text{D}} = 4.5(2)$ (Figure 4-16). A similar value was obtained ($k_{\text{H}}/k_{\text{D}} = 4.6(1)$) when competitive amination of a 1:1 mixture of THF/THF-*d*₈ was conducted (Figure 4-4 A). These isotope effect results indicate that C–H bond cleavage is the critical initial step in the product formation process (Figure 4-4 B).²⁸ The isotope effect for intermolecular C–H amination by CPF-5 is lower than some Fe-nitrene systems that function by a hydrogen-atom abstraction/radical rebound pathway,^{7, 25} but are comparable to other Mn-,²⁶ Cu-,²⁹ and Ru-nitrene³⁰⁻³¹ systems that have been proposed to operate similarly. Notably, the preferential C–H amination, rather than aziridination, of cyclohexene by CPF-5 mirrors the chemoselectivity of other Mn- and Fe-based amination catalysts where reactive metal-nitrene species are proposed as the catalytically relevant intermediates.^{26, 32}

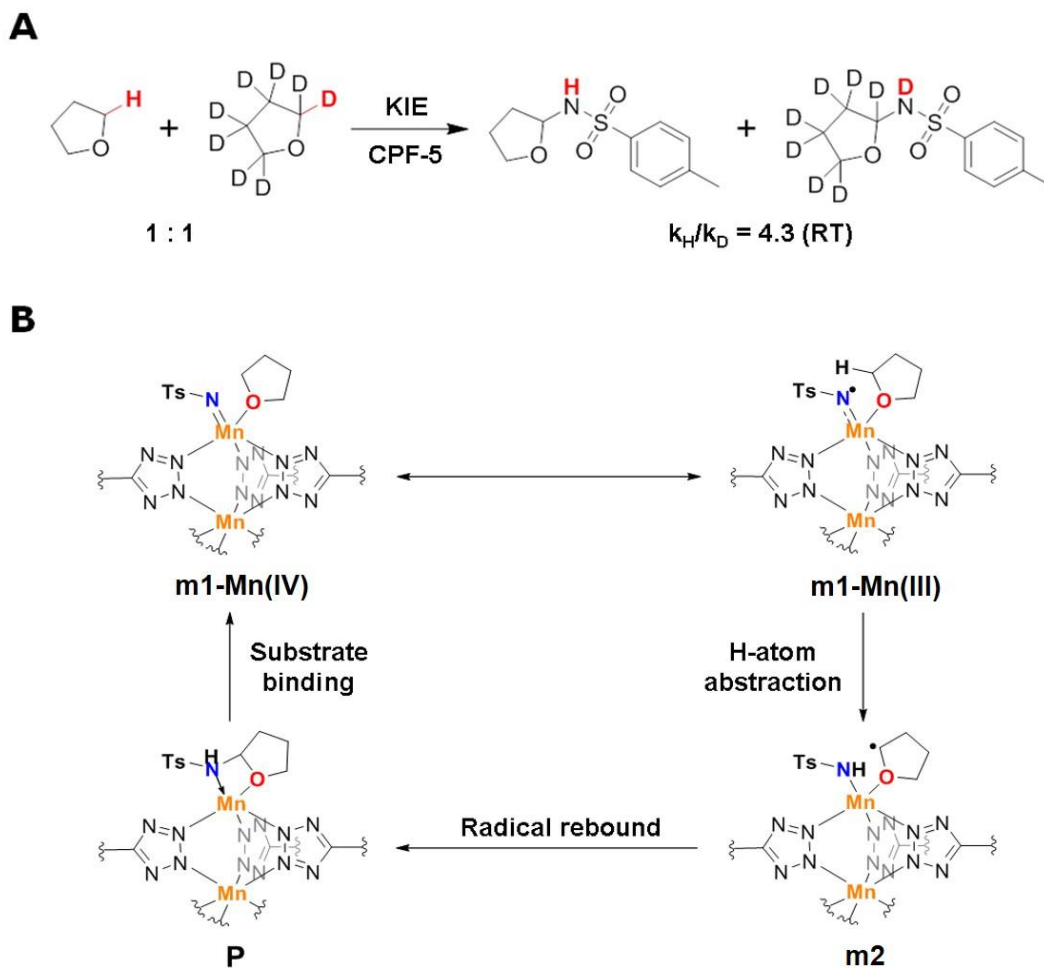


Figure 4-4 Schematic illustration of C-H amination mechanism. (A) KIE values for intramolecular competition experiments with CPF-5 were obtained from quantitative ^1H NMR spectroscopy. (B) Nonunity KIE value suggests CPF-5 amination catalysis proceeds via a transition structure where C–H bond breakage occurs followed by a radical rebound.

While attempts to observe an intermediate species upon the addition of $\text{PhI}=\text{NTs}$ to CPF-5 in the absence of substrate were not successful, density functional theory (DFT) calculations indicate that a substrate-accessible Mn-nitrene species is a feasible intermediate for this system. Using a heterodinuclear Mn/Zn tetrazolate cation $[\text{Zn}(\text{OH}_2)_3(\text{MeTet})\text{Mn}]^+$ (MeTet = 5-methyl-tetrazolate) as a model platform, the Mn-nitrene THF adduct

$[\text{Zn}(\text{OH}_2)_3(\text{MeTet})\text{Mn}(\text{NTs})(\text{THF})]^+$ (**m1**; m = model) was found to optimize to a reasonable uncongested, trigonal bipyramidal geometry (Figure 4-17). Broken-symmetry DFT calculations³³ on model **m1** indicated that electronic states representing a Mn(IV)-imido ($\text{Mn}^{\text{IV}}=\text{NR}$) and an anti-ferromagnetically coupled Mn(III)-bound aminyl radical ($\text{Mn}^{\text{III}}-(\text{N}\cdot)\text{R}$) are nearly isoenergetic. Notably, metal-bound aminyl radicals have been previously shown to be competent for C–H bond amination catalysis through a hydrogen-atom abstraction/radical rebound mechanism.^{7, 25, 32} Calculations on the putative THF-radical intermediate, $[\text{Zn}(\text{OH}_2)_3(\text{MeTet})\text{Mn}(\text{N}(\text{H})\text{Ts})(\text{THF})]^+$ (**m2**), in which an α -hydrogen atom is transferred to the Mn-nitrene unit, converged to a minimum lying only 6.0 kcal/mol higher in energy than **m1** (Figure 4-18). This enthalpic difference indicates that a hydrogen-atom abstraction pathway for product formation is energetically surmountable for coordinating substrates such as THF. Whereas the intermediacy of a simple Mn-iminoiodane adduct (i.e. $\text{Mn}\leftarrow\text{RI}=\text{NR}'$) capable nitrene transfer cannot be ruled out,³⁴⁻³⁵ especially for the aziridination of olefin substrates lacking allylic C–H bonds, the similar chemoselectivity and kinetic isotope data to other C–H amination catalysts systems suggest that the tripodal Mn(tetrazolate)₃ sites of CPF-5 can form an active metal-nitrene species.²⁶

4.4 PSE of CPF-5

In order to improve the catalytic activity of CPF-5 and extend the scope of catalytic organic reactions³⁶, we tried to exchange Mn with Fe and Co in CPF-5 on position 1 (Figure 4-1). Anhydrous metal salts and solvents were used for PSE experiments because excessive water has proven to destroy the crystals in previous sections. First, PSE of CPF-5 with Co or Fe was found to be solvent-dependent. PSE on CPF-5 with CoCl_2 in acetonitrile gave highest exchange

ratio when maintaining the single crystallinity, while other solvents like DMF, DCM, THF and methanol resulted in either lower exchange ratio or poor crystallinity (Table 4-2, Entry 3, 5 and 6). However, attempts to solve the structure of CPF-5(M) (exchanged CPF-5 with M, M= Co or Fe) using single-crystal XRD data were unsuccessful because of close electron densities between metal Mn, Fe, Co. Second, more Co can be incorporated into CPF-5 when increasing the ratio of CoCl₂ and reaction time used for PSE (Table 4-2, Entry 1-3). Co/Mn ratio of CPF-5(Co) was found to be 25.7% after 48h (Table 4-2, Entry 4), which almost equals the ratio of position 1 Mn (4 atoms) to overall Mn (21 atoms) in CPF-5 SBUs (Figure 4-1). Similarly, more Fe was incorporated into CPF-5(Fe) when increasing the amount of Fe salt and reaction time (Table 4-2, Entry 9 and 10). PSE with Fe(III) salts, including FeCl₃ and Fe(SO₃CF₃)₃, resulted in the formation of amorphous precipitate.

Table 4-2 PSE of CPF with Co and Fe under different reaction conditions.

Entry	Metal Source	Solvent	T and t	Crystallinity	M/Mn
1	CoCl ₂ , 0.5 eq	CH ₃ CN	60 °C, 24 h	+	8.7%
2	CoCl ₂ , 1.0 eq	CH ₃ CN	60 °C, 24 h	+	17.2%
3	CoCl ₂ , 2.5 eq	CH ₃ CN	60 °C, 24 h	+	24.0%
4	CoCl ₂ , 2.5 eq	CH ₃ CN	60 °C, 48 h	+	25.7%
5	CoCl ₂ , 2.5 eq	DMF	60 °C, 24 h	+	4.0%
6	CoCl ₂ , 2.5 eq	CH ₃ OH	60 °C, 24 h	-	N/A
7	CoCl ₂ , 10 eq	CH ₃ CN	60 °C, 6d	-	N/A
8	CoCl ₂ , 10 eq	DMF	120 °C, 24h	-	N/A
9	Fe(SO ₃ CF ₃) ₂ , 1 eq	CH ₃ CN	60 °C, 24 h	+	4.6%
10	Fe(SO ₃ CF ₃) ₂ , 2 eq	CH ₃ CN	60 °C, 48 h	+	9.4%

Reaction conditions: 20 mg CPF-5 was used with 2 mL solvent for PSE, it contains 0.02 mmol Mn active site 1 in the original MOF. Exchanged CPF-5 maintaining single crystallinity is denoted as “+” in crystallinity column, otherwise denoted as “-”. M/Mn ratio of exchanged CPF-5 was monitored by ICP-MS after MOF digestion in HNO₃. PSE with Fe(SO₃CF₃)₂ was conducted under N₂ atmosphere.

In order to confirm the replacement of Mn by Co or Fe, the amount of Mn in the PSE supernatant solution was tested by ICP-MS (Figure 4-5). After PSE with Co for 1 day (Table 4-2, Entry 3), 0.49 mg of Co was exchanged into 10 mg CPF-5(Co), while only 0.20 mg of Mn was observed in the supernatant solution. It shows that 41% Co, with respect to all Co detected in CPF-5(Co) (24.0% Co/Mn), was actually replacing Mn atoms in MOF SBUs while other Co ions may be adsorbed to the surface of MOF. 2-day PSE with Co resulted in 0.54 mg of Co exchanged into CPF-5(Co) and 0.32 mg of Mn out of CPF-5(Co), showing 59% Co for actual PSE. Although Fe exchange for 1 d resulted in lower M/Mn ratio in CPF-5(Fe) compared to Co exchange (Table 4-2, Entry 2 and 9), it shows higher PSE ratio among the incorporated Fe with

almost same amount of metals detected in MOF (65 μg) and supernatant solution (69 μg) (Figure 4-5). Addition of much excessive metal salts was demonstrated to achieve efficient PSE for MFU-4l.^{19, 37} However, for CPF-5, aggressive PSE conditions destroyed MOF crystallinity by producing amorphous solid materials (Table 4-2, Entry 7) or completely dissolving MOFs (Table 4-2, Entry 8).

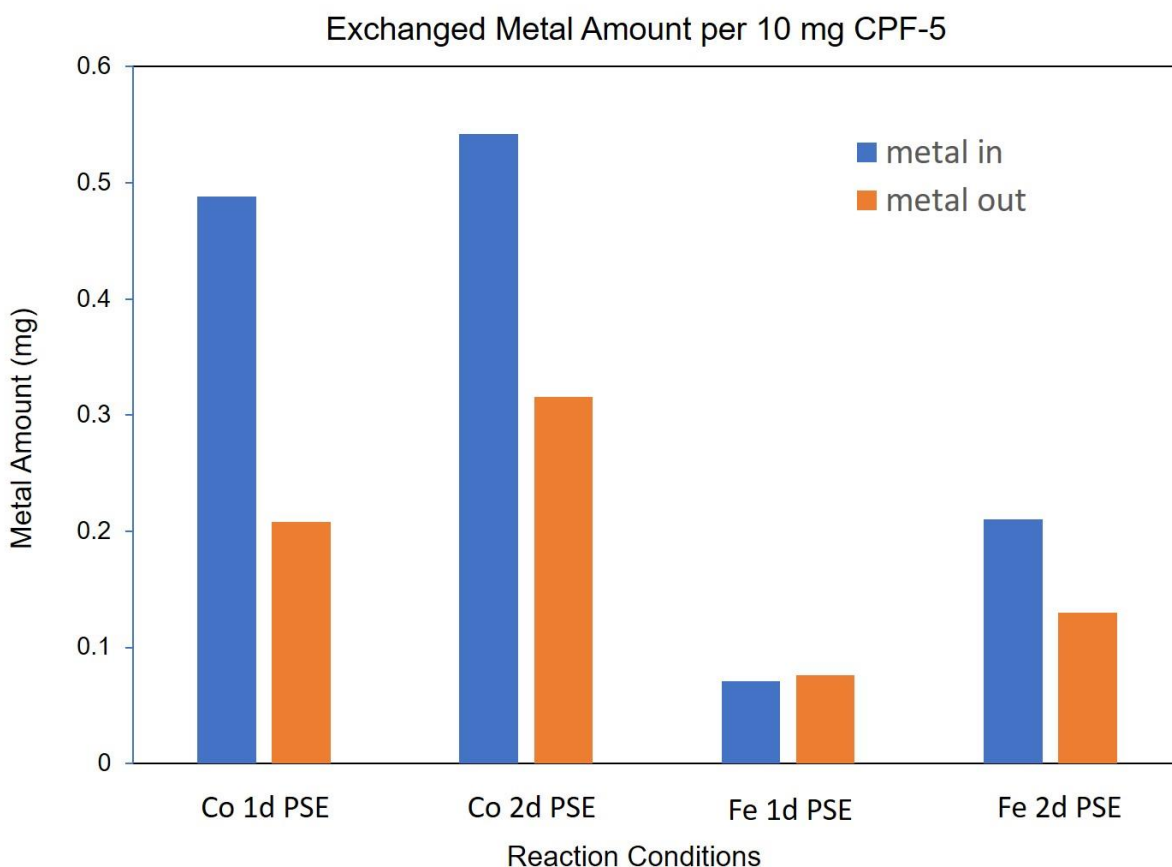


Figure 4-5 Metal exchanged in and out CPF-5 with Co and Fe.

4.5 Conclusion

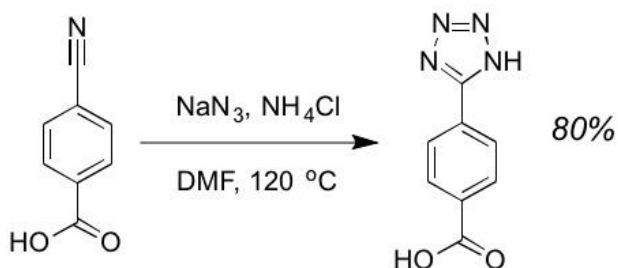
The unprecedented activity of CPF-5 is attributed to a combination of effects, including site isolation of the dianionic, facial coordinating, sterically unencumbered active site.^{21, 38} In addition, unlike homogenous molecular species or flexible MOFs,³⁹⁻⁴⁰ the highly

interconnected metal clusters in CPF-5 result in a rigid framework that may inhibits dynamic, stabilize reactive centers, and isolate these centers. Although the substrate scope of CPF-5 is rather limited, it is also known that tripodal Mn complexes are inferior to their Fe analogues for C–H amination.⁸ Therefore, we also modified CPF-5 by postsynthetic ion exchange to produce highly active catalysts with a broader utility. Nevertheless, CPF-5 achieves unprecedented activity in Mn catalyzed C–H amination and represents the first example of a C–H amination catalyst with immortal-like characteristics.

4.6 Experimental

General Methods. All manipulations of activated metal-organic frameworks (MOFs) were carried out in the absence of water and oxygen using standard Schlenk techniques or in an MBraun inert atmosphere glovebox. All glassware was oven dried for a minimum of 1 h and cooled in an evacuated antechamber prior to use in the glovebox. Acetonitrile, benzene, and tetrahydrofuran purchased from Sigma Aldrich were dried and deoxygenated using standard procedures, then stored over 4 Å molecular sieves prior to use. Dimethylformaldehyde (DMF) were purchased from VWR and used as received. CDCl₃ was purchased from Cambridge Isotope Labs and used as received. Diacetolalyl-iodobenzene, tosylamide, methanol, manganese(II) chloride tetrahydrate, 4-cyano-benzoic acid and ammonium formate were purchased from Sigma Aldrich and used as received. Ammonium chloride was purchased from Alfa Aesar and used as received. Organic substrates including were purchased from Sigma Aldrich and dried over 4 Å molecular sieves for more than 48 h prior to use. Chromatography purification was performed on Teledyne ISCO Combiflash Rf+ PurIon auto-column system. Ligand and MOF syntheses were carried out in air. ¹H and ¹³C NMR were recorded on Varian

Mercury 400 MHz or Varian Unity/Inova 500 MHz spectrometers. ^1H and ^{13}C NMR chemical shifts are reported relative to SiMe_4 using the chemical shift of residual solvent peaks as reference.



Synthesis of 4-(Tetrazol-5-yl)benzoic acid (*H₂tzca*). 4-(Tetrazol-5-yl)benzoic acid was synthesized using a previously reported method with minor modifications (*Chemistry of Materials*, **2011**, 23, 2908-2916). 4-Cyanobenzoic acid (14.7 g, 100 mmol), ammonium chloride (5.9 g, 110 mmol), and sodium azide (7.2 g, 110 mmol) were heated to $120\text{ }^\circ\text{C}$ in 100 g of DMF for 24 h. After heating, 1 M HCl was added until the solution was acidic (pH \sim 2 as indicated by pH paper). The desired product precipitated as a white solid, which was collected by vacuum filtration, and dried in an oven at $120\text{ }^\circ\text{C}$ for 12 h. Yield: 17.1 g (80%). ^1H NMR (400 MHz, CDCl_3): δ 7.98 (d, 2H), 8.10 (d, 2H). ATR-FTIR (cm^{-1}): 3485 (w), 3360 (w), 1687 (s), 1575 (w), 1436 (w), 1323 (w), 1286 (w), 1091 (w), 995 (w).

Synthesis of CPF-5. Single-crystals of CPF-5 were synthesized as previously reported (*Chem. Commun.* **2012**, 48, 7498-7500). Upon formation of crystals using the reported procedure, the warm reaction solution was immediately removed by filtration to prevent the formation of amorphous precipitates as the reaction mixture cooled. The recovered crystals were washed with $3 \times 3.0\text{ mL}$ of MeOH to remove any excess starting materials. Then $5 \times 3.0\text{ mL}$ of dry CH_3CN was used to wash CPF-5 crystals to remove the MeOH. CPF-5 crystals were

placed in 5.0 mL of dry CH₃CN inside 24-mL glass vials sealed with a rubber septum. The vials were flushed with nitrogen gas and held under a nitrogen atmosphere at 70 ° C. After 24 h, the CH₃CN was removed with an airtight syringe and replaced with fresh dry CH₃CN (5.0 mL). The vial was again flushed with nitrogen gas and held under a nitrogen atmosphere at 70 ° C for 24 h. This process was repeated a total of five times, after which the activated CPF-5 crystals were dried under vacuum and stored in a glovebox.

PSE of CPF-5. 20 mg CPF-5 (0.02 mmol) was incubated in solutions containing different equivalent CoCl₂ or Fe(SO₃CF₃)₂ for different time (1 d or 2 d). Addition of Fe(SO₃CF₃)₂ was conducted in a N₂ glovebox. Exchanged CPF-5 was washed with 15 mL CH₃CN for three times and soaked in CH₃CN at 60 °C for 3 days to remove excessive metal salts. During incubation, fresh CH₃CN was exchanged every 24h. The washed solvents were combined together with PSE supernatant solution for ICP-MS to test the amount of Mn ions out of MOF. The obtained CPF-5(M) (M = Co or Fe) was stored in CH₃CN for further analysis.

Synthesis of [N-(p-Toluenesulfonylimino)]phenyliodinane (PhI=NTs). [N-(p-Toluenesulfonylimino)]phenyliodinane was synthesized using literature methods (*Chem. Lett.* **1975**, *4*, 361-362). Potassium hydroxide (14.0 g, 250 mmol) was dissolved in 400 mL of MeOH cooled in an ice-water bath. To this solution was added *p*-toluenesulfonamide (17.1 g, 100 mmol) giving a clear solution. To this solution was added diacetolatoiodobenzene (32.2 g, 100 mmol) resulting in a yellow solution. The reaction mixture was then allowed to warm to room temperature at which it was left to stir for 3 h. The reaction mixture was poured into 1.4 L of water that was placed in an ice bath, resulting in precipitation of a pale yellow solid upon standing overnight. The crude product was isolated by vacuum filtration and then washed with 2×80 mL of ice cold water, suspended in ~160 mL of cold MeOH, briefly stirred, and then re-

isolated by vacuum filtration and dried under vacuum to give the product as a pale yellow powder. Caution: No heat should be applied during product drying, as temperatures $>90^{\circ}\text{C}$ can result in explosive decomposition. Yield: 24.2 g (65%). ^1H NMR (400 MHz, $\text{DMSO-}d_6$): δ 2.42 (s, 3 H), 7.26-8.13 (m, 9 H).

General Catalytic Procedure for Heteroatom Substrates. Under an inert nitrogen atmosphere, CPF-5 (4.0 mg, 0.004 mmol active sites, 1 mol%) and PhI=NTs (150 mg, 0.40 mmol, 1.0 equiv) were placed into a 24 mL scintillation vial, followed by the addition of 0.40 mmol (1.0 equiv) of the organic heteroatom substrate in 5.0 mL of dry CH_3CN . Reaction mixtures were held at room temperature with gentle agitation using a shaker bed. After 30 min, the PhI=NTs in the initial suspension had dissolved to give a transparent, pale yellow solution. The solution was then concentrated under vacuum to dryness. The resulting residue was dissolved in 1.0 mL of CH_2Cl_2 , loaded onto a pre-packed silica gel column, and isolated by flash chromatography using a 0 \rightarrow 20% gradient of ethylacetate in hexanes as the eluent. Yields for the isolated products are based on the productive nitrene transfer from PhI=NTs and are based on at least three independent experiments.

For amination product of THF. Yield: $85\pm 3\%$. ^1H NMR (400 MHz, CDCl_3): δ 7.80 (d, $J = 8.3$ Hz, 2H), 7.27 (d, $J = 8.3$ Hz, 2H), 5.74 (d, $J = 8.8$ Hz, 1H), 5.38-5.28 (m, 1H), 3.77-3.59 (m, 2H), 2.41 (s, 3H), 2.22 – 2.05 (m, 1H), 1.93 – 1.72 (m, 3H). ^{13}C NMR (100 MHz, CDCl_3): δ 143.5, 138.8, 129.7, 127.3, 85.2, 67.4, 32.8, 24.2, 21.8. ESI-MS Calculated for $[\text{C}_{11}\text{H}_{15}\text{NNaO}_3\text{S}]^+$ (m/z): 264.07; Found: 264.07.

For amination product of BzTHF. Yield: $98\pm 2\%$. ^1H NMR (400 MHz, CDCl_3): δ 7.84 (d, $J = 8.2$ Hz, 2H), 7.32-7.30 (m, 6H), 6.52 (d, $J = 8.5$ Hz, 1H), 5.39 (d, $J = 10.1$ Hz, 1H), 4.98 (dd, $J = 12.6$ Hz, 12.6 Hz, 2H), 2.44 (s, 3H). ^{13}C NMR (100 MHz, CDCl_3): δ 143.7, 139.5,

138.8, 136.8, 129.8, 129.7, 128.3, 127.4, 123.2, 121.4, 89.1, 72.2, 35.4, 21.8. ESI-MS Calculated for $[\text{C}_{15}\text{H}_{15}\text{NNaO}_3\text{S}]^+$ (m/z): 312.07; Found: 312.08.

For amination product of 2-MeTHF. Yield: 73±2%. ^1H NMR (400 MHz, CDCl_3): δ 7.80 (d, $J = 8.3$ Hz, 2H), 7.28 (d, $J = 8.3$ Hz, 2H), 5.56 (d, $J = 8.7$ Hz, 1H), 5.48-5.33 (m, 1H), 5.25-5.06 (m, 1H), 3.93 (m, 1H), 2.41 (s, 3H), 2.29 – 2.23 (m, 1H), 2.23-1.88 (m, 4H). ^{13}C NMR (100 MHz, CDCl_3): δ 143.3, 138.3, 129.7, 129.4, 85.0, 74.3, 33.3, 31.6, 21.8, 20.7. ESI-MS Calculated for $[\text{C}_{12}\text{H}_{17}\text{NNaO}_3\text{S}]^+$ (m/z): 278.08; Found: 278.10.

For amination product of THP. Yield: 50±3%. ^1H NMR (400 MHz, CDCl_3): δ 7.79 (d, $J = 8.3$ Hz, 2H), 7.27 (d, $J = 8.3$ Hz, 2H), 5.20 (d, $J = 9.7$ Hz, 1H), 4.75 (td, $J = 9.4, 2.4$ Hz, 1H), 3.77-3.67 (m, 1H), 3.43-3.33 (m, 1H), 2.41 (s, 3H), 1.88-1.51 (m, 6H). ^{13}C NMR (125 MHz, CDCl_3): δ 129.3, 127.1, 82.1, 66.3, 31.9, 24.6, 22.4, 21.5. ESI-MS Calculated for $[\text{C}_{12}\text{H}_{17}\text{NNaO}_3\text{S}]^+$ (m/z): 278.08; Found: 278.12.

For amination product of BzTHP. Yield: 91±2%. ^1H NMR (400 MHz, CDCl_3): δ 7.86 (d, $J = 8.3$ Hz, 2H), 7.46-7.21 (s, 6H), 6.11 (d, $J = 8.5$ Hz, 1H), 5.39 (d, $J = 8.3$ Hz, 1H), 3.99-3.30 (m, 4H), 3.07-2.56 (m, 2H), 2.44 (s, 3H). ^{13}C NMR (100 MHz, CDCl_3): δ 129.7, 129.1, 128.7, 127.4, 127.0, 127.0, 80.1, 59.0, 27.8, 21.8. ESI-MS Calculated for $[\text{C}_{16}\text{H}_{17}\text{NNaO}_3\text{S}]^+$ (m/z): 326.08; Found: 326.12.

For amination product of DBMA. Yield: 35±4%. ^1H NMR (400 MHz, CDCl_3): δ 8.51 (s, 1H), 7.82 – 7.13 (m, 14H), 4.53 (s, 2H), 4.36 (s, 2H), 2.43 (s, 3H). ^{13}C NMR (125 MHz, CDCl_3): δ 159.7, 129.6, 129.4, 129.1, 128.9, 128.4, 128.2, 126.7, 55.3, 48.7, 21.8. ESI-MS Calculated for $[\text{C}_{22}\text{H}_{23}\text{N}_2\text{O}_2\text{S}]^+$ (m/z): 379.15; Found: 379.14.

For amination product of DHP. Yield: 56±2%. ^1H NMR (400 MHz, CDCl_3): δ 7.82 (d, $J=8.3$, 2H), 7.28 (d, $J=8.0$, 2H), 6.03 (s, 1H), 5.65 (s, 1H), 5.47 (d, $J=11.5$, 2H), 3.57 – 3.33

(m, 2H), 2.42 (s, 3H), 2.16 (s, 1H), 1.89 (s, 1H) ^{13}C NMR (125 MHz, CDCl_3): δ 143.28, 138.96, 130.38, 129.42, 127.09, 124.76, 76.77, 57.69, 24.15, 21.60. ESI-MS Calculated for $[\text{C}_{12}\text{H}_{16}\text{NO}_3\text{S}]^+$ (m/z): 254.08; Found: 254.08

For amination product of 3-Me-THF. Yield (mixture of two isomers): 65±4%. ^1H NMR (400 MHz, CDCl_3): **Isomer 1 (with blue labels in Fig. S5):** (4-methyl-N-(3-methyltetrahydrofuran-2-yl)benzenesulfonamide, 36% of two isomers): δ 7.80 (d, $J = 8.2$ Hz, 2H), 7.35 (d, $J = 8.0$ Hz, 2H), 5.39 (s, 1H), 5.36 – 5.30 (m, 1H), 3.93 – 3.58 (m, 2H), 2.42 (s, 3H), 2.29 (ddd, $J = 23.9, 15.0, 7.1$ Hz, 1H), 2.11 – 1.75 (m, 2H), 1.00 (dd, $J = 6.6, 3.0$ Hz, 3H); **Isomer 2 (with red labels in Fig. S5):** (4-methyl-N-(4-methyltetrahydrofuran-2-yl)benzenesulfonamide, 64% of two isomers): δ 7.80 (d, $J = 8.2$ Hz, 2H), 7.35 (d, $J = 8.0$ Hz, 2H), 5.25 (s, 1H), 4.83 (dd, $J = 9.5, 5.1$ Hz, 1H), 3.24 (d, $J = 15.1$ Hz, 2H), 1.60 – 1.44 (m, 1H), 1.38 – 1.17 (m, 2H), 1.07 (d, $J = 6.5$ Hz, 3H). ESI-MS Calculated for $[\text{C}_{12}\text{H}_{18}\text{NO}_3\text{S}]^+$ (m/z): 256.08; Found: 256.16

Catalytic Procedure for Dioxane. Using the reaction conditions described above and extending the reaction time to 6 h, did not result in a reaction between 1,4-dioxane and $\text{PhI}=\text{NTs}$. Therefore, the reaction was performed as described above, but using neat (5.0 mL) 1,4-dioxane as solvent. The reaction was complete within ~1 h as evidenced by the dissolution of $\text{PhI}=\text{NTs}$ to give a transparent, pale yellow solution. The solution was then concentrated under vacuum to dryness. The resulting residue was dissolved in 1.0 mL of CH_2Cl_2 , loaded onto a pre-packed silica gel column, and isolated by flash chromatography using a 0→20% gradient of ethylacetate in hexanes as the eluent. Yields for the isolated products are based on the productive nitrene transfer from $\text{PhI}=\text{NTs}$ and are based on at least three independent experiments. Yield: 98±1%. ^1H NMR (400 MHz, CDCl_3): δ 7.82 – 7.79 (m, 2H), 7.31 – 7.27

(m, 2H), 5.84 (d, 1H), 5.05 – 4.98 (m, 1H), 3.78 – 3.43 (m, 6H), 2.42 (s, 3H). ^{13}C NMR (100 MHz, CDCl_3): δ 129.7, 129.1, 128.7, 127.4, 127.0, 127.0, 80.1, 59.0, 27.8, 21.8. ESI-MS Calculated for $[\text{C}_{11}\text{H}_{16}\text{NO}_4\text{S}]^+$ (m/z): 258.08; Found: 258.24.

General Catalytic Procedure for Alkyl Substrates. Under an inert nitrogen atmosphere, CPF-5 (4.0 mg, 0.004 mmol active sites, 1 mol%) and $\text{PhI}=\text{NTs}$ (150 mg, 0.40 mmol, 1.0 equiv) were placed into a 24 mL scintillation vial, followed by the addition of 2.0 mmol (5.0 equiv) of the alkyl substrate in 5.0 mL of dry CHCl_3 . Reaction mixtures were held at room temperature with gentle agitation using a shaker bed. After 6 h, the $\text{PhI}=\text{NTs}$ in the initial suspension had dissolved to give a transparent, pale yellow solution. The solution was then concentrated under vacuum to dryness. The resulting residue was dissolved in 1.0 mL of CH_2Cl_2 , loaded onto a pre-packed silica gel column, and isolated by flash chromatography using a 0→20% gradient of ethylacetate in hexanes as the eluent. Yields for the isolated products are based on the productive nitrene transfer from $\text{PhI}=\text{NTs}$ and are based on at least three independent experiments.

For amination product of indane. Yield: 32±3%. ^1H NMR (400 MHz, CDCl_3): δ 7.83 (d, 2H), 7.34 (d, 2H), 7.13-7.10 (m, 4H), 4.81-4.80 (m, 2H), 2.89-2.85 (m, 1H), 2.77-2.71 (m, 1H), 2.45 (s, 3H), 2.32-2.30 (m, 1H), 1.76-1.71 (m, 1H). ESI-MS Calculated for $[\text{C}_{16}\text{H}_{17}\text{NNaO}_2\text{S}]^+$ (m/z): 310.09; Found: 310.20.

For amination product of THN. Yield: 35±1%. ^1H NMR (400 MHz, CDCl_3): δ 7.83 (d, 2H), 7.34 (d, 2H), 7.13-7.12 (m, 1H), 7.05-7.03 (m, 2H), 6.93 (d, 1H), 4.61 (d, 1H), 4.46 (s, 1H), 2.71 (dd, 2H), 1.83-1.38 (m, 4H). ESI-MS Calculated for $[\text{C}_{17}\text{H}_{19}\text{NNaO}_2\text{S}]^+$ (m/z): 324.10; Found: 324.33.

For amination product of cyclohexene. Yield: 53±2%. ¹H NMR (400 MHz, CDCl₃): δ 7.87 (d, 2H), 7.30 (d, 2H), 5.76 (d, 1H), 5.33 (d, 1H), 4.39 (s, 1H), 3.81 (s, 1H), 2.43 (s, 3H), 1.93-1.73 (m, 4H), 1.25 (2H). ESI-MS Calculated for [C₁₃H₁₆NO₂S]⁻ (*m/z*): 250.09; Found: 250.33.

For aziridination product of tBE. Yield: 26±3%. ¹H NMR (400 MHz, CDCl₃): δ 7.83 (d, 2H), 7.31 (d, 2H), 2.51 (m, 2H), 2.44 (s, 3H), 2.15 (d, 1H). ESI-MS Calculated for [C₁₃H₁₉NNaO₂S]⁺ (*m/z*): 276.10; Found: 276.21.

For aziridination product of TMSE. Yield: 23±2%. ¹H NMR (400 MHz, CDCl₃): δ 7.81 (d, 2H), 7.33 (d, 2H), 2.68 (d, 2H), 2.44 (s, 3H), 2.15 (d, 1H), 2.07-1.88 (m, 2H), 0.09 (s, 9H). ESI-MS Calculated for [C₁₂H₂₀NO₂SSi]⁺ (*m/z*): 270.10; Found: 270.13.

For aziridination product of styrene. Yield: 15±2%. ¹H NMR (400 MHz, CDCl₃): δ 7.85 (d, 2H), 7.34-7.21 (m, 7H), 3.78-3.76 (m, 1H), 2.97 (d, 1H), 2.43 (s, 3H), 2.42 (d, 1H). ESI-MS Calculated for [C₁₅H₁₆NO₂S]⁺ (*m/z*): 274.09; Found: 274.32.

Control Reactions with Other Potential Catalysts. Under an inert nitrogen atmosphere, possible catalysts (MnCO₃, Mn(OAc)₂, MnCl₂, Mn(acac)₃, UiO-66, ZIF-8, 0.004 mmol, 1 mol%) and PhI=NTs (150 mg, 0.40 mmol, 1.0 equiv) were placed into a 24 mL scintillation vial, followed by the addition of either THF or BzTHF substrate (4.0 mmol, 10 equiv) in 5.0 mL of dry CH₃CN. Reaction mixtures were held at room temperature with gentle agitation using a shaker bed. After 12 h, the PhI=NTs in the initial suspension had dissolved to give a transparent, pale yellow solution. The solution was then concentrated under vacuum to dryness. The resulting residue was dissolved in 1.0 mL of CH₂Cl₂, loaded onto a pre-packed silica gel column, and isolated by flash chromatography using a 0→20% gradient of ethylacetate in

hexanes as the eluent. Yields for the isolated products are based on the productive nitrene transfer from PhI=NTs.

Evidence for CPF-5 as a Living C–H Amination Catalyst. Figure 4-3A, Uninterrupted Formation of Amination Products Upon Addition of Fresh Reactants. Under an inert nitrogen atmosphere, CPF-5 (1.0 mg, 0.001 mmol active sites, 0.4 mol%) and PhI=NTs (100 mg, 0.27 mmol, 1.0 equiv) were placed into a 24 mL scintillation vial, followed by the addition of 0.024 mL (10% THF in 0.24 mL dry CH₃CN, 0.29 mmol, 1.1 equiv) of THF in 5.0 mL of dry CH₃CN. Reaction mixtures were held at room temperature with gentle agitation using a shaker bed. After 30 min, the PhI=NTs in the initial suspension had dissolved to give a transparent, pale yellow solution. An aliquot (0.05 mL) of the reaction mixture was removed using an airtight syringe and diluted with 1.0 mL of acetone for analysis at each timepoint by GC-MS (Figure 3A). The sealed reaction mixture was transferred back into a glovebox, dosed with another 100 mg (0.27 mmol, 1 equiv) of PhI=NTs and 0.024 mL of THF (10% THF in 0.24 mL dry CH₃CN, 0.29 mmol, 1.1 equiv), and the mixture was held at room temperature with gentle agitation using a shaker bed for another 30 min. This process was repeated, giving a total of three additions of 100 mg PhI=NTs (including the initial reaction), followed by two more additions of 200 mg of PhI=NTs (0.54 mmol) and 0.049 mL of THF (10% THF in 0.49 mL dry CH₃CN, 0.59 mmol, 1.1 equiv). The formation of product was quantified from each aliquot removed by using GC-MS with toluene as internal standard. This experiment was performed in triplicate on a single CPF-5 sample.

Figure 4-3B, Uninterrupted Formation of Amination Products with Long Resting Times. The same procedure was used as described above, with the only difference being that the reaction was kept at room temperature for 24 h between additions of fresh substrate. Fresh

reactants, 100 mg of PhI=NTs and 0.023 mL of THF (10% THF in 0.23 mL dry CH₃CN, 0.27 mmol, 1.0 equiv), were added a total of five times (including the initial reaction). The formation of product was quantified from each aliquot removed by using GC-MS with toluene as internal standard. This experiment was performed in triplicate on a single CPF-5 sample.

Figure 4-3C, Uninterrupted Formation of Amination Products upon Switching Substrates. Under an inert nitrogen atmosphere, CPF-5 (1.0 mg, 0.001 mmol active sites, 0.4 mol%) and PhI=NTs (100 mg, 0.27 mmol, 1.0 equiv) were placed into a 24 mL scintillation vial, followed by the addition of 0.026 mL of THP (10% THP in 0.26 mL dry CH₃CN, 0.27 mmol, 1.0 equiv) in 5.0 mL of dry CH₃CN. Reaction mixtures were held at room temperature with gentle agitation using a shaker bed. After 30 min, the PhI=NTs in the initial suspension had dissolved to give a transparent, pale yellow solution. An aliquot (0.05 mL) of the reaction mixture was removed using an airtight syringe and diluted with 1.0 mL of acetone for analysis at each timepoint by GC-MS (Figure 3C). The sealed reaction mixture was transferred back into a glove box, dosed with another 100 mg (0.27 mmol, 1 equiv) of PhI=NTs and 0.023 mL of THF (instead of THP) (10% THF in 0.23 mL dry CH₃CN, 0.27 mmol, 1.0 equiv), and the mixture was held at room temperature with gentle agitation using a shaker bed for another 30 min. This substrate switching process was repeated, giving a total of two additions of THP and two additions of THF (including the initial reaction). The formation of product was quantified from each aliquot removed by using GC-MS with toluene as internal standard. This experiment was performed in triplicate on a single CPF-5 sample.

Figure 4-3D, Recyclable Catalytic Activity. The same procedure was used as described above, with the only difference being that the reaction mixture was completely removed after 30 min using an airtight syringe, and the sealed vial containing CPF-5 crystals was transferred

back into a glove box, dosed with another 100 mg (0.27 mmol, 1 equiv) of PhI=NTs and 0.023 mL of THF (10% THF in 0.23 mL dry CH₃CN, 0.27 mmol, 1.0 equiv) in 5.0 mL of dry CH₃CN, and the mixture was held at room temperature with gentle agitation using a shaker bed for another 30 min. This process of catalyst isolation and reuse was repeated a total of five times (including the initial reaction). The formation of product was quantified from each aliquot removed by using GC-MS with toluene as internal standard. This experiment was performed in triplicate on a single CPF-5 sample.

Catalyst Recyclability. Catalytic reactions were run as described above with slight modification. Under an inert nitrogen atmosphere, CPF-5 (2.0 mg, 0.002 mmol active sites, 1.5 mol%) and PhI=NTs (50 mg, 0.13 mmol, 1.0 equiv) were placed into a 24 mL scintillation vial, followed by the addition of 0.13 mmol (1.0 equiv) of either 0.014 mL of BzTHF (10% BzTHF in 0.14 mL dry CH₃CN, 0.13 mmol, 1.0 equiv) or 0.016 mL of BzTHP (10% BzTHP in 0.16 mL dry CH₃CN, 0.13 mmol, 1.0 equiv) in 5.0 mL of dry CH₃CN. Reaction mixtures were held at room temperature with gentle agitation using a shaker bed. After 30 min, the PhI=NTs in the initial suspension had dissolved to give a transparent, pale yellow solution. After removal of the reaction mixture using a disposable glass pipette (and isolation of the reaction products via silica gel column chromatography), the sealed vial containing the remaining CPF-5 crystals was transferred back into a glove box, and a fresh aliquot of PhI=NTs (50 mg, 0.13 mmol, 1.0 equiv) and substrate (either BzTHF or BzTHP, 0.13 mmol, 1.0 equiv) in 5.0 mL of dry CH₃CN was added to the vial. This process of product isolation and catalyst reuse was repeated up to twenty times. Yields for the isolated products are based on the productive nitrene transfer from the PhI=NTs limiting reagent and are based on at least three independent experiments.

Catalysis with Repeated Addition of PhI=NTs. Catalytic reactions were run as described above with slight modification. Under an inert nitrogen atmosphere, CPF-5 (2.0 mg, 0.002 mmol active sites, 1.5 mol%) and PhI=NTs (50 mg, 0.13 mmol, 1.0 equiv) were placed into a 24 mL scintillation vial, followed by the addition of 0.068 mL of cyclohexene (10% cyclohexene in 0.68 mL dry CHCl₃, 0.67 mmol, 1.0 equiv) in 5.0 mL of dry CHCl₃. Reaction mixtures were held at room temperature with gentle agitation using a shaker bed. After 6 h, the PhI=NTs in the initial suspension had dissolved to give a transparent, pale yellow solution. An aliquot (0.05 mL) of the reaction mixture was removed using airtight syringe and diluted in 1.0 mL of acetone. The sealed reaction mixture was transferred back into a glove box, dosed with another 50.0 mg (0.13 mmol, 1 equiv) of PhI=NTs, and the mixture was held at room temperature with gentle agitation using a shaker bed for 6 h. This process was repeated, giving a total of four additions of PhI=NTs (including the initial reaction). The formation of product was quantified from each aliquot removed by using GC-MS with toluene as internal standard.

Kinetic Measurements on THF C-H Amination by CPF-5 and Determination of Kinetic Isotope Effect (KIE) from Parallel Reactions. Amination catalysis reactions of THF and THF-*d*₈ were performed as described above with slight modifications. Under an inert dinitrogen atmosphere, freshly prepared CPF-5 (2.0 mg, 0.002 mmol active sites, 0.75 mol%) and PhI=NTs (100 mg, 0.27 mmol, 1.0 equiv) were placed into a 24 mL scintillation vial, followed by the addition of 0.40 mmol (1.5 equiv) of either THF or THF-*d*₈ in 5 mL of MeCN. The reaction system was stirred and kept in a water bath with a programmable heating control with a set temperature of 30.0(5) °C. The progress of the reactions was monitored by GC-MS (using toluene as an internal standard) by taking aliquots at regular time intervals as required (Figure S7). Rate constants for the reactions (*k*_{obs}) were obtained for the formation of amination

product using linear fits of $\ln(1-[P]/[P_{\max}])$ vs time (s^{-1}). The reported k_{obs} for both THF and THF- d_8 are the average of three independent runs. All kinetic traces are shown in Figure S7. THF: $k_{\text{obs}} = k_{\text{H}} = 6.0(2) \times 10^{-3} s^{-1}$. THF- d_8 : $k_{\text{obs}} = k_{\text{D}} = 1.3(1) \times 10^{-3} s^{-1}$. $\text{KIE} = k_{\text{H}}/k_{\text{D}} = 4.5(2)$.

Determination of Kinetic Isotope Effect (KIE) from Competitive Amination of THF and THF- d_8 by CPF-5. The amination catalysis reaction was performed as described above with slight modifications. Under an inert dinitrogen atmosphere, freshly prepared CPF-5 (2.0 mg, 0.002 mmol active sites, 0.75 mol%) and PhI=NTs (100 mg, 0.27 mmol, 1.0 equiv) were placed into a 24 mL scintillation vial, followed by the addition of 0.03 mL of a 1:1 mixture of THF/THF- d_8 (0.2 mmol THF; 0.2 mmol THF- d_8) in 5.0 mL of MeCN. The catalysis reaction proceeded until full consumption of PhI=NTs. The reaction mixture was then concentrated under vacuum to dryness. The resulting residue was dissolved in 1.0 mL of CH_2Cl_2 , loaded onto a pre-packed silica gel column, and isolated by flash chromatography using a 0 \rightarrow 20% gradient of ethylacetate in hexanes as the eluent. The isolated product was then analyzed by ^1H NMR spectroscopy and the relative ratio of THF-amination product to unreacted THF was determined by peak integration. This analysis resulted in a $k_{\text{H}}/k_{\text{D}}$ ratio of 4.6(1), based on the assumption that the amount of unreacted THF corresponds directly to the amount of aminated-THF- d_8 .

X-ray Crystallography. After 20 cycles of catalysis, using BzTHF as a substrate in CH_3CN , colorless cubic crystals of CPF-5 were recovered. A crystal was immobilized onto a nylon loop with Paratone grease and flash frozen at 100 K in a liquid N_2 cold stream. Single-crystal X-ray diffraction data were collected at 100 K on a Bruker D8 Diffractometer equipped with a Mo-K α radiation source and APEX-II CCD area detector. The structure was solved via direct methods with SHELXS5 and refined by full-matrix least-squares procedures using

SHELXL within the Olex2 software. The structure was refined in the cubic $F-43c$ space group with $Z = 4$. A total of 50474 reflections were collected of which 4803 were unique. The range of θ was from 2.9° to 50.72° . All non-hydrogen atoms were refined anisotropically with hydrogen atoms placed in idealized positions. BzTHF occupancy was refined to 100% with minor restraints (AFIX 66, ISOR) on the benzene ring to achieve full convergence. Three unidentified solvent molecules were refined bound to the catalytic Mn(II) metal center as a single oxygen atom (water) with 100% occupancy, completing the coordination sphere of the metal ion.

Density Functional Theory (DFT) Calculations. DFT calculations and geometry optimizations were performed using the ORCA program package (F. Neese, *Wiley Interdiscip. Rev.: Comput. Mol. Sci.* **2012**, 2, 73) with the OLYP (Handy, N. C.; Cohen, A. *J. Mol. Phys.* **2001**, 99, 403) functional and the all-electron Ahlrichs triple-zeta basis set def2-TZVP (Schafer, A.; Horn, H.; Ahlrichs, R. *J. Chem. Phys.* **1992**, 97, 2571) and def2-TZVP/J auxiliary (Weigend, F.; Ahlrichs, R. *Phys. Chem. Chem. Phys.* **2005**, 7, 3297). The resolution of identity (RI) approximation was used to accelerate the calculations. Using crystallographic coordinates from CPF-5, a model system was devised utilizing $[\text{Zn}(\text{OH}_2)_3]^+$ in the basal position and 5-methyl-tetrazolate as the bridging ligand (MeTet = 5-methyl-tetrazolate). The diamagnetic $[\text{Zn}(\text{OH}_2)_3]^+$ fragment was used to minimize the potential of extensive multi-configurational behavior stemming from calculations on two high-spin, $S = 5/2$ Mn(II) centers. The geometry of the model $[\text{Zn}(\text{OH}_2)_3(\text{MeTet})_3\text{Mn}(\text{OH}_2)_3]^+$ was fully optimized, after which additional computational elaboration of the Mn site was performed.

Broken symmetry calculations were performed on the models $[\text{Zn}(\text{OH}_2)_3(\text{MeTet})\text{Mn}(\text{NTs})]^+$ (**i1**; I = intermediate; Ts = $\text{SO}_2(p\text{-MeC}_6\text{H}_4)$), $[\text{Zn}(\text{OH}_2)_3(\text{MeTet})\text{Mn}(\text{NTs})(\text{THF})]^+$ (**m1**; m = model), $[\text{Zn}(\text{OH}_2)_3(\text{MeTet})\text{Mn}(\text{N}(\text{H})\text{Ts})(\text{THF}\cdot)]^+$ (**m2**) and $[\text{Zn}(\text{OH}_2)_3(\text{MeTet})\text{Mn}(\square^2\text{-N}, O\text{-N}(\text{H})\text{Ts}(\text{OC}_4\text{H}_7))]^+$ (**p**; p = product). For **i1**, **m1**, and **m2** the broken symmetry electronic structure formalism was employed to investigate alternate electronic ground states. The notation BS(m, n) describes an antiferromagnetically coupled system with ($m + n$) unpaired electrons and a net spin of $(m + n)/2$, in which m α -spin electrons occupy one fragment and n β -spin electrons occupy the other fragment. For **i1**, a Mn(III)-aminyl radical was modeled as BS(4,1) to describe a high-spin Mn(III) ($S = 2$) coupled to an aminyl radical ($S = 1/2$). The results indicated the broken symmetry solution to be strongly favored ($\Delta E_{\text{calc}} = 42.1$ kcal/mol) compared to that of the Mn(IV)-imido electronic structure, with a strongly antiferromagnetically coupled system ($J = 1235$ cm^{-1}). Similarly for **m1**, a Mn(III)-aminyl radical was modeled as BS(4,1) to describe a high-spin Mn(III) ($S = 2$) coupled to an aminyl radical ($S = 1/2$). It was found that the Mn(IV)-imido and Mn(III)-aminyl electronic ground states are essentially isoenergetic ($\Delta E_{\text{calc}} = 8.5 \times 10^{-5}$ kcal/mol). The broken symmetry solution for the Mn(III)-aminyl showed an antiferromagnetically coupled system ($J = 1032$ cm^{-1}), with a total spin population of 13% on N (Figure S11). For **m2**, a Mn(II)-aminyl radical was modeled as BS(5,1) to describe a high-spin Mn(II) ($S = 5/2$) coupled to an aminyl radical ($S = 1/2$). The resultant energy of this system was found to be 39.6 kcal/mol higher in energy than that of the Mn(III) amido electronic structure.

The hypothetical enthalpic reaction trajectory between **i1**, **m1**, **m2**, and **p**, which represents THF binding to **i1**, hydrogen-atom abstraction from **m1** and radical recombination

from **m2** to the resulting product **p** is shown in Figure S12. In this trajectory, the broken-symmetry (4,1) states of **i1** and **m2** were used. The resultant energetics revealed that THF binding to **i1** is enthalpically favorable by 1.8 kcal/mol, while the H-atom abstraction even between **m1** and **m2** is disfavored by only 4.1 kcal/mol. Product **p** formation from **m2** is strongly favored (46.7 kcal/mol) and may reasonably take place via a radical rebound mechanism. Attempts to locate reasonable transition states between **m1** and **m2**, and **m2** and **p** were not successful at the computational level employed.

4.6 Appendix

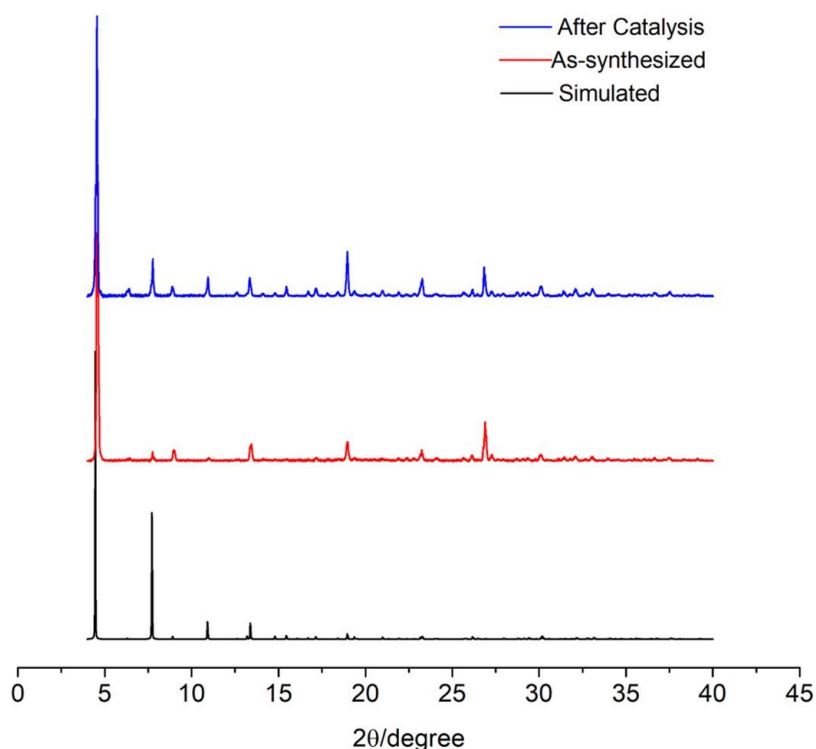


Figure 4-6 PXR D of CPF-5 before (red) and after (blue) catalysis. The CPF-5 after catalysis used for PXR D analysis is the combination of 5 reactions to get enough MOF materials, while only 5 mg of CPF-5 was used for the catalytic reaction.

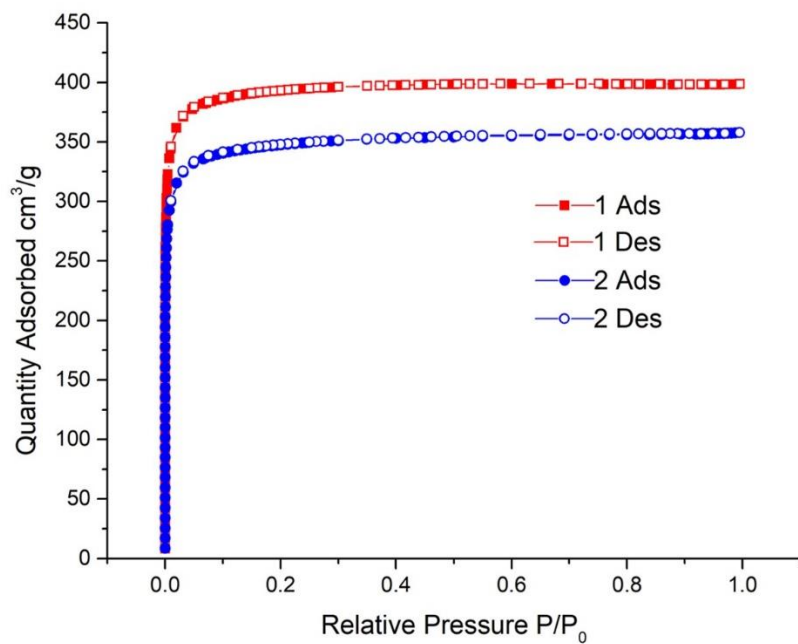


Figure 4-7 N₂ adsorption at 77 K of CPF-5 before (red) and after (blue) catalysis. The BET surface area is $\sim 1409 \pm 70$ m²/g before catalysis (average of two trials) and 1300 m²/g after catalysis.

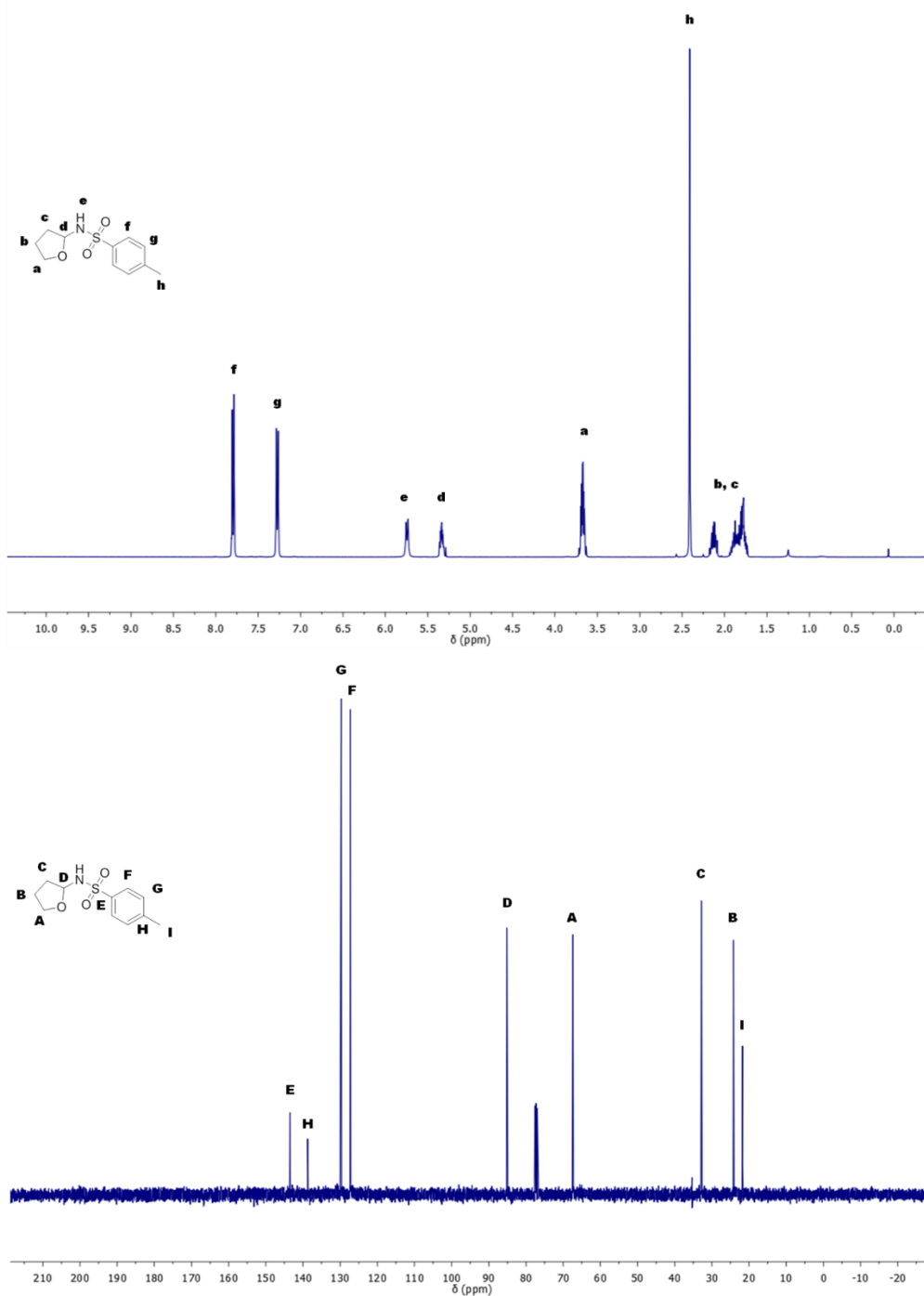
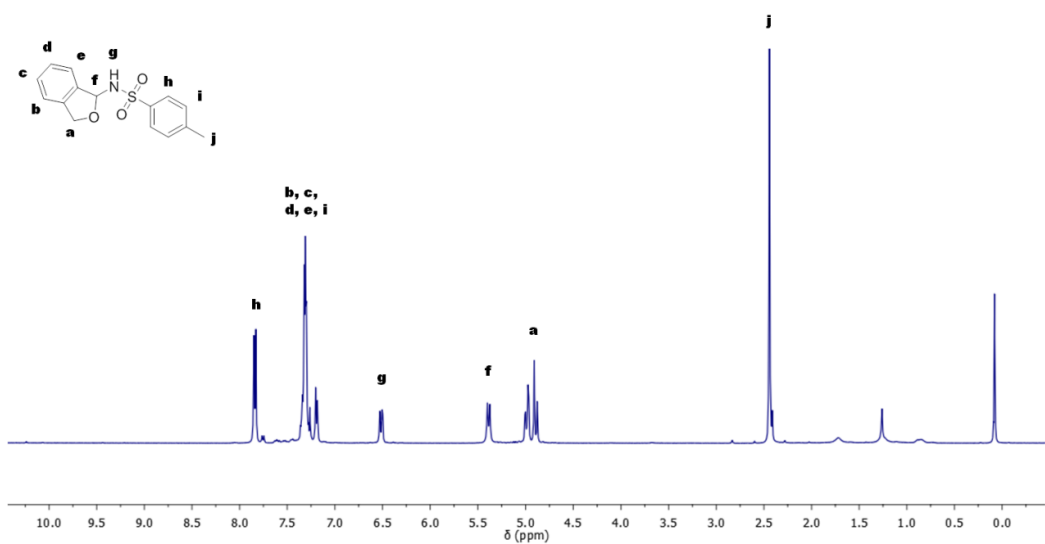


Figure 4-8 ^1H (top) and ^{13}C (bottom) NMR for amination product of THF. ^1H NMR (400 MHz, CDCl_3): δ 7.80 (d, $J = 8.3$ Hz, 2H), 7.27 (d, $J = 8.3$ Hz, 2H), 5.74 (d, $J = 8.8$ Hz, 1H), 5.38 – 5.28 (m, 1H), 3.77 – 3.59 (m, 2H), 2.41 (s, 3H), 2.22 – 2.05 (m, 1H), 1.93 – 1.72 (m, 3H). ^{13}C NMR (100 MHz, CDCl_3): δ 143.5, 138.8, 129.7, 127.3, 85.2, 67.4, 32.8, 24.2, 21.8.



143.52
139.21
138.51
136.51
129.62
128.09
127.19
126.45
123.05
121.14

-88.93

-72.02

-21.65

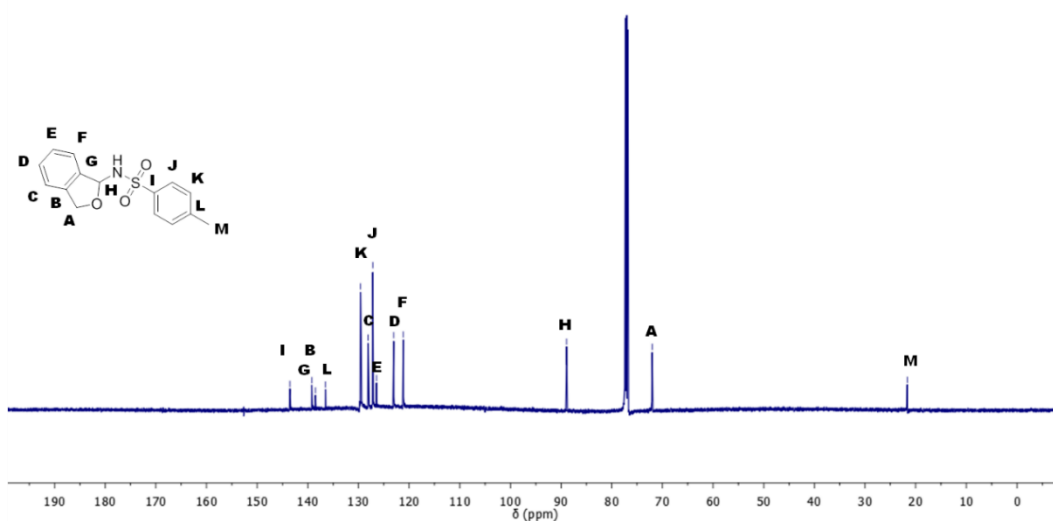


Figure 4-9 ^1H (top) and ^{13}C (bottom) NMR for amination product of BzTHF. ^1H NMR (400 MHz, CDCl_3): δ 7.84 (d, $J = 8.2$ Hz, 2H), 7.32- 7.30 (m, 6H), 6.52 (d, $J = 8.5$ Hz, 1H), 5.39 (d, $J = 10.1$ Hz, 1H), 4.98 (dd, $J = 12.6$ Hz, 12.6 Hz, 2H), 2.44 (s, 3H). ^{13}C NMR (100 MHz, CDCl_3): δ 143.5, 139.2, 138.5, 136.5, 129.6, 128.1, 127.2, 126.5, 123.1, 121.1, 88.9, 72.0, 21.6.

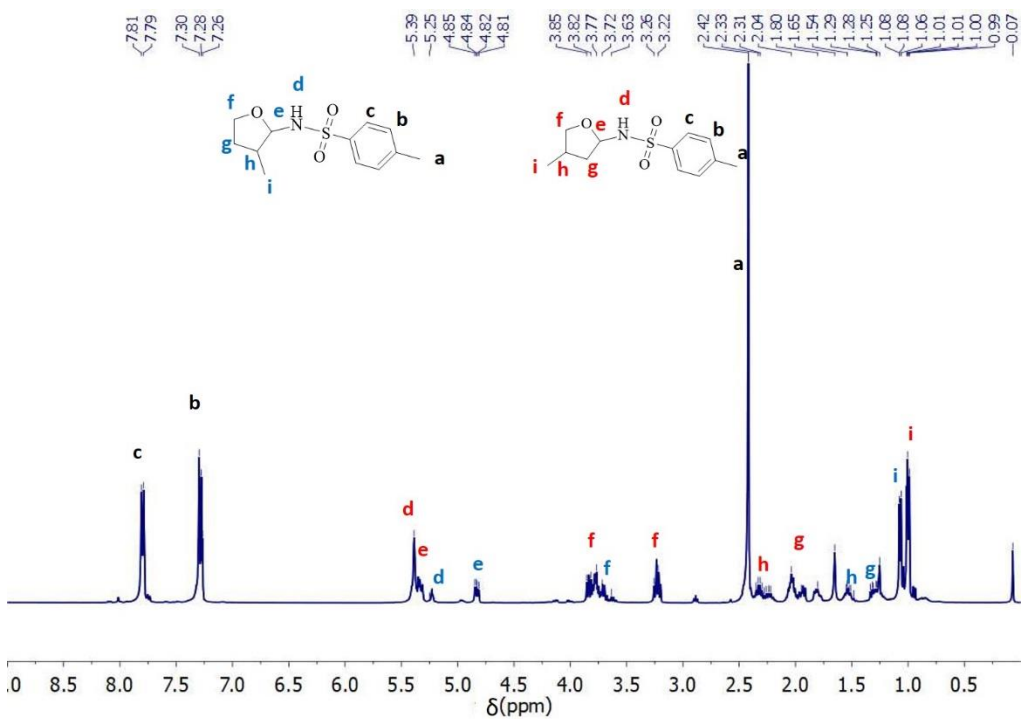


Figure 4-10 ^1H NMR for amination product isomers of 3-Me-THF.

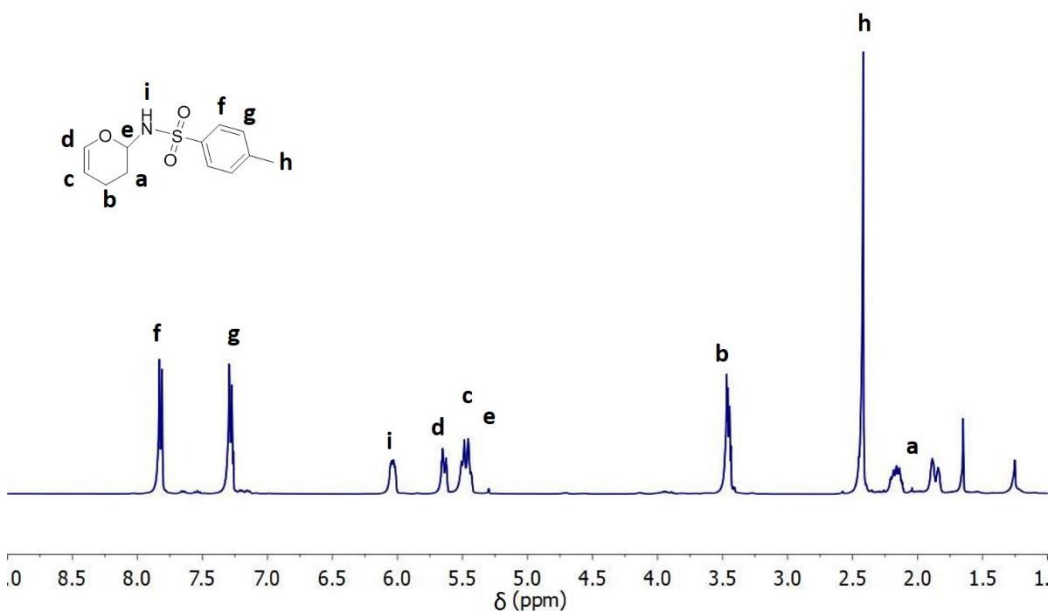


Figure 4-11 ^1H NMR for amination product of DHP. ^1H NMR (400 MHz, CDCl_3): δ 7.82 (d, $J=8.3$, 2H), 7.28 (d, $J=8.0$, 2H), 6.03 (s, 1H), 5.65 (s, 1H), 5.47 (d, $J=11.5$, 2H), 3.57 – 3.33 (m, 2H), 2.42 (s, 3H), 2.16 (s, 1H), 1.89 (s, 1H).

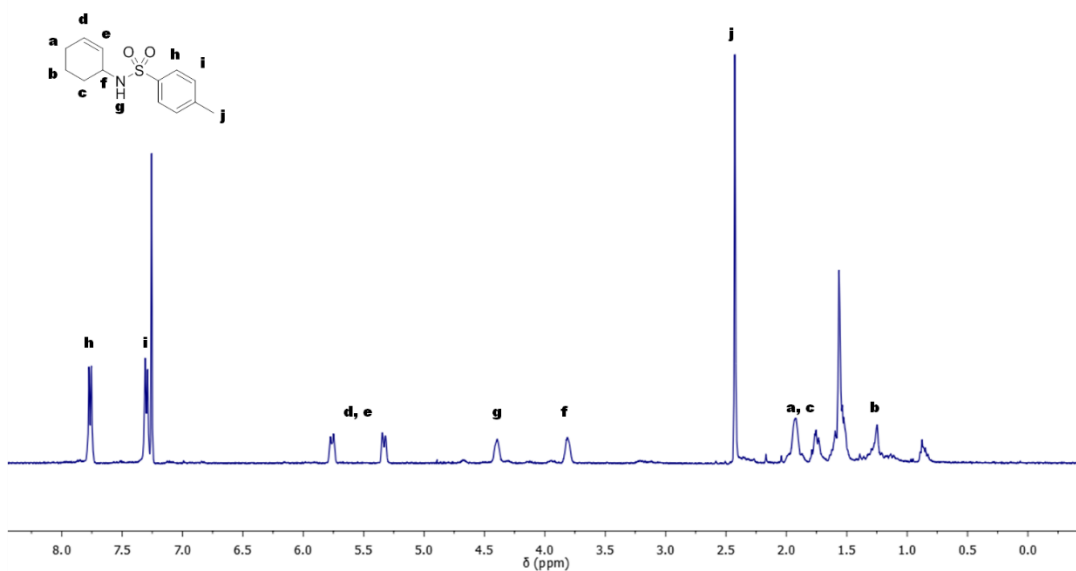


Figure 4-12 ^1H NMR for amination product of cyclohexene. ^1H NMR (400 MHz, CDCl_3): δ 7.87 (d, 2H), 7.30 (d, 2H), 5.76 (d, 1H), 5.33 (d, 1H), 4.39 (s, 1H), 3.81 (s, 1H), 2.43 (s, 3H), 1.93-1.73 (m, 4H), 1.25 (2H).

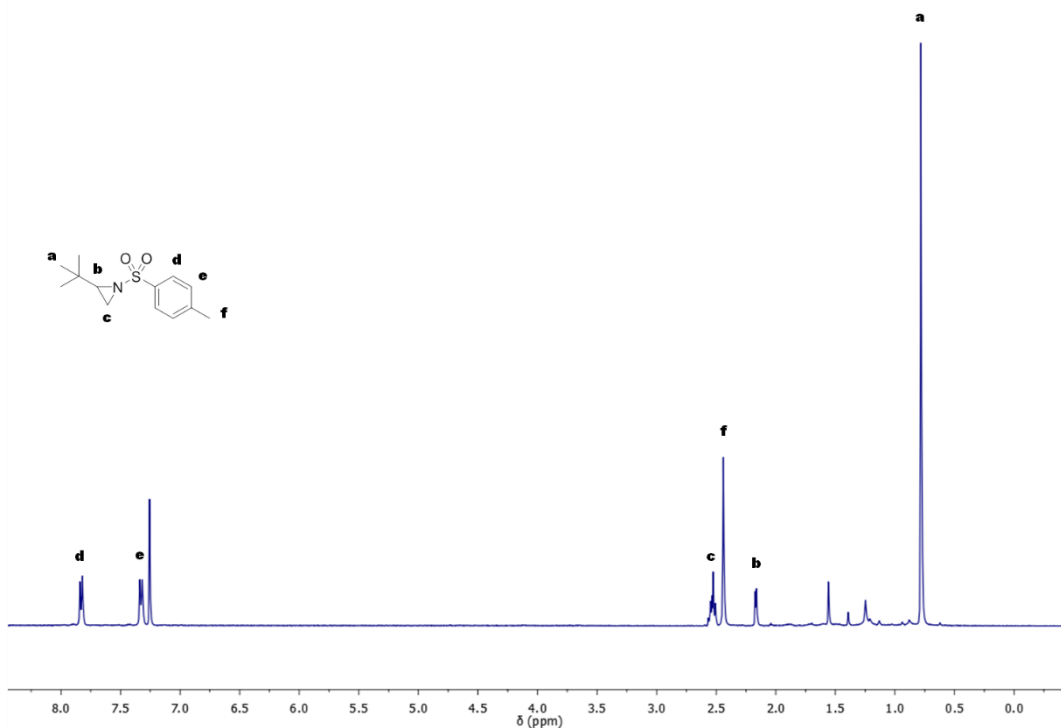


Figure 4-13 ^1H NMR for amination product of TBE. ^1H NMR (400 MHz, CDCl_3): δ 7.83 (d, 2H), 7.31 (d, 2H), 2.51 (m, 2H), 2.44 (s, 3H), 2.15 (d, 1H), 0.75 (s, 9H).

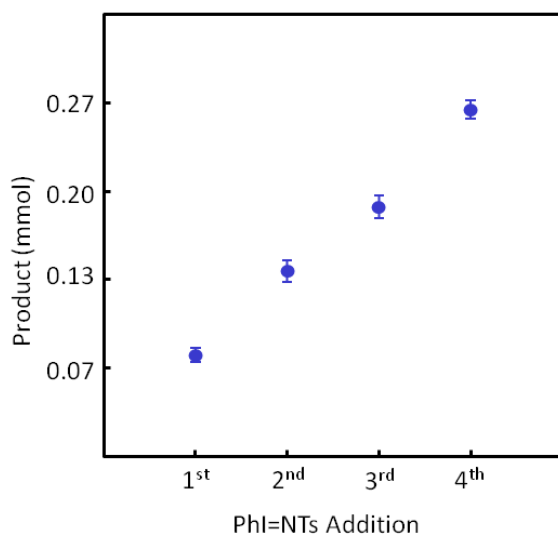


Figure 4-14 Conversion of cyclohexene (0.67 mmol) using 1.5 mol% CPF-5 in 5.0 mL of CHCl_3 , with repeated additions of 50 mg (0.13 mmol) of PhI=NTS. Nitrene transfer to cyclohexene continues with each new addition of PhI=NTs, demonstrating the robust, living nature of the CPF-5 catalyst.

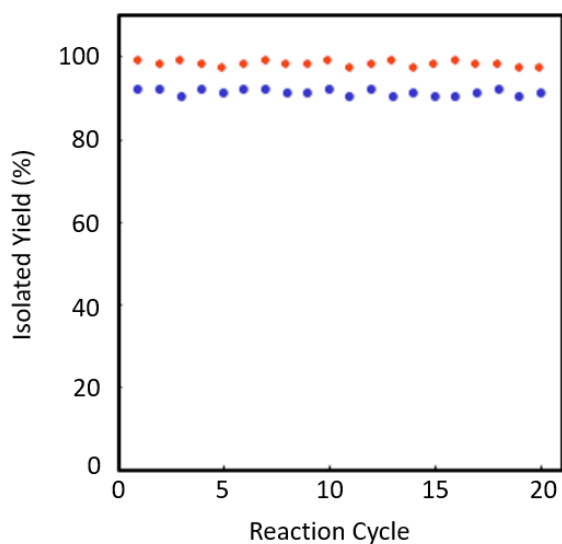


Figure 4-15 Conversion of BzTHF (red) and BzTHP (blue) in the presence of 1.5 mol% CPF-5 and PhI=NTs (1.0 equiv) in dry acetonitrile. The same CPF-5 crystal was used for catalysis twenty times in this experiment with no significant change in reaction yield. Yields reported are isolated product (after column chromatography) and are based on the productive nitrene transfer from PhI=NTs.

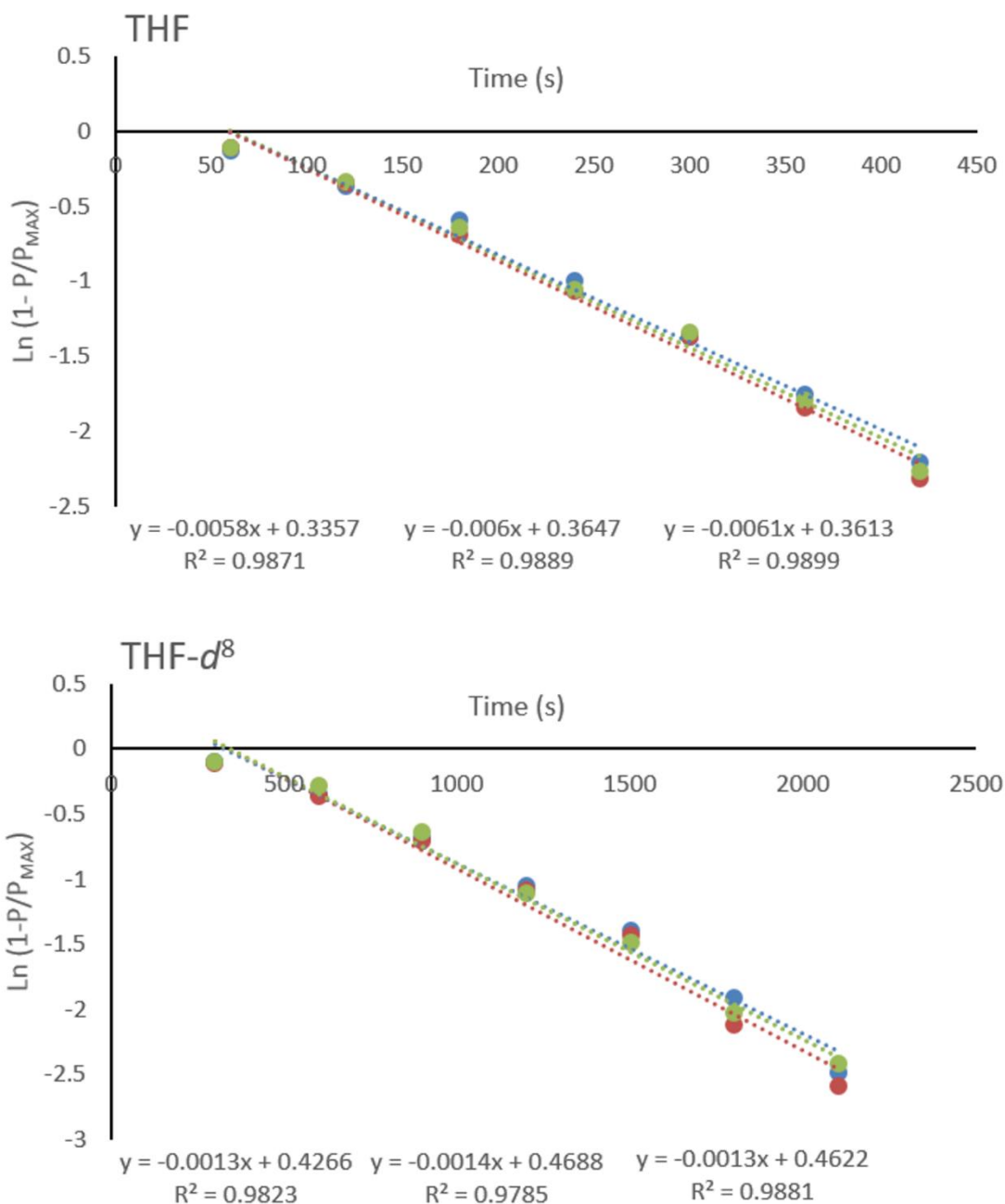


Figure 4-16 Kinetic traces for the amination of THF (*top*) and THF- d_8 (*bottom*) by CPF-5 at 30 °C. The Kinetic Isotope Effect (KIE) for the reaction was determined using the average of three runs for each substrate.

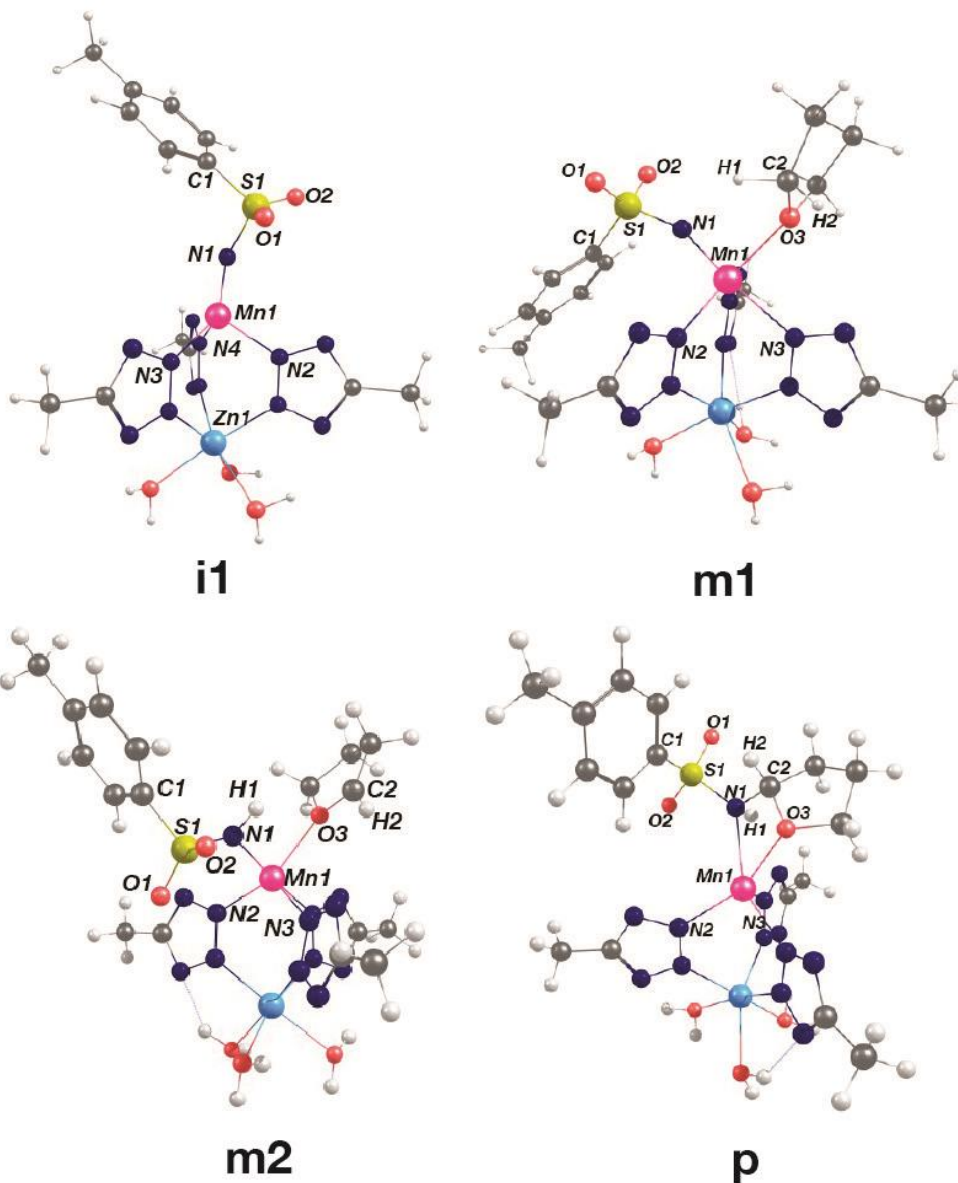


Figure 4-17 Optimized structures of $[\text{Zn}(\text{OH}_2)_3(\text{MeTet})\text{Mn}(\text{NTs})]^+$ (**i1**), $[\text{Zn}(\text{OH}_2)_3(\text{MeTet})\text{Mn}(\text{NTs})(\text{THF})]^+$ (**m1**), $[\text{Zn}(\text{OH}_2)_3(\text{MeTet})\text{Mn}(\text{NTs})(\text{THF}\cdot)]^+$ (**m2**), $[\text{Zn}(\text{OH}_2)_3(\text{MeTet})\text{Mn}(\kappa^2\text{-}N,O\text{-}N(\text{H})\text{Ts}(\text{OC}_4\text{H}_7))]^+$ (**p**). Selected bond distances (Å) and angles (°). **i1 (BS 4,1 solution)**: Mn1-N1 = 1.688; N1-S1 = 1.683; S1-O1 = 1.445; Mn1-N3 = 2.053; Mn1-N2 = 2.044; Mn1-N4 = 2.074; Mn1=Zn = 3.649; Mn1-N1-S1 = 155.01. **m1(BS 4,1 solution)**: Mn-N1 = 1.726; Mn1-O3 = 2.187; O3-C2 = 1.467; N1-S1 = 1.649; Mn1-N2 = 2.078; Mn1-N3 = 2.185; S1-N1-Mn1 = 154.06; N1-Mn1-O3 = 88.85. **m2**: Mn-N1 = 1.912; N1-H1 = 1.026; N1-S1 = 1.689; Mn1-O3 = 2.235; O3-C2 = 1.363; C2-H2 = 1.082; H1-C2 = 2.839; S1-N1-Mn1 = 129.73; H1-N1-Mn1 = 109.22; O3-Mn1-N1 = 86.19. **p**: Mn1-N1 = 2.159; N1-C2 = 1.459; N1-H1 = 1.028; C2-H2 = 1.095; C2-O3 = 1.465; O3-Mn1 = 2.234; Mn1-N2 = 1.773; Mn1-N3 = 2.206; N1-C2-O3 = 103.84; N1-Mn1-O3 = 58.17. Gray, C; cyan, Zn; white, H; pink, Mn; yellow, S; red, O; dark blue, N.

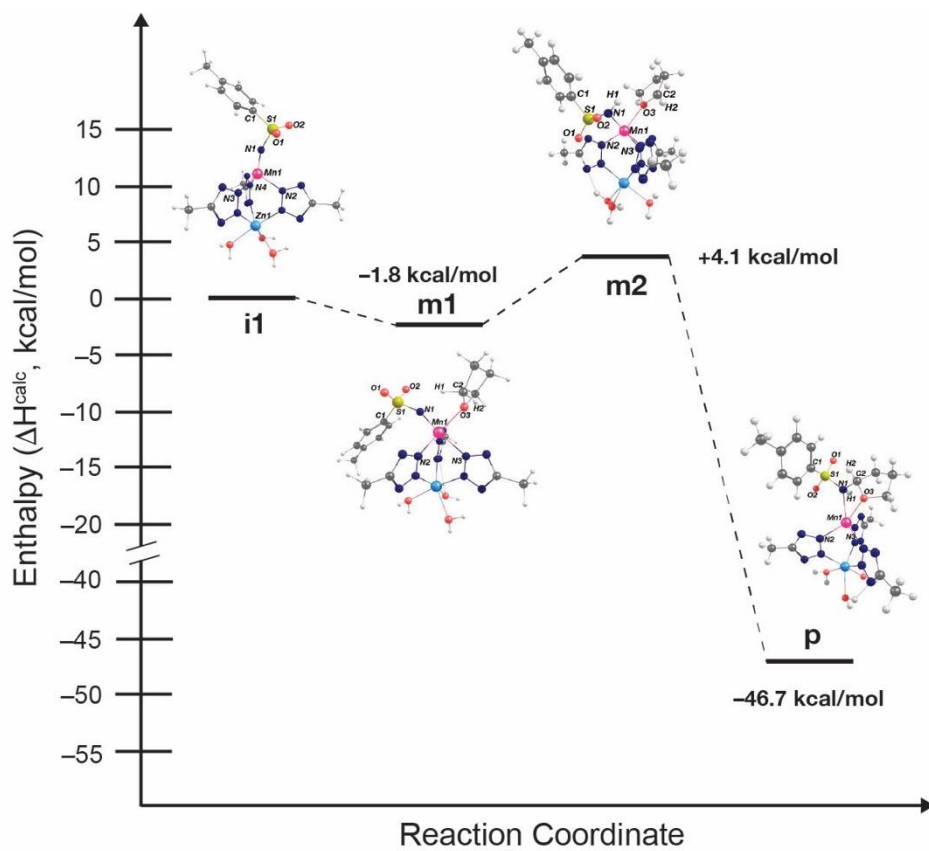


Figure 4-18 Comparative energies along the reaction coordinate for the amination of THF via a proposed hydrogen-atom abstraction/radical recombination pathway.

Table 4-3 Crystal data and structure refinement for CPF-5 after use in 20 catalytic cycles with BzTHF.

Identification code	CPF-5
Empirical formula	Mn ₂₁ C ₁₂₄ H ₆₆ O ₆₀ •(C ₈ H ₈ O) ₁₂
Formula weight	6402.1
Temperature/K	100.0
Crystal system	cubic
Space group	<i>F</i> -43 <i>c</i>
<i>a</i> /Å	39.7158(9)
<i>b</i> /Å	39.7158(9)
<i>c</i> /Å	39.7158(9)
α /°	90
β /°	90
γ /°	90
Volume/Å ³	62646(2)
<i>Z</i>	4
ρ_{calc} /cm ³	1.0917
μ /mm ⁻¹	0.881
<i>F</i> (000)	20812.7
Crystal size/mm ³	0.2 × 0.2 × 0.2
Radiation	Mo K α (λ = 0.71073)
2 Θ range for data collection/°	2.9 to 50.72
Index ranges	-27 ≤ <i>h</i> ≤ 47, -35 ≤ <i>k</i> ≤ 40, -47 ≤ <i>l</i> ≤ 47
Reflections collected	50474
Independent reflections	4803 [<i>R</i> _{int} = 0.0667, <i>R</i> _{sigma} = 0.0342]
Data/restraints/parameters	4803/45/267
Goodness-of-fit on <i>F</i> ²	1.035
Final <i>R</i> indexes [<i>I</i> >= 2 σ (<i>I</i>)]	<i>R</i> ₁ = 0.0507, <i>wR</i> ₂ = 0.1545
Final <i>R</i> indexes [all data]	<i>R</i> ₁ = 0.0588, <i>wR</i> ₂ = 0.1651
Largest diff. peak/hole / e Å ⁻³	1.01/-0.45
Flack parameter	0.01(3)

4.7 Acknowledgements

Text, tables, and figures in this chapter are, in part, reprints of materials published in the paper: “A Metal-Organic Framework with Exceptional Activity for C-H Bond Amination”. Le Wang, Douglas W. Agnew, Xiao Yu, Joshua S. Figueroa*, and Seth M. Cohen* *Angew. Chem. Int. Ed.* **2018**, *57*, 511-515. The dissertation author was a primary researcher for the data presented and was the co-author of this publication. The permissions to reproduce this material were granted by the John Wiley & Sons, copyright 2018.

4.8 References

1. Park, Y.; Kim, Y.; Chang, S., Transition Metal-Catalyzed C–H Amination: Scope, Mechanism, and Applications. *Chem. Rev.* **2017**, *117* (13), 9247-9301.
2. Zalatan, D. N.; Du Bois, J., Metal-Catalyzed Oxidations of C-H to C-N Bonds. *Top Curr Chem* **2010**, *292*, 347-378.
3. Yosca, T. H.; Rittle, J.; Krest, C. M.; Onderko, E. L.; Silakov, A.; Calixto, J. C.; Behan, R. K.; Green, M. T., Iron(IV)hydroxide pKa and the Role of Thiolate Ligation in C–H Bond Activation by Cytochrome P450. *Science* **2013**, *342* (6160), 825-829.
4. Rittle, J.; Green, M. T., Cytochrome P450 Compound I: Capture, Characterization, and C-H Bond Activation Kinetics. *Science* **2010**, *330* (6006), 933-937.
5. Schlichting, I.; Berendzen, J.; Chu, K.; Stock, A. M.; Maves, S. A.; Benson, D. E.; Sweet, R. M.; Ringe, D.; Petsko, G. A.; Sligar, S. G., The Catalytic Pathway of Cytochrome P450cam at Atomic Resolution. *Science* **2000**, *287* (5458), 1615-1622.
6. Badiei, Y. M.; Dinescu, A.; Dai, X.; Palomino, R. M.; Heinemann, F. W.; Cundari, T. R.; Warren, T. H., Copper-Nitrene Complexes in Catalytic C-H Amination. *Angew. Chem. Int. Ed.* **2008**, *120* (51), 9961-9964.
7. King, E. R.; Hennessy, E. T.; Betley, T. A., Catalytic C-H Bond Amination from High-Spin Iron Imido Complexes. *J. Am. Chem. Soc.* **2011**, *133* (13), 4917-4923.
8. Liang, S. W.; Jensen, M. P., Half-Sandwich Scorpionates as Nitrene Transfer Catalysts. *Organometallics* **2012**, *31* (23), 8055-8058.

9. Liu, J.; Chen, L.; Cui, H.; Zhang, J.; Zhang, L.; Su, C.-Y., Applications of metal–organic frameworks in heterogeneous supramolecular catalysis. *Chem. Soc. Rev.* **2014**, *43* (16), 6011-6061.
10. Aida, T.; Inoue, S., Metalloporphyrins as Initiators for Living and Immortal Polymerizations. *Acc. Chem. Res.* **1995**, *29* (1), 39-48.
11. Yoon, M.; Srirambalaji, R.; Kim, K., Homochiral metal–organic frameworks for asymmetric heterogeneous catalysis. *Chem. Rev.* **2011**, *112* (2), 1196-1231.
12. Zhang, T.; Manna, K.; Lin, W., Metal–organic frameworks stabilize solution-inaccessible cobalt catalysts for highly efficient broad-scope organic transformations. *J. Am. Chem. Soc.* **2016**, *138* (9), 3241-3249.
13. Hendon, C. H.; Rieth, A. J.; Korzyński, M. D.; Dincă, M., Grand Challenges and Future Opportunities for Metal–Organic Frameworks. *ACS Cent. Sci.* **2017**, *3* (3), 554-563.
14. Thacker, N. C.; Lin, Z. K.; Zhang, T.; Gilhula, J. C.; Abney, C. W.; Lin, W. B., Robust and Porous beta-Diketiminato-Functionalized Metal-Organic Frameworks for Earth-Abundant-Metal-Catalyzed C-H Amination and Hydrogenation. *J. Am. Chem. Soc.* **2016**, *138* (10), 3501-3509.
15. Thacker, N. C.; Ji, P.; Lin, Z.; Urban, A.; Lin, W., Phenanthroline-based metal–organic frameworks for Fe-catalyzed Csp³–H amination. *Faraday Discuss.* **2017**, *201*, 315-327.
16. Ajellala, N.; Carpentier, J.-F.; Guillaumea, C.; Guillaume, S. M.; Heloua, M.; Poiriera, V.; Sarazina, Y.; Trifonov, A., Metal-catalyzed immortal ring-opening polymerization of lactones, lactides and cyclic carbonates. *Dalton Trans.* **2010**, *39* (36), 8363-8376.
17. Diaz-Requejo, M. M.; Belderrain, T. R.; Nicasio, M. C.; Trofimenko, S.; Perez, P. J., Cyclohexane and benzene amination by catalytic nitrene insertion into C-H bonds with the copper-homoscorpionate catalyst Tp(Br₃)Cu(NCMe). *J. Am. Chem. Soc.* **2003**, *125* (40), 12078-12079.
18. Metzger, E. D.; Brozek, C. K.; Comito, R. J.; Dincă, M., Selective Dimerization of Ethylene to 1-Butene with a Porous Catalyst. *ACS Cent. Sci.* **2016**, *2* (3), 148-161.
19. Comito, R. J.; Metzger, E. D.; Wu, Z.; Zhang, G.; Hendon, C. H.; Miller, J. T.; Dincă, M., Selective Dimerization of Propylene with Ni-MFU-4 l. *Organometallics* **2017**, *36* (9), 1681-1683.

20. Metzger, E. D.; Comito, R. J.; Hendon, C. H.; Dincă, M., Mechanism of Single-Site Molecule-Like Catalytic Ethylene Dimerization in Ni-MFU-4l. *J. Am. Chem. Soc.* **2017**, *139*, 757-762.
21. Wang, L.; Morales, J.; Wu, T.; Zhao, X.; Beyermann, W. P.; Bu, X. H.; Feng, P. Y., Assembly of super-supertetrahedral metal-organic clusters into a hierarchical porous cubic framework. *Chem. Commun.* **2012**, *48* (60), 7498-7500.
22. Trofimenko, S., Scorpionates: genesis, milestones, prognosis. *Polyhedron* **2004**, *23* (2-3), 197-203.
23. Coates, G. W.; Hustad, P. D.; Reinartz, S., Catalysts for the Living Insertion Polymerization of Alkenes: Access to New Polyolefin Architectures Using Ziegler–Natta Chemistry. *Angew. Chem. Int. Ed.* **2002**, *41* (13), 2236-2257.
24. Fructos, M. R.; Trofimenko, S.; Diaz-Requejo, M. M.; Perez, P. J., Facile amine formation by intermolecular catalytic amidation of carbon-hydrogen bonds. *J. Am. Chem. Soc.* **2006**, *128* (36), 11784-11791.
25. Hennessy, E. T.; Betley, T. A., Complex N-Heterocycle Synthesis via Iron-Catalyzed, Direct C-H Bond Amination. *Science* **2013**, *340* (6132), 591-595.
26. Paradine, S. M.; Griffin, J. R.; Zhao, J. P.; Petronico, A. L.; Miller, S. M.; White, M. C., A manganese catalyst for highly reactive yet chemoselective intramolecular C(sp³)-H amination. *Nat. Chem.* **2015**, *7* (12), 987-994.
27. Irving, H.; Williams, R. J. P., The Stability of Transition-metal Complexes. *J. Chem. Soc.* **1953**, 3192-3210
28. Zhong, H. A.; Labinger, J. A.; Bercaw, J. E., C–H Bond Activation by Cationic Platinum(II) Complexes: Ligand Electronic and Steric Effects. *J. Am. Chem. Soc.* **2002**, *124* (7), 1378-1399.
29. Moreau, Y.; Chen, H.; Derat, E.; Hirao, H.; Bolm, C.; Shaik, S., NR Transfer Reactivity of Azo-Compound I of P450. How Does the Nitrogen Substituent Tune the Reactivity of the Species toward CH and CC Activation? *J. Phys. Chem. B.* **2007**, *111* (34), 10288-10299.
30. Au, S.-M.; Huang, J.-S.; Yu, W.-Y.; Fung, W.-H.; Che, C.-M., Aziridination of Alkenes and Amidation of Alkanes by Bis(tosylimido)ruthenium(VI) Porphyrins. A Mechanistic Study. *J. Am. Chem. Soc.* **1999**, *121* (39), 9120-9132.

31. Leung, S. K.-Y.; Tsui, W.-M.; Huang, J.-S.; Che, C.-M.; Liang, J.-L.; Zhu, N., Imido Transfer from Bis(imido)ruthenium(VI) Porphyrins to Hydrocarbons: Effect of Imido Substituents, C–H Bond Dissociation Energies, and RuVI/V Reduction Potentials. *J. Am. Chem. Soc.* **2005**, *127* (47), 16629-16640.
32. Hennessy, E. T.; Liu, R. Y.; Iovan, D. A.; Duncan, R. A.; Betley, T. A., Iron-mediated intermolecular N-group transfer chemistry with olefinic substrates. *Chem. Sci.* **2014**, *5* (4), 1526-1532.
33. Noodleman, L.; Peng, C. Y.; Case, D. A.; Mouesca, J. M., Orbital interactions, electron delocalization and spin coupling in iron-sulfur clusters. *Coord. Chem. Rev.* **1995**, *144*, 199-244.
34. Kundu, S.; Chernev, P.; Engelmann, X.; Chung, C. S.; Dau, H.; Bill, E.; England, J.; Nam, W.; Ray, K., A cobalt(ii) iminoiodane complex and its scandium adduct: mechanistic promiscuity in hydrogen atom abstraction reactions. *Dalton Trans.* **2016**, *45* (37), 14538-14543.
35. Zdilla, M. J.; Abu-Omar, M. M., Mechanism of Catalytic Aziridination with Manganese Corrole: The Often Postulated High-Valent Mn(V) Imido Is Not the Group Transfer Reagent. *J. Am. Chem. Soc.* **2006**, *128* (51), 16971-16979.
36. Su, B.; Cao, Z.-C.; Shi, Z.-J., Exploration of earth-abundant transition metals (Fe, Co, and Ni) as catalysts in unreactive chemical bond activations. *Acc. Chem. Res.* **2015**, *48* (3), 886-896.
37. Denysenko, D.; Jelic, J.; Reuter, K.; Volkmer, D., Postsynthetic Metal and Ligand Exchange in MFU - 4l: A Screening Approach toward Functional Metal - Organic Frameworks Comprising Single - Site Active Centers. *Chem. Eur. J.* **2015**, *21* (22), 8188-8199.
38. Zhao, X.; Bu, X. H.; Nguyen, E. T.; Zhai, Q. G.; Mao, C. Y.; Feng, P. Y., Multivariable Modular Design of Pore Space Partition. *J. Am. Chem. Soc.* **2016**, *138* (46), 15102-15105.
39. Ferey, G.; Serre, C., Large breathing effects in three-dimensional porous hybrid matter: facts, analyses, rules and consequences. *Chem Soc Rev* **2009**, *38* (5), 1380-1399.
40. Mason, J. A.; Oktawiec, J.; Taylor, M. K.; Hudson, M. R.; Rodriguez, J.; Bachman, J. E.; Gonzalez, M. I.; Cervellino, A.; Guagliardi, A.; Brown, C. M.; Llewellyn, P. L.; Masciocchi, N.; Long, J. R., Methane storage in flexible metal-organic frameworks with intrinsic thermal management. *Nature* **2015**, *527* (7578), 357-361.

**Chapter 5 : Metal-Organic Frameworks as Micromotors with Tunable Engines and
Brakes**

5.1 Introduction

The complex transport processes in living cells are possible because of a set of highly efficient and functional biomolecular motors. Recently, there has been a strong interest in the development of organic and inorganic devices and machines that are capable of efficient propulsion and complex operation at the nanoscale through energy consumption.¹⁻⁸ Among the many micro/nanoscale machines, bubble-propelled micromotors are quite powerful and versatile for many practical operations such as biological target transportation and isolation,⁹ drug delivery,¹⁰⁻¹² and environmental remediation.¹³⁻¹⁵ Bubble propulsion commonly involves catalytic decomposition of hydrogen peroxide as a fuel using a catalytic engine to generate oxygen bubbles.¹⁶ Inorganic catalysts including the noble metals Pt and Ag, as well as enzyme catalysts such as catalase, have been used for catalytic propulsion.¹⁷⁻¹⁹ However, the most widely used catalyst, based on Pt metal, is expensive and enzymatic systems such as catalase have limited stability. In most of these systems, the speeds of the bubble propulsion motors are controlled by the amount of fuel used and are difficult to be tuned or halted at will. Given these limitations, there is a strong desire to develop low cost, tunable micromotors with different engines and functional materials for various on-demand operations.

The use of MOFs to build micro- and nanomotors (MNMs) has received little attention, despite the tremendous chemical diversity and tunability of these coordination solids. To the best of our knowledge, only three reports on MOF-based motor devices have been described.²⁰⁻²² Two reports used the Marangoni effect generated by peptide-driven self-assembly as the locomotive source to drive millimeter-size MOF particle.²⁰⁻²¹ A third report used ZIF-67/ZIF-8 Janus particles, with sizes between 200 and 500 μm , that were propelled via the catalytic decomposition of H_2O_2 by the Co^{2+} -based ZIF-67 part of the particle.²² Although these

pioneering reports are at the interface of MOFs and tiny motors, they utilize strategies that have limitations with respect to the choice of MOF that can be used, the types of the motors that can be achieved, and the degree of control over propulsion.

5.2 MOF-MNMs Synthesis and Characterization

Herein, we report facile preparation of micromotors from the widely used Zr^{4+} -based UiO-67 MOF scaffold. The Zr^{4+} -based UiO series of MOFs were selected due to their high chemical stability and tunability.²³ UiO-based micromotors were generated by introducing single-site metal centers on the ligand struts that catalyze the decomposition of H_2O_2 fuel (Figure 5-1). This approach offers a very facile and diverse means of manufacturing MOF micromotors. Most importantly, the catalytic activity of the ‘engine’ can be tuned by the choice of metal ion utilized. In addition, adding suitable chelators as ‘brakes’ could reduce the micromotor speed, further demonstrating the high degree of control and tunability in this MOF micromotor system.

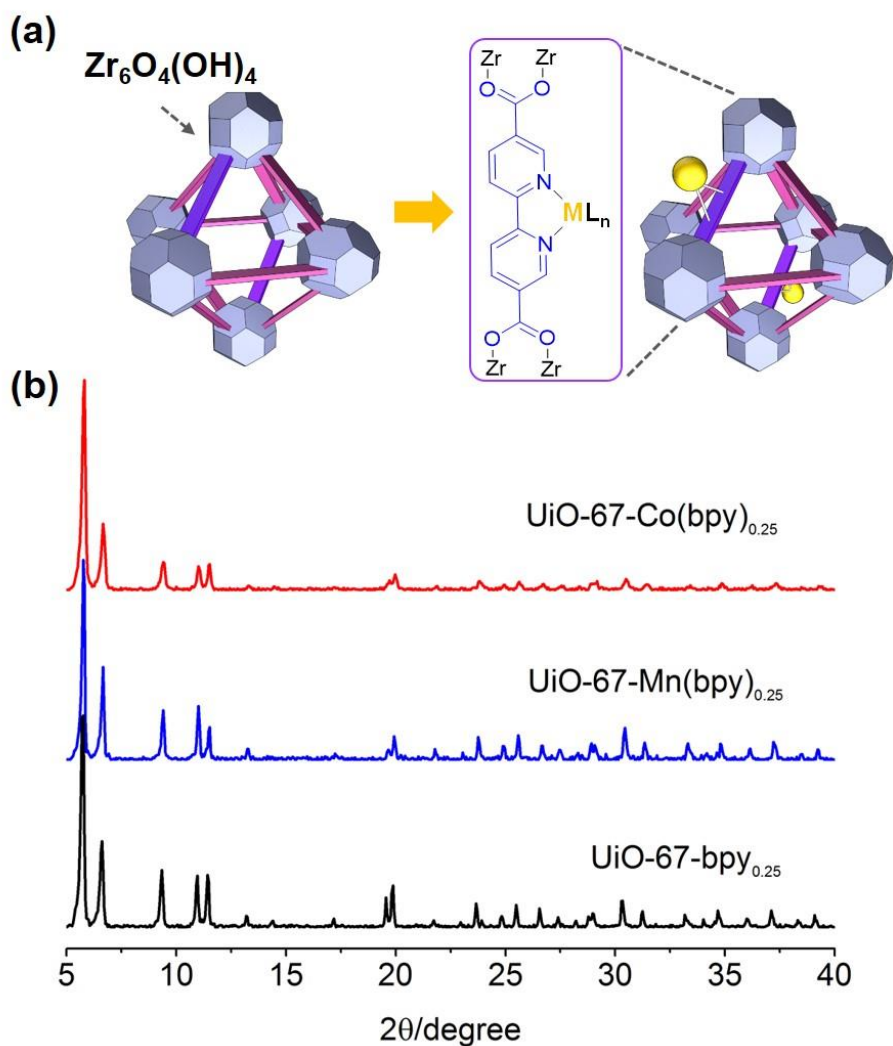


Figure 5-1 Zr-based MOF micromotors. (a) Scheme of the metalation of UiO-67-bpy_{0.25}, (b) PXRD of UiO-67-bpy_{0.25}, UiO-67-Mn(bpy)_{0.25}, and UiO-67-Co(bpy)_{0.25} MOFs

A mixed-ligand method was used to synthesize UiO-67-bpy_{0.25} MOF as the platform, where 25% H₂dc bpy (2,2'-bipyridine-dicarboxylic acid) was mixed with H₂bpdc (biphendicarbonyl) as connecting ligands (Figure 5-1a). During the synthesis, a large excess of benzoic acid was added as a modulator, producing monodisperse particles ~5 μm in diameter. Metalation of the bipyridine sites with cobalt or manganese salts afforded single-site catalytically active MOF nanomotors with good crystallinity, which was confirmed by powder

X-ray diffraction (Figure 5-1b). SEM with EDX (Energy Dispersive X-ray spectroscopy) was used to characterize the metal ratio of metalated UiO-67 (Figure S1, Table S1). For Co^{2+} -metalated UiO-67-bpy_{0.25}, using $\text{Co}(\text{OAc})_2$ (OAc = acetate) as the metal source, postsynthetic modification (PSM) yielded 20% overall metalation, which is equivalent to metalation of 80% of the available bipyridine sites in the MOF. For Mn^{2+} -metalated UiO-67-bpy_{0.25}, $\text{Mn}(\text{OAc})_2$ was found to quantitatively modify UiO-67-bpy_{0.25}. EDX mapping (Figure 5-2) showed the uniform distribution of Co^{2+} and Mn^{2+} in these MOFs.

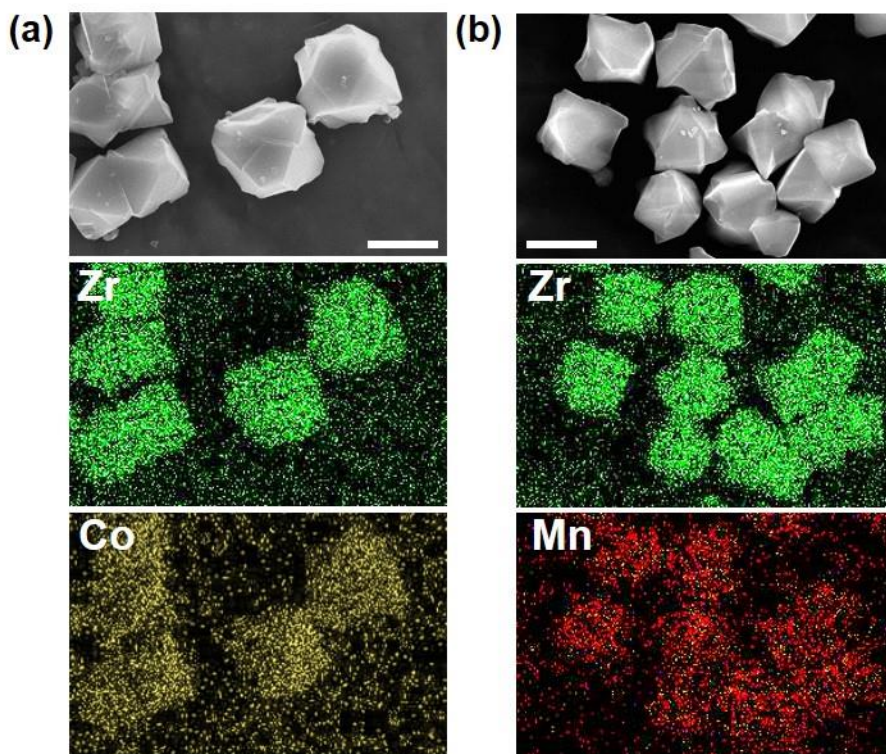


Figure 5-2 SEM and EDX characterization of UiO-67-bpy_{0.25} metalated with different transition metal salts: (a) $\text{Co}(\text{OAc})_2$ and (b) $\text{Mn}(\text{OAc})_2$. Scale bar: 5 μm .

5.3 Motion Test

The resulting UiO-67-Co(bpy)_{0.25} and UiO-67-Mn(bpy)_{0.25} can work as micromotors in fuel solutions, where the metal-based catalytic engine sites decompose H₂O₂ into water and oxygen for bubble-propelled motion (Figure 5-3, Figure 5-7). Control experiments were conducted to confirm the role of the catalytic active sites in these MOF motors. A non-metalated UiO-67-bpy_{0.25} crystal showed no motion in a 5% (v/v) H₂O₂ aqueous solution (no bubbling). Similarly, as-synthesized UiO-67 without any bipyridine sites (only H₂bpdc as a ligand), even when treated with Co(OAc)₂, did not move in H₂O₂ fuel solutions. While the metalated MOF micromotors show efficient motion for at least 6 hrs with continuous fuel supplying. These control experiments indicate that the binding of suitable metal ions at the MOF bipyridine sites is essential to form the catalytic engine.

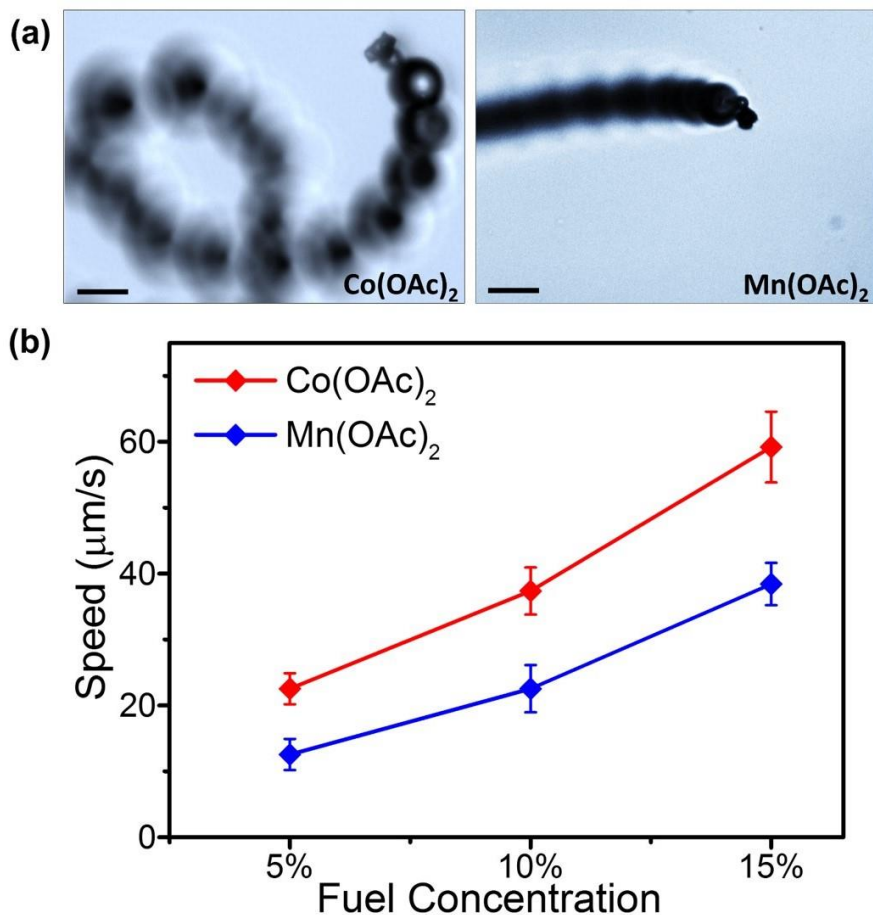


Figure 5-3 Tuning the speed of micromotor engines with different metals. (a) Microscopy images showing the propulsion of micromotor engines made from UiO-67-bpy_{0.25} metalated with Co²⁺ and Mn²⁺. Scale bars: 10 μm . (b) Speed of the different MOF micromotor engines as a function of fuel concentration. Plots are based on measuring the average speed of 30 tracked MOF particles

As expected, when evaluated at different fuel levels (5%, 10%, 15% (v/v) H₂O₂), higher concentrations of H₂O₂ fuel solution gave rise to faster movement of both UiO-67-Co(bpy)_{0.25} and UiO-67-Mn(bpy)_{0.25} particles (Figure 5-3a). These data show a rapid conversion of chemical energy into mechanical work with increasing fuel concentration. Importantly, greater speeds were observed at all fuel concentrations with UiO-67-Co(bpy)_{0.25} when compared to UiO-67-Mn(bpy)_{0.25} (Figure 5-3b), despite the manganese system having a higher loading of

metal ion. This shows that by selecting different metal ions we can tune the performance of the engines in these MOF micromotors. It is observed that the moving direction of the MOF micromotors is random due to the inhomogeneous bubble nucleation on the crystal surface. We envision that by coating with a magnetic layer, such as Ni or Fe, would enable remote magnetic guidance of the MOF motors.^{17, 24-26}

Interestingly, the propulsion of UiO-67 micromotors can be dramatically slowed down and stopped by adding suitable chelators as chemical brakes. This can be achieved by adding chelating ligands such as iminodiacetic acid (IDA) or ethylenediaminetetraacetic acid (EDTA) into the motor-fuel system. The attenuated motion of the MOF motors in the presence of chelator brakes was clearly indicated by a reduction in the ejection of oxygen bubbles from the crystal. Figure 5-4 displays time-lapse images illustrating changes in the motion of the UiO-67-Co(bpy)_{0.25} motor in the presence of IDA with a fuel concentration of 15% (v/v) H₂O₂. The track lines in Figure 5-4a were recorded over a 2 s period following 0 and 15 min exposures to IDA. A clear reduction in bubble ejection and propulsion is observed after adding IDA, with movement of the MOF effectively halted.

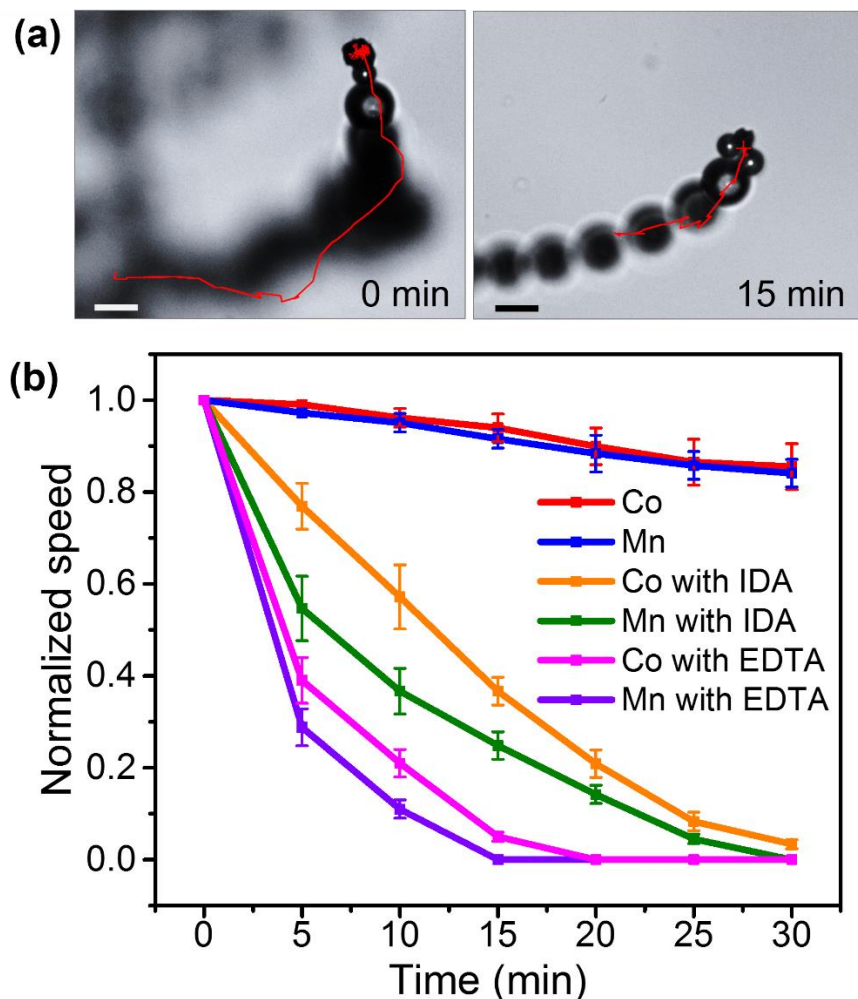


Figure 5-4 Chelators act as molecular brakes for MOF micromotors. (a) Microscopy images showing the propulsion of UiO-67-Co(bpy)_{0.25} at the 0 min and 15 min after adding IDA (0.15 M). The red trajectories indicate the motion in 2 seconds. Scale bars: 10 μm . (b) Time-dependent normalized speed of the micromotor engines UiO-67-Co(bpy)_{0.25} and UiO-67-Mn(bpy)_{0.25} before and after adding chemical brakes: either 0.15 M IDA or EDTA. Fuel concentration: 15% (v/v) H₂O₂.

A comparative study of the braking behaviors of UiO-67-Co(bpy)_{0.25} and UiO-67-Mn(bpy)_{0.25} micromotors in the presence of IDA or EDTA is shown in Figure 5-4, in which the normalized speed of motors is tracked over a 30 min period. In the absence of chemical brakes, both motors only show slightly decreases in speed over a 30 min period (due to the depletion

of fuel). However, the addition of IDA or EDTA resulted in steep drops in speed, even after only 5 min, and completely braking is observed at ~20 min (EDTA) and ~30 min (IDA). The motor tracking data of Figure 5-4b clearly illustrate that EDTA is a more effective brake, which is consistent with the greater chelating ability of EDTA versus IDA. Similarly, UiO-67-Mn(bpy)_{0.25} motors proved to be more susceptible to the chemical brakes than UiO-67-Co(bpy)_{0.25} (Figure 5-4b), which is consistent with lower stability of the Mn(bpy) when compared to Co(bpy) complex.

To investigate the mechanism of braking, the metal content of the MOF motors after exposure to either IDA or EDTA was measured by EDX. The EDX data show (Table 5-1) that ~95% of the Co and Mn were removed from the MOF motors after 30 min exposure to the chemical brakes. The decrease in content upon braking is consistent with a mechanism involving removal engine metals from the active sites of the MOF motors, resulting in the loss of propulsion. To ensure that braking is not due to these chelators destroying the MOF, PXRD and SEM was used to show that these MOFs maintain crystallinity after 30 min incubation in 0.15 M IDA or EDTA solution (Figure 5-5 and 5-6). In addition, the MOF micromotors showed no change in bulk structure, as gauged by microscopic imaging, over the course of the experiment (30 min).

5.4 Conclusion

In conclusion, single-site catalytic MOFs can act as self-propelled micromotors. The propulsion of MOF-nanomotors can be tuned by the metal ion used to power the micromotor engine. In addition, a braking system has been achieved by adding chelator brakes to removing the catalytic engine metal ions, thus controlling the speed and motion of micromotors. We

expect that the strategy employed here for micromotors is adaptable to a much wider variety of MOFs when compared to previously reported approaches. Integrating the functionality of MOF materials with self-propelled micro-/nanomachines will significantly advance the implementation of active transport in catalysis, energy storage and conversion, environmental decontamination, and other applications.

5.5 Experimental

General Methods Starting materials and solvents were purchased and used without further purification from commercial suppliers (Sigma-Aldrich, Alfa Aesar, EMD, TCI, Cambridge Isotope Laboratories, Inc., and others). Centrifugation was performed using a Beckman Coulter Allegra X-22R Centrifuge, with a fixed-angle rotor at 6800 rpm for 10 min. Microscopy videos were captured by an inverted optical microscope (Nikon Instrument Inc. Ti-S/L100), coupled with a Hamamatsu digital camera C11440.

Synthesis of UiO-67-bpy_{0.25}. ZrCl₄ (120 mg, 0.51 mmol), benzoic acid (2.0 g, 16.4 mmol), H₂bpdca (biphenyldicarboxylic acid, 94 mg, 0.39 mmol), and H₂bpydc (2,2'-bipyridine-5,5'-dicarboxylic acid, 32 mg, 0.13 mmol) were placed in a bottle with 20 mL DMF. The solids were dispersed via sonication for ~10 min, followed by incubation at 120 °C for 24 h. After cooling, solids were collected by centrifugation and the solvent was decanted. The solids were washed with DMF (2×20 mL), followed by soaking in ethanol (EtOH) for 3 d, with the solution exchanged with fresh EtOH (10 mL) every 24 h. After 3 d of soaking, the solids were collected via centrifugation and dried under vacuum.

Metalation of UiO-67-bpy_{0.25} with Co(II) or Mn(II). Metal salt (0.1 mmol, Co(OAc)₂ or Mn(OAc)₂) was dissolved in 2 mL MeOH and 0.5 mL DMF. UiO-67-bpy_{0.25} (36 mg, 0.1 mmol)

was added into the solution and dispersed via sonication for ~5 min, then incubated at 55 °C for 24 h. After 24 h at 55 °C, the supernatant was decanted by centrifugation and the solids were washed profusely with DMF (3×10 mL) and MeOH (4×10 mL). The solids were left to soak in MeOH for 3 d, and the solution was exchanged with fresh MeOH (10 mL) every 24 h. After 3 d of soaking, the solids were collected via centrifugation and dried under vacuum to afford UiO-67-Co(bpy)_{0.25} and UiO-67-Mn(bpy)_{0.25}. SEM-EDX was used to quantitate the degree of metalation by Co²⁺ and Mn²⁺.

MOF Micromotor Propulsion Characterization. The autonomous propulsion of the MOF micromotors in aqueous solution was achieved by using hydrogen peroxide fuel at different concentrations (5%, 10%, 15% (v/v) in water). A 2 µL drop of micromotor suspension in water was placed on a glass slide followed by a 2 µL drop of hydrogen peroxide fuel. Microscopy videos were captured by an inverted optical microscope with a digital camera. The videos were tracked and analyzed using the NIS Elements AR 3.2 software. In the chemical braking tests, the hydrogen peroxide fuel was added containing NDI or EDTA at a concentration of 0.3 M. A 2 µL drop of this combined chelator/fuel solution was added to the micromotor suspension, resulting a final chelator concentration of 0.15 M. Videos were captured and tracked in the same manner as experiments without chelator.

Powder X-ray Diffraction (PXRD) Analysis. ~20-30 mg of UiO-67 derivative samples were dried under vacuum prior to PXRD analysis. PXRD data were collected at ambient temperature on a Bruker D8 Advance diffractometer at 40 kV, 40 mA for Cu K α ($\lambda=1.5418$ Å), with a scan speed of 0.2 sec/step, a step size of 0.03° in 2 θ , and a 2 θ range of ~5 to 40° (sample dependent). The experimental backgrounds were corrected using Jade 5.0 software package.

Scanning Electron Microscopy-Energy Dispersed X-ray Spectroscopy. ~2-5 mg of activated UiO-67 derivative materials were transferred to conductive carbon tape on a sample holder disk, and coated using a Ir-sputter coating for 8 sec. A Philips XL ESEM instrument was used for acquiring images using a 10 kV energy source under vacuum. Oxford EDX and Inca software are attached to determine elemental mapping of particle surfaces at a working distance at 10 mm. Electron microscopy images with ~19000× magnification was finely focused, and collected at 10 mm working distance.

5.6 Appendix

Table 5-1 Metal ratio before and after treatment with chemical brakes (IDA or EDTA), as measured by SEM-EDX.

MOF	Treatment	M/Zr ratio (M = Co or Mn)
UiO-67-Co(bpy)_{0.25}	As-synthesized	20%
	With IDA	2%
	With EDTA	1%
UiO-67-Mn(bpy)_{0.25}	As-synthesized	25%
	With IDA	1%
	With EDTA	1%

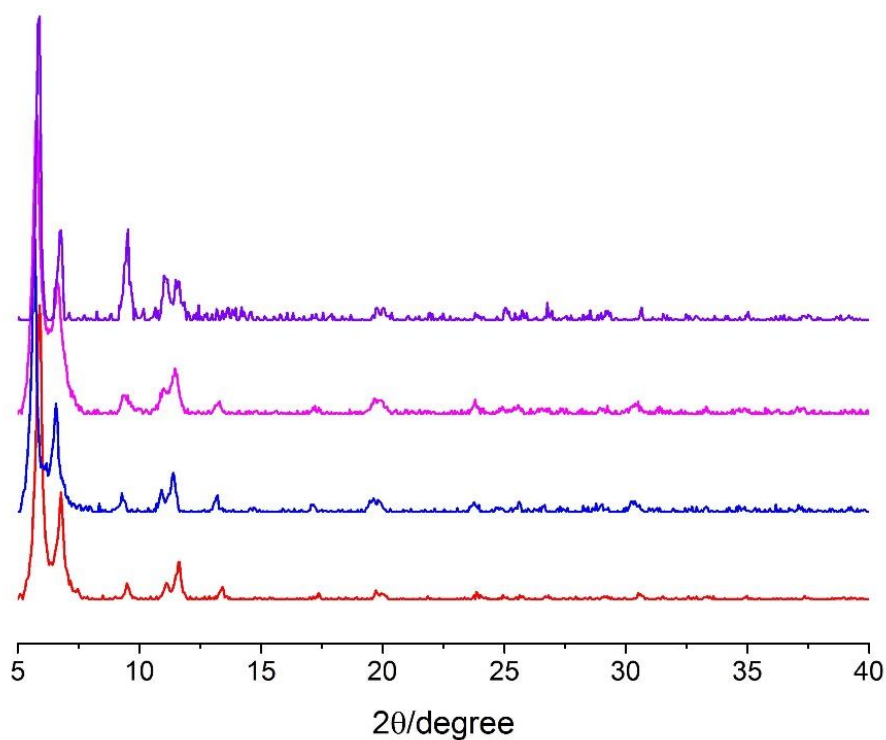


Figure 5-5 PXRD of MOF micromotors after treatment with braking chelators for 1 h: UiO-67-Co(bpy)_{0.25} with EDTA (red), UiO-67-Mn(bpy)_{0.25} with EDTA (blue), UiO-67-Co(bpy)_{0.25} with IDA (magenta), and UiO-67-Mn(bpy)_{0.25} with IDA (violet).

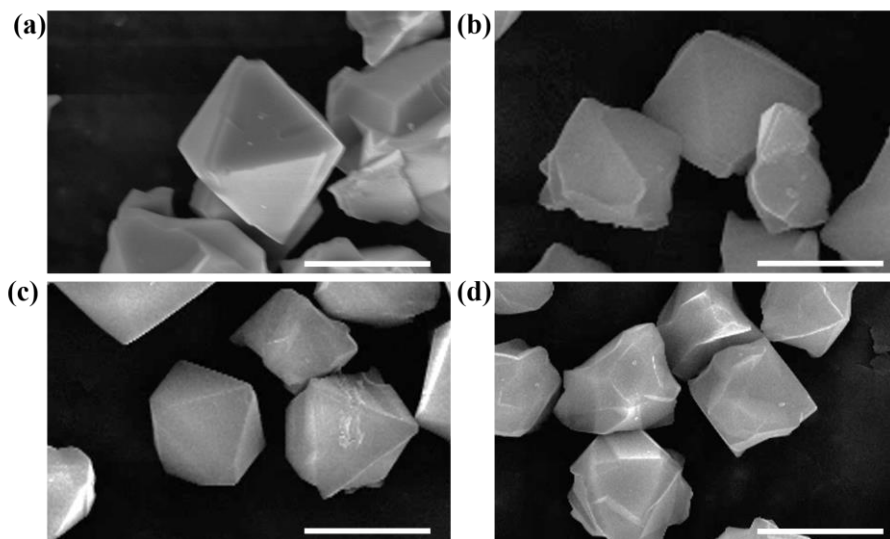


Figure 5-6 SEM of MOF micromotors after treatment with braking chelators for 1 h: (a) UiO-67-Co(bpy)_{0.25} with EDTA, (b) UiO-67-Co(bpy)_{0.25} with IDA, (c) UiO-67-Mn(bpy)_{0.25} with EDTA, and (d) UiO-67-Mn(bpy)_{0.25} with IDA. Scale bars: 5 μ m.

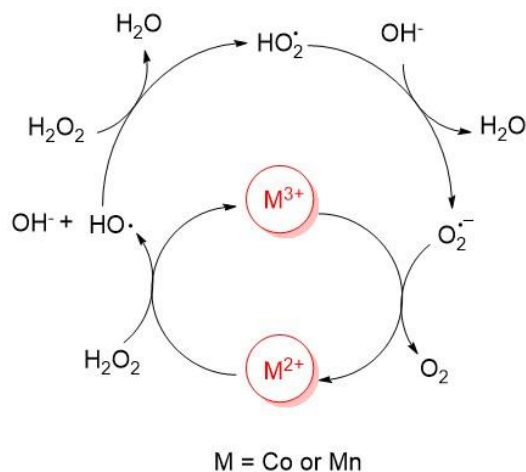


Figure 5-7 Mechanism of catalytic decomposition of hydrogen peroxide by Co(II) or Mn(II).

5.7 Acknowledgements

Text, tables, and figures in this chapter are, in part, reprints of materials published in the paper: “Metal–Organic Frameworks as Micromotors with Tunable Engines”. Jinxing Li, Xiao Yu, Mingli Xu, Wenjuan Liu, Elodie Sandraz, Hsin Lan, Joseph Wang*, and Seth M. Cohen*, *J. Am. Chem. Soc.* **2017**, *139*, 611-614 (J.L. and X.Y. contributed equally). The dissertation author was the primary researcher for the data presented and was the primary author of this publication. The permissions to reproduce this material were granted by the American Chemistry Society, copyright 2017.

5.8 References

1. Balzani, V.; Credi, A.; Raymo, F. M.; Stoddart, J. F., Artificial molecular machines. *Angew. Chem. Int. Ed.* **2000**, *39* (19), 3348-3391.
2. Browne, W. R.; Feringa, B. L., Making molecular machines work. *Nat. Nanotech.* **2006**, *1* (1), 25-35.
3. Wang, J., *Nanomachines: fundamentals and applications*. John Wiley & Sons: 2013.

4. Sanchez, S.; Soler, L.; Katuri, J., Chemically Powered Micro - and Nanomotors. *Angew. Chem. Int. Ed.* **2015**, *54* (5), 1414-1444.
5. Wang, W.; Duan, W.; Ahmed, S.; Mallouk, T. E.; Sen, A., Small power: Autonomous nano-and micromotors propelled by self-generated gradients. *Nano Today* **2013**, *8* (5), 531-554.
6. Mei, Y.; Solovev, A. A.; Sanchez, S.; Schmidt, O. G., Rolled-up nanotech on polymers: from basic perception to self-propelled catalytic microengines. *Chem. Soc. Rev.* **2011**, *40* (5), 2109-2119.
7. Wang, H.; Pumera, M., Fabrication of micro/nanoscale motors. *Chem. Rev.* **2015**, *115* (16), 8704-8735.
8. Guix, M.; Mayorga-Martinez, C. C.; Merkoçi, A., Nano/micromotors in (bio) chemical science applications. *Chem. Rev.* **2014**, *114* (12), 6285-6322.
9. Balasubramanian, S.; Kagan, D.; Jack Hu, C. M.; Campuzano, S.; Lobo - Castañon, M. J.; Lim, N.; Kang, D. Y.; Zimmerman, M.; Zhang, L.; Wang, J., Micromachine - Enabled Capture and Isolation of Cancer Cells in Complex Media. *Angew. Chem. Int. Ed.* **2011**, *50* (18), 4161-4164.
10. Mou, F.; Chen, C.; Zhong, Q.; Yin, Y.; Ma, H.; Guan, J., Autonomous motion and temperature-controlled drug delivery of Mg/Pt-Poly (N-isopropylacrylamide) Janus micromotors driven by simulated Body fluid and blood plasma. *ACS Appl. Mater. Interfaces* **2014**, *6* (12), 9897-9903.
11. Wu, Z.; Wu, Y.; He, W.; Lin, X.; Sun, J.; He, Q., Self - propelled polymer - based multilayer nanorockets for transportation and drug release. *Angew. Chem. Int. Ed.* **2013**, *52* (27), 7000-7003.
12. Li, J.; Thamphiwatana, S.; Liu, W.; Esteban-Fernández de Ávila, B.; Angsantikul, P.; Sandraz, E.; Wang, J.; Xu, T.; Soto, F.; Ramez, V., An Enteric Micromotor Can Selectively Position and Spontaneously Propel in the Gastrointestinal Tract. *ACS nano* **2016**, *10* (10), 9536-9542.
13. Orozco, J.; Cheng, G.; Vilela, D.; Sattayasamitsathit, S.; Vazquez - Duhalt, R.; Valdés - Ramírez, G.; Pak, O. S.; Escarpa, A.; Kan, C.; Wang, J., Micromotor - Based High - Yielding Fast Oxidative Detoxification of Chemical Threats. *Angew. Chem. Int. Ed.* **2013**, *52* (50), 13276-13279.
14. Soler, L.; Magdanz, V.; Fomin, V. M.; Sanchez, S.; Schmidt, O. G., Self-propelled micromotors for cleaning polluted water. *ACS nano* **2013**, *7* (11), 9611-9620.

15. Srivastava, S. K.; Guix, M.; Schmidt, O. G., Wastewater mediated activation of micromotors for efficient water cleaning. *Nano Lett.* **2015**, *16* (1), 817-821.
16. Sun, Y.; Sun, L.; Feng, D.; Zhou, H. C., An In Situ One - Pot Synthetic Approach towards Multivariate Zirconium MOFs. *Angew. Chem. Int. Ed.* **2016**, *55* (22), 6471-6475.
17. Solovev, A. A.; Mei, Y.; Bermúdez Ureña, E.; Huang, G.; Schmidt, O. G., Catalytic Microtubular Jet Engines Self - Propelled by Accumulated Gas Bubbles. *Small* **2009**, *5* (14), 1688-1692.
18. Wang, H.; Zhao, G.; Pumera, M., Beyond platinum: Bubble-propelled micromotors based on Ag and MnO₂ catalysts. *J. Am. Chem. Soc.* **2014**, *136* (7), 2719-2722.
19. Sanchez, S.; Solovev, A. A.; Mei, Y.; Schmidt, O. G., Dynamics of biocatalytic microengines mediated by variable friction control. *J. Am. Chem. Soc.* **2010**, *132* (38), 13144-13145.
20. Ikezoe, Y.; Washino, G.; Uemura, T.; Kitagawa, S.; Matsui, H., Autonomous motors of a metal-organic framework powered by reorganization of self-assembled peptides at interfaces. *Nat. Mater.* **2012**, *11* (12), 1081.
21. Ikezoe, Y.; Fang, J.; Wasik, T. L.; Shi, M.; Uemura, T.; Kitagawa, S.; Matsui, H., Peptide-Metal Organic Framework Swimmers that Direct the Motion toward Chemical Targets. *Nano Lett.* **2015**, *15* (6), 4019-4023.
22. Tan, T. T.; Cham, J. T.; Reithofer, M. R.; Hor, T. A.; Chin, J. M., Motorized Janus metal organic framework crystals. *Chem. Commun.* **2014**, *50* (96), 15175-15178.
23. Kim, M.; Cohen, S. M., Discovery, development, and functionalization of Zr (IV)-based metal-organic frameworks. *CrystEngComm* **2012**, *14* (12), 4096-4104.
24. Gao, W.; Uygun, A.; Wang, J., Hydrogen-bubble-propelled zinc-based microrockets in strongly acidic media. *J. Am. Chem. Soc.* **2011**, *134* (2), 897-900.
25. Gao, W.; Feng, X.; Pei, A.; Gu, Y.; Li, J.; Wang, J., Seawater-driven magnesium based Janus micromotors for environmental remediation. *Nanoscale* **2013**, *5* (11), 4696-4700.
26. Li, J.; Gao, W.; Dong, R.; Pei, A.; Sattayasamitsathit, S.; Wang, J., Nanomotor lithography. *Nat. Commun.* **2014**, *5*, 5026.